Fundamental parameters of very low mass stars in eclipsing binary systems

Ezri Fitzpatrick

Master of Philosophy

Department of Physics, Keele University

October 2024

Abstract

Photometry of binary star and extrasolar planet transits offer an opportunity to characterise their components and test stellar models. When investigating exoplanets, it is important properly understand the host star otherwise large systematic errors will be introduced. Radii predicted by models of low-mass and very low-mass are often too low when compared with observations. This discrepancy between theory and observation as called the "radius inflation problem". In this thesis I investigate how well current stellar models of F/G stars predict the centre-to-limb variation (known as limb darkening) observed and whether the M dwarf companions show signs of the radius inflation problem. I use a class of eclipsing binary star with a low-mass companion (EBLM).

I fit a transit model with the Claret 4-parameter law to *TESS* light curves for 19 EBLMs to parameterise the limb darkening. I combined this with observations from Maxted (2023) for targets with transiting hot Jupiters in the *Kepler* and *TESS* bands and compared with limb darkening parameters predicted by PHOENIX−COND (Claret, 2018) and MPS−ATLAS (Kostogryz et al., 2022), testing for trends with effective temperature and metallicity. I found a significant linear trend in model vs observed limb darkening parameters with effective temperature for *Kepler* systems from limb darkening parameters predicted by PHOENIX-COND. For other model and band combinations, I find no such trends, only offsets between theory and observation, likely caused by magnetic activity. I suggest trends are seen in the *Kepler* band but not *TESS* due to line blanketing but further investigation is needed.

I calculate masses, radii, effective temperatures and gravities of the secondary star from fit parameters and compare with MIST isochrones. By interpolating over metallicity for models of 4 Gyr, I find an average radius inflation of $1.9 \pm 1.0\%$ over my sample. Hence, my observations agree well with MIST models.

Acknowledgements

Firstly, and most importantly, I would like to thank my supervisor Dr. Pierre Maxted for setting up this project. Your mentorship has helped me grow as I take my first steps in research. Thanks to Alix Freckelton for giving me spectroscopic parameters for my target EBLMs, making my analysis possible. This project wouldn't have been possible without funding support from the Haberdashers' Company and my family. I would like to specifically mention my brother Christopher Fitzpatrick who has given me the confidence to explore my interests and curiosities, thanks for always having nerd talks with me in the back of the car on long journeys.

All the friends I've made across the various music societies I've been in over the years, thanks for helping make this time at university much less stressful than it would have been without our shenanigans and organised chaos. Thank you to my friends in the office for your insightful conversations about bear arms, spider sharks, zombies and race cars to name a few! And a special thanks to Dr. Nikki Miller, you have been an inspiration throughout my time at Keele and a great friend.

A special mention to everyone at the International Astronomical Youth Camp, these summers have helped me grow as a person and encourage my love of observational astronomy.

And finally, Cade, you're the best partner a guy could ask for. Thank you for all your support over the past year, through the good times and the difficult.

I dedicate this thesis to my GCSE and A-level teacher Helen Hyde, I know I was only one student of many that you taught but you always believed in me. I would not be here today without your early encouragement. You are greatly missed.

Contents

Abstract . . . . . **i**
Acknowledgements . . . . . **ii**
1 Introduction **1**
1.1 Eclipsing binaries and eclipsing binaries with low mass companions . . 1
1.2 Observing binary stars and exoplanets 2
1.2.1 Using EBLMs to investigate M dwarf stars 4
1.2.1.1 The radius inflation problem 5
1.3 Limb darkening 6
1.3.1 Limb darkening laws 6
1.3.2 The Power-2 law 11
1.3.3 Claret's 4-parameter limb darkening law 11
1.3.4 Measuring limb darkening 13
1.4 Atmospheric models 14
1.4.1 1D plane-parallel 17
1.4.2 1D spherically-symmetric 17
1.5 Markov chain Monte Carlo sampling 18
1.5.1 Sampling theory 18
1.5.2 Likelihood and priors 20
2 Pre-analysis **23**
2.1 Light curve processing 23
2.1.1 Target selection 23
2.1.2 Data processing 24
2.2 Atmospheric parameters 24
2.2.1 Finding a data set 25
3 Light curves **29**
3.1 Calculating light curves 29
3.1.1 Starting parameters 29
3.1.2 Initialising Models 32
3.2 Fitting 33
3.3 Best fit parameters 34
4 Comparing to atmospheric models **38**
4.1 Extracting theoretical parameters 38
4.2 Model Comparisons 40
4.2.1 PHOENIX−COND model 40
4.2.1.1 Metallicity relation 41
4.2.1.2 Temperature relation 44
4.2.2 MPS−ATLAS Set 1 and Set 2 46

4.2.2.1 Metallicity relation 46
4.2.2.2 Temperature relation 46
4.3 Discussion 49
5 Investigations into the radius inflation problem 52
5.1 Methods 52
5.1.1 Light curve fitting 52
5.1.2 Model isochrones 53
5.1.3 Determining primary star mass, radius and average density and secondary star mass, radius and gravity 53
5.1.4 Determining secondary star temperature 56
5.1.5 Quantifying radius inflation in the sample 59
5.1.6 Population assignment 62
5.2 Discussion 63
6 Conclusions 64
6.1 Stellar atmospheric models 64
6.2 Radius inflation 65
A Light curve fits 66

List of Figures

1.1 Graphics showing *TESS* field of view and how the sky is split up for observation. Left: *TESS* field of view with partitions per camera. Middle: sky partitions. Right: time each area of the sky will be observed for over an all-sky survey. Image credit: Ricker et al. (2014) 3

1.2 Schematic demonstrating the definition of the impact parameter, b. The yellow disk represents the primary star and the transparent blue disks represent a transiting companion at different corresponding impact parameters. 4

1.3 Image taken in the visible spectrum during the transit of Venus cross the Sun (2012) to show limb darkening. Image credit: Brocken Inaglory[1]. 7

1.4 Labelled example primary eclipse light curve (*TESS* data for EBLM J0723+79). Numbers in blue circles give contact points of an eclipse. Schematics shown in orange is an example of what would be seen at that point in the light curve of an eclipsing companion from left to right. Point 1: point when companion first begins transiting. Point 2: the full disk of the companion is first over the host. Point 3: companion starts to leave the disk of the host. Point 4: companion no longer eclipses the host. 8

1.5 Diagram to illustrate why we observe limb darkening. Image not to scale and representative of the photosphere of a star. The white lines inside the star are approximately the same length. 9

1.6 Light curves predicted by linear, power-2 and the Claret 4-parameter law for $h_1' = 0.833$ and $h_2' = 0.201$ in comparison to no limb darkening. Purple dot dashed line: uniform disk (i.e. no limb darkening). Solid red line: linear limb darkening (Equation (1.2)). Light green dotted line: Power-2 law (Equation (1.3)). Dark green dashed line: Claret law (Equation (1.4)). Period = 5 days, companion:host radius = 0.05, semi-major axis in terms of stellar radius = 14.9, inclination = 87°, eccentricity = 0. Generated using the `BATMAN` transit model (Kreidberg, 2015). 10

1.7 The Limb-darkening profiles from a fit to the light curve for J0723+79 was sampled using `EMCEE` and the intensity profile for the best fit and a random sample of 100 tested parameters plotted. The left panels show the intensity as a function of μ. The right panels show the intensity as a function of radius. The grey lines are calculated the values of the Claret limb darkening coefficients recovered from a random selection of 100 chains. The green line gives the profile calculated with best fit parameters. The purple dotted lines show where in the profile h_1' and h_2' are dependant. 12

1.8 Histogram showing distribution of metallicities of targets used in this project compared to those used in Maxted (2023). 15

2.1 Cleaned primary eclipse light curve for EBLM J0723+79 folded at the orbital period of the binary. The horizontal yellow dashed line gives the initial estimate of the primary eclipse depth and the difference between the vertical green dashed lines gives the initial estimate of the primary eclipse width. 25

2.2 Graph comparing Gaia model $T_{\rm eff}$ to spectroscopic $T_{\rm eff}$ listed in SWEET-Cat 26

2.3 Graph comparing Gaia model $\log(g)$ to spectroscopic $\log(g)$ listed in SWEET-Cat 27

2.4 Figures comparing Gaia model metallicities to spectroscopic metallicities listed in SWEET-Cat 27

4.1 Figure showing observed limb darkening profile in the *TESS* band compared with the theoretical limb darkening profile as calculated by Claret (2018) as a function of metallicity. 42

4.2 Figure 10 from Maxted (2023). Blue points are results in the *Kepler* band and red points in the *TESS* band. The green line is the line of best fit for all systems plotted above 5500K (relations given in rows 1 and 2 of Table 4.2 in the form of Equation (4.3)). Note, systems above an impact parameter of 0.65 were excluded. 43

4.3 Figure showing the observed limb darkening profile compared to the parameters predicted by the PHOENIX−COND model calculated in Claret (2018). *Kepler* systems are in blue on the left panels and *TESS* systems are in red on the right panels. Data from Maxted (2023) uses unfilled circles, data from this project uses filled circles. The solid green line is the best fit for each set of systems for $T_{\rm eff} > 5500$ and the dotted green line is the relation from Maxted (2023). The grey dashed line is the zero line. Rows 3 and 4 of Table 4.2 in the form of (4.3) give the trends for the *Kepler* systems and rows 5 and 6 give the trends for *TESS*. 45

4.4 Figure showing observed limb darkening profile in the *TESS* band compared with the theoretical limb darkening profile as calculated by Kostogryz et al. (2022) (Set 1) as a function of metallicity. 47
4.5 Figure showing observed limb darkening profile compared with the theoretical limb darkening profile as calculated by Kostogryz et al. (2022) (Set 1) as a function of $T_{\rm eff}$. *Kepler* systems are in blue on the left panels and *TESS* systems are in red on the right panels. Data from Maxted (2023) uses unfilled circles, data from this project uses filled circles. The solid green line is the best fit for each set of systems for $T_{\rm eff} > 5500\,\mathrm{K}$. The grey dashed line is the zero line. Rows 7 and 8 of Table 4.2 in the form of (4.3) give the trends for the *Kepler* systems and rows 9 and 10 give the trends for *TESS*. 48
4.6 Image credit: Zach Berta Thompson[1] using data from Sullivan et al. (2015). Figure shows a schematic of typical spectra of a G dwarf star and M dwarf star in blue and red respectively compared to the *Kepler* and *TESS* bandpass response curves. 50
5.1 Figure showing parameters determined for the primary and secondary stars, plotted with isochrones for comparison. Dark blue points with error bars are EBLMs analysed using synthetic photometry assuming solar alpha element abundance ($[\alpha/\mathrm{Fe}] = 0.0$). The turquoise points and error bars show target J0432−33 which has α-element abundance $[\alpha/\mathrm{Fe}] = +0.24$. The grey lines are MIST isochrones (Dotter, 2016; Choi et al., 2016) plotted for ages 10Gyr and 1Gyr at solar metallicity. The top panels give parameters for the primary star and the bottom panels for the secondary star. 55
5.2 $T_{\rm eff,2}$ vs $\log(g_2)$ and errors plotted for 16 EBLMs from the analysis with their colour corresponding to their metallicity (colour bar shown to the left hand side). MIST isochrones at 4 Gyr, plotted for metallicity −0.5 (purple), +0.0 (orange) and +0.25 (yellow), corresponding to the same colour mapping as the points plotted. See Section 5.1.5 for brief description of isochrone +0.25. 58
5.3 Plot of the radius inflation ($R_{\%}$) vs mass (M_2) for the secondary star in the full sample of 19 EBLMs. Points are plotted with colour mapping correlated to metallicity. 61
A.1 *TESS* light curves (grey points) for J0228+05 with best fit of `BATMAN` from my analysis in Section 3 (red line) from `EMCEE` analysis. Data binned in 120 s intervals with errors equivalent to the mean absolute deviation are shown for reference in purple. Top panel: primary eclipse. Bottom panel: secondary eclipse. 67
A.2 Corner plots from best fits of `BATMAN` to *TESS* data using `EMCEE` from my analysis in Section 3 for J0228+05. 68

A.3 *TESS* light curves (grey points) for J0247−51 with best fit of `BATMAN` from my analysis in Section 3 (red line) from `EMCEE` analysis. Data binned in 120 s intervals with errors equivalent to the mean absolute deviation are shown for reference in purple. Top panel: primary eclipse. Bottom panel: secondary eclipse. 69
A.4 Corner plots from best fits of `BATMAN` to *TESS* data using `EMCEE` from my analysis in Section 3 for J0247−51. 70
A.5 *TESS* light curves (grey points) for J0400−51 with best fit of `BATMAN` from my analysis in Section 3 (red line) from `EMCEE` analysis. Data binned in 120 s intervals with errors equivalent to the mean absolute deviation are shown for reference in purple. Top panel: primary eclipse. Bottom panel: secondary eclipse. 71
A.6 Corner plots from best fits of `BATMAN` to *TESS* data using `EMCEE` from my analysis in Section 3 for J0400−51. 72
A.7 *TESS* light curves (grey points) for J0432−33 with best fit of `BATMAN` from my analysis in Section 3 (red line) from `EMCEE` analysis. Data binned in 120 s intervals with errors equivalent to the mean absolute deviation are shown for reference in purple. Top panel: primary eclipse. Bottom panel: secondary eclipse. 73
A.8 Corner plots from best fits of `BATMAN` to *TESS* data using `EMCEE` from my analysis in Section 3 for J0432−33. 74
A.9 *TESS* light curves (grey points) for J0440−48 with best fit of `BATMAN` from my analysis in Section 3 (red line) from `EMCEE` analysis. Data binned in 120 s intervals with errors equivalent to the mean absolute deviation are shown for reference in purple. Top panel: primary eclipse. Bottom panel: secondary eclipse. 75
A.10 Corner plots from best fits of `BATMAN` to *TESS* data using `EMCEE` from my analysis in Section 3 for J0440−48. 76
A.11 *TESS* light curves (grey points) for J0500−46 with best fit of `BATMAN` from my analysis in Section 3 (red line) from `EMCEE` analysis. Data binned in 120 s intervals with errors equivalent to the mean absolute deviation are shown for reference in purple. Top panel: primary eclipse. Bottom panel: secondary eclipse. 77
A.12 Corner plots from best fits of `BATMAN` to *TESS* data using `EMCEE` from my analysis in Section 3 for J0500−46. 78
A.13 *TESS* light curves (grey points) for J0526−34 with best fit of `BATMAN` from my analysis in Section 3 (red line) from `EMCEE` analysis. Data binned in 120 s intervals with errors equivalent to the mean absolute deviation are shown for reference in purple. Top panel: primary eclipse. Bottom panel: secondary eclipse. 79

A.14 Corner plots from best fits of `BATMAN` to *TESS* data using `EMCEE` from my analysis in Section 3 for J0526−34. 80

A.15 *TESS* light curves (grey points) for J0608−59 with best fit of `BATMAN` from my analysis in Section 3 (red line) from `EMCEE` analysis. Data binned in 120 s intervals with errors equivalent to the mean absolute deviation are shown for reference in purple. Top panel: primary eclipse. Bottom panel: secondary eclipse. 81

A.16 Corner plots from best fits of `BATMAN` to *TESS* data using `EMCEE` from my analysis in Section 3 for J0608−59. 82

A.17 *TESS* light curves (grey points) for J0625−43 with best fit of `BATMAN` from my analysis in Section 3 (red line) from `EMCEE` analysis. Data binned in 120 s intervals with errors equivalent to the mean absolute deviation are shown for reference in purple. Top panel: primary eclipse. Bottom panel: secondary eclipse. 83

A.18 Corner plots from best fits of `BATMAN` to *TESS* data using `EMCEE` from my analysis in Section 3 for J0625−43. 84

A.19 *TESS* light curves (grey points) for J0627−67 with best fit of `BATMAN` from my analysis in Section 3 (red line) from `EMCEE` analysis. Data binned in 120 s intervals with errors equivalent to the mean absolute deviation are shown for reference in purple. Top panel: primary eclipse. Bottom panel: secondary eclipse. 85

A.20 Corner plots from best fits of `BATMAN` to *TESS* data using `EMCEE` from my analysis in Section 3 for J0627−67. 86

A.21 *TESS* light curves (grey points) for J0709−52 with best fit of `BATMAN` from my analysis in Section 3 (red line) from `EMCEE` analysis. Data binned in 120 s intervals with errors equivalent to the mean absolute deviation are shown for reference in purple. Top panel: primary eclipse. Bottom panel: secondary eclipse. 87

A.22 Corner plots from best fits of `BATMAN` to *TESS* data using `EMCEE` from my analysis in Section 3 for J0709−52. 88

A.23 *TESS* light curves (grey points) for J0723+79 with best fit of `BATMAN` from my analysis in Section 3 (red line) from `EMCEE` analysis. Data binned in 120 s intervals with errors equivalent to the mean absolute deviation are shown for reference in purple. Top panel: primary eclipse. Bottom panel: secondary eclipse. 89

A.24 Corner plots from best fits of `BATMAN` to *TESS* data using `EMCEE` from my analysis in Section 3 for J0723+79. 90

A.25 *TESS* light curves (grey points) for J0829+66 with best fit of `BATMAN` from my analysis in Section 3 (red line) from `EMCEE` analysis. Data binned in 120 s intervals with errors equivalent to the mean absolute deviation are shown for reference in purple. Top panel: primary eclipse. Bottom panel: secondary eclipse. 91
A.26 Corner plots from best fits of `BATMAN` to *TESS* data using `EMCEE` from my analysis in Section 3 for J0829+66. 92
A.27 *TESS* light curves (grey points) for J0941−31 with best fit of `BATMAN` from my analysis in Section 3 (red line) from `EMCEE` analysis. Data binned in 120 s intervals with errors equivalent to the mean absolute deviation are shown for reference in purple. Top panel: primary eclipse. Bottom panel: secondary eclipse. 93
A.28 Corner plots from best fits of `BATMAN` to *TESS* data using `EMCEE` from my analysis in Section 3 for J0941−31. 94
A.29 *TESS* light curves (grey points) for J0955−39 with best fit of `BATMAN` from my analysis in Section 3 (red line) from `EMCEE` analysis. Data binned in 120 s intervals with errors equivalent to the mean absolute deviation are shown for reference in purple. Top panel: primary eclipse. Bottom panel: secondary eclipse. 95
A.30 Corner plots from best fits of `BATMAN` to *TESS* data using `EMCEE` from my analysis in Section 3 for J0955−39. 96
A.31 *TESS* light curves (grey points) for J1626+57 with best fit of `BATMAN` from my analysis in Section 3 (red line) from `EMCEE` analysis. Data binned in 120 s intervals with errors equivalent to the mean absolute deviation are shown for reference in purple. Top panel: primary eclipse. Bottom panel: secondary eclipse. 97
A.32 Corner plots from best fits of `BATMAN` to *TESS* data using `EMCEE` from my analysis in Section 3 for J1626+57. 98
A.33 *TESS* light curves (grey points) for J1640+49 with best fit of `BATMAN` from my analysis in Section 3 (red line) from `EMCEE` analysis. Data binned in 120 s intervals with errors equivalent to the mean absolute deviation are shown for reference in purple. Top panel: primary eclipse. Bottom panel: secondary eclipse. 99
A.34 Corner plots from best fits of `BATMAN` to *TESS* data using `EMCEE` from my analysis in Section 3 for J1640+49. 100
A.35 *TESS* light curves (grey points) for J1705+55 with best fit of `BATMAN` from my analysis in Section 3 (red line) from `EMCEE` analysis. Data binned in 120 s intervals with errors equivalent to the mean absolute deviation are shown for reference in purple. Top panel: primary eclipse. Bottom panel: secondary eclipse. 101

A.36 Corner plots from best fits of `BATMAN` to *TESS* data using `EMCEE` from my analysis in Section 3 for J1705+55. 102
A.37 *TESS* light curves (grey points) for J1850+50 with best fit of `BATMAN` from my analysis in Section 3 (red line) from `EMCEE` analysis. Data binned in 120 s intervals with errors equivalent to the mean absolute deviation are shown for reference in purple. Top panel: primary eclipse. Bottom panel: secondary eclipse. 103
A.38 Corner plots from best fits of `BATMAN` to *TESS* data using `EMCEE` from my analysis in Section 3 for J1850+50. 104

List of Tables

3.1 Characteristic parameters and labels of targets for reference. Target EBLM and TIC IDs; magnitudes in the TESS band; Effective temperature gravity and metallicity of the primary star (for references see Table 4.1; masses and radii of stars found in Section 5; orbital periods with references as footnotes. Numbers in brackets are the errors on the final digits. 30
3.2 List of stars analysed with note of how they were analysed. Targets marked "Circular" had no eccentricity variation in fitting. Targets marked "Eccentricity priors" had an eccentricity prior obtained from literature applied. Targets marked "No available priors" had no eccentricity priors applied and instead $e\cos(\omega)$ and $e\sin(\omega)$ were varied. . . . 32
3.3 Light curve model parameters obtained from `EMCEE` fit of `BATMAN` to *TESS* data. Values in parentheses are the standard errors on the final two digits of the preceding value. D is the primary eclipse depth, W is the primary eclipse width, b is the impact parameter and L is the secondary eclipse depth 35
3.4 Limb darkening parameters obtained from `EMCEE` fit of `BATMAN` to *TESS* data. Values in parentheses are the standard errors on the final two digits of the preceding value. h_1' and h_2' are the limb darkening profile summary statistics as defined in Equation (1.6). 36
3.5 Parameters obtained from `EMCEE` fit of `BATMAN` to *TESS* data. Values in parentheses are the standard errors on the final two digits of the preceding value. Where k is the radius ratio, and J is the surface brightness ratio 37
4.1 Atmospheric parameters with relevant references 39
4.2 Relationship from least-squares fit for a straight line (Equation (4.3)) determined for different models and bands and their respective limb darkening coefficient as a function of $(T_{\rm eff} - 6000{\rm K})/1000{\rm K}$. σ_X is the additional scatter added in quadrature to the standard error on $\Delta h_1'$ or $\Delta h_2'$ to obtain $\chi^2 = N_{df}$ (which is equal to the number of targets).
(*) Magnitude of the gradient trend is more than two times the standard error.
([1]) Limb darkening parameters compared to Claret (2018).
([2]) Limb darkening parameters compared to Kostogryz et al. (2022), Set 1. 41
5.1 Data behind Figures 5.1, 5.2 and 5.3. Numbers in brackets give errors on the lattermost digits. 59

1 Introduction

1.1 Eclipsing binaries and eclipsing binaries with low mass companions

When one star orbits another they are referred to as a binary star. If the stars in a binary cross in front of each other from our point of view, they are referred to as an eclipsing binary star.

Eclipsing binaries are excellent laboratories for studying the properties of stars. Due to their nature, we are able to precisely measure many properties of the stars without making assumptions about the system and relying on models. We are able to directly measure the mass and radius of binaries from photometric and radial velocity analysis. This makes eclipsing binaries great benchmark stars for stellar science (eg, Gómez Maqueo Chew et al. (2014); Higl & Weiss (2017).

Eclipsing binaries with low mass companions (EBLMs) are a class of binary star consisting of a primary F/G/K star and a secondary M dwarf companion (Triaud et al., 2013). This class of binary star is often found in surveys searching for transiting exoplanets due to the low luminosity of the companion producing very shallow secondary eclipses, much like hot Jupiters (Triaud et al., 2017). Because of this, it is quite common to use terms usually used when describing exoplanets instead of their binary star analogue, for example, this thesis references impact parameter instead of inclination. Extrasolar planets (or exoplanets) are planets that do not orbit our Sun. Hot Jupiters are a class of exoplanet that are Jupiter mass and have an orbital period of less than 10 days causing a high surface temperature. A series of papers presented in Triaud et al. (2013) called "The EBLM project" aims to characterise these objects containing stars at the stellar-substellar border.

1.2 Observing binary stars and exoplanets

A very powerful method for observing binary stars and exoplanets is photometry of transits. Transit light curves show periodic dips in the brightness coming from a target. In EBLM systems when the secondary (or companion) star transits across the primary star, we see a dip in light of about 1% of the intensity outside of eclipse. When the primary star eclipses the secondary star we usually see a small dip on the order of 0.2%. EBLM and hot Jupiter transit light curves are often confused as the hottest hot Jupiters can have day-side effective temperatures as hot as the coolest stars (Gaudi et al., 2017) making their light curves show similar dips in flux. The main difference between EBLM and hot Jupiter transit light curves is that the latter usually do not show a secondary eclipse. From these light curves we are able to calculate properties, for example: radius ratio and surface brightness ratio.

There are a number of ground-based and space-based surveys which are used to investigate binary stars and exoplanets, in this project I am specifically interested in the space based telescopes *Kepler* and *TESS*.

The *Kepler* Mission was launched in 2009 with the purpose of finding Earth-size planets in the habitable zone around Sun-like stars. It has a bandpass of around $400 - 900$ nm (Borucki et al., 2008). *Kepler* light curves were not analysed in this project, however, data from Maxted (2023)'s light curve analysis of *Kepler* band hot Jupiter transits were used when investigating stellar atmospheres in Section 4.

The Transiting Exoplanet Survey Satellite (or *TESS*) was launched in 2018 with the purpose of recording exoplanet transits, but in its time has also observed many eclipsing binary stars. For example, Prša et al. (2022) catalogue 4584 eclipsing binaries in the first 2 years of *TESS* data. The *TESS* bandpass operates in the $600 - 1000$ nm range (Ricker et al., 2014). As the mission was designed to monitor main-sequence dwarf stars for planetary transits, the telescope is well suited to use to analyse high precision photometry of EBLMs. For a *TESS* observation sector, each hemisphere of the sky is split into 13 observation sectors, overlapping at the ecliptic poles as seen in Figure 1.1. *TESS* continuously observes one sector for 27.4 days before moving on

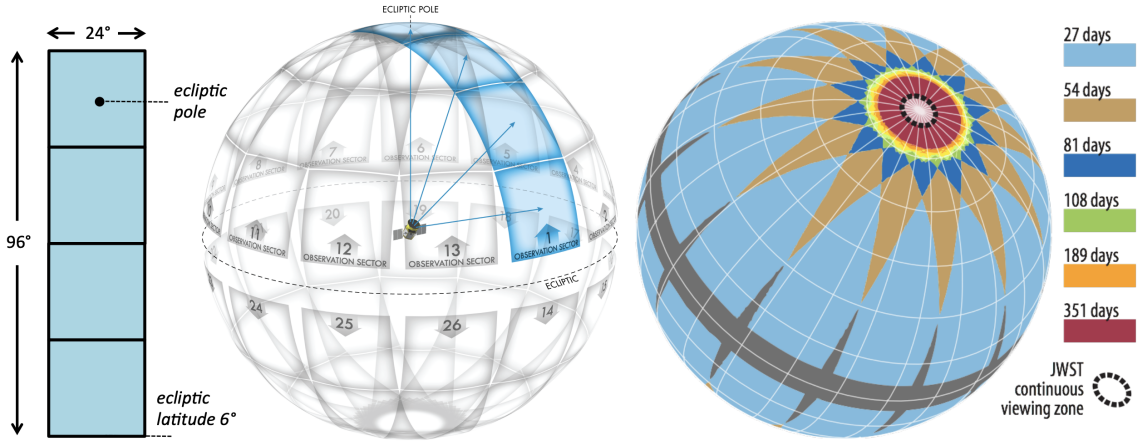

Figure 1.1: Graphics showing *TESS* field of view and how the sky is split up for observation. Left: *TESS* field of view with partitions per camera. Middle: sky partitions. Right: time each area of the sky will be observed for over an all-sky survey. Image credit: Ricker et al. (2014)

to the next sector, taking around a year to complete observing one whole hemisphere. During the course of observation of one hemisphere, the portion of sky around 12° from the ecliptic pole will is viewed continuously. This also means that areas of the sky near the ecliptic poles will generally receive more observation time as can be seen in the right panel of Figure 1.1. This project used *TESS* data at a cadence of 120 s. These images are obtained by taking 2 s exposures 60 times and summing them to give the effective exposure time of 120 s.

As mentioned in Section 1.1, we use impact parameter (b) instead of inclination (i) to describe where the companion crosses in front of the host star. As can be seen from Figure 1.2, an orbiting companion where the centre of the companion passes over the centre of the primary star from the point of view of an observer happens when b is zero and one when the centre of the companion grazes the edge of the host star. b is defined by Equation (1.1), where a is the semi-major axis of the orbit and R_1 is the radius of the primary star.

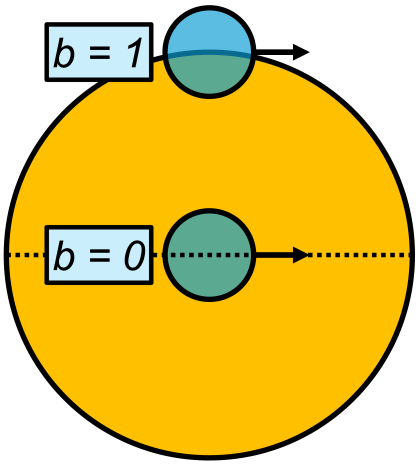

Figure 1.2: Schematic demonstrating the definition of the impact parameter, b. The yellow disk represents the primary star and the transparent blue disks represent a transiting companion at different corresponding impact parameters.

$$b = \frac{a}{R_1} \cos i \tag{1.1}$$

1.2.1 Using EBLMs to investigate M dwarf stars

Due to their intrinsic faintness, analysing M dwarf stars is difficult. At the start of the EBLM project, most observations that were used to calibrate M dwarf models relied on interferometry of nearby M dwarfs or double M dwarf eclipsing binaries (Gómez Maqueo Chew et al., 2014, and references within). EBLMs give the unique opportunity to investigate a much larger sample of M dwarfs. While finding masses and radii of the companion relies on models, as the primary F/G/K host is well understood in our sample of EBLMs, the errors introduced before using empirical relations should be minimal.

M-dwarfs have very complex spectra dominated by strong molecular bands so it is difficult to obtain their metallicity. In binaries however, we can use the fact that both stars will very likely have formed in the same region and are hence made from a similar

composition of matter. This means if we have the metallicity of one star in the binary we can assume that the companion star will have the same metallicity, allowing us to investigate the effects of metallicity, use this metallicity when using empirical relations to find masses and radii and not have to assume solar metallicity when comparing results with models.

1.2.1.1 The radius inflation problem

Within the range of M dwarf stars, evolutionary models show that stars become completely convective (Limber, 1958). This border between fully-convective stars and the start of radiative energy transport begins at stars of $0.35 M_{\odot}$ (Chabrier & Baraffe, 1997). We use this boundary to define stars with mass $\lesssim 0.35 M_{\odot}$ to be very low-mass stars.

It is often seen in literature that the radii determined from observations of cool stars (such as M dwarfs) are higher than those predicted by stellar models. This was first noted in Hoxie (1970) for low-mass main sequence star models. They observed radius inflation of up to 40% of the theoretical radius for their targets, leading many people to investigate this phenomena in the decades since. Much more recent investigations based on high precision light curves and radial velocity data are suggesting that this problem is much less serious than previously thought (Maxted et al., 2023). The EBLM project has worked to investigate this effect finding that systems with orbital periods greater than 5 days show radius inflation for very low mass M dwarfs $\leq 3\%$ (Swayne et al., 2023) when comparing to the MIST grids of stellar isochrones (Dotter, 2016; Choi et al., 2016). Similarly, Wanderley et al. (2023) also find their sample of M dwarf stars to show a subtle radius inflation from comparison with MIST models.

1.3 Limb darkening

The angle that we observe a star leads to variation in intensity of light that is measured from the centre to the limb by an observer. This effect is known as centre-to-limb variation or limb darkening. An example of what this looks like is shown in Figure 1.3 for the Sun through an optical filter. Most of the light emitted from a star comes from a region called the photosphere. For dwarf stars like the Sun, this is a narrow range of radius where temperature drops to a minimum moving outwards. This temperature gradient is directly related to the limb-darkening. So while the amount of star we see through remains approximately constant, a higher proportion of what we see comes from cooler areas of the star as we observe closer to the limb, seen in Figure 1.5. In light curves (LCs), this effect can easily be seen in the curved section between the second and third contact points, if there was no limb darkening, this section would appear flat however we do not observe this, as can be seen in Figure 1.4. Inaccurate treatment of limb darkening can lead to errors in estimating system parameters. For example, as can be seen from Figure 1.6 in modelling the light curve, in order for the case with no limb darkening to (on average) align with the limb darkened curves, the radius of the companion input to the transit model would have to be reduced. As methods to characterise stars from light curves and instruments collecting photometry become more precise, the need to accurately characterise limb darkening becomes more important to ensure unnecessary errors are not introduced.

1.3.1 Limb darkening laws

Many laws have been proposed to describe limb darkening. Some examples are listed below in terms of μ which is the cosine of the angle between the normal to the surface of the star and the line of sight of an observer.

[1] https://commons.wikimedia.org/wiki/File:2012_Transit_of_Venus_from_SF.jpg

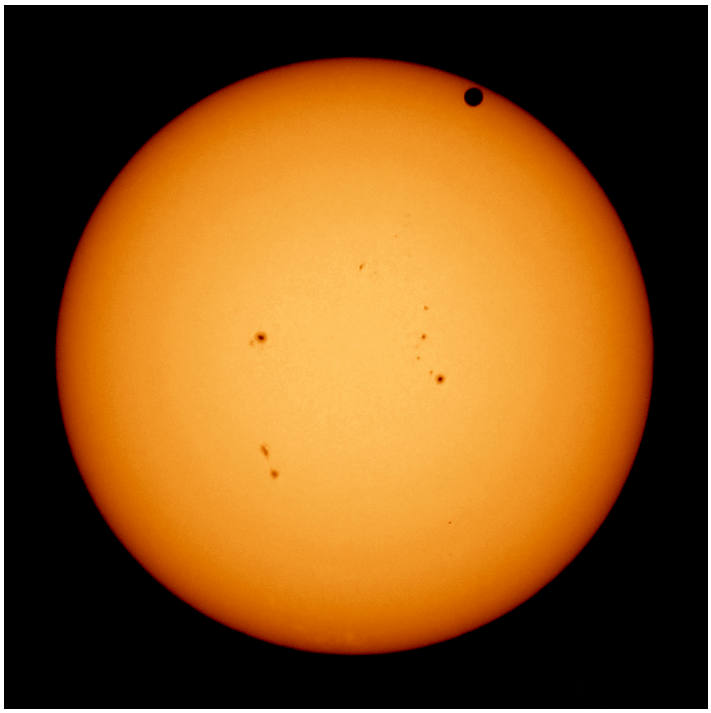

Figure 1.3: Image taken in the visible spectrum during the transit of Venus cross the Sun (2012) to show limb darkening. Image credit: Brocken Inaglory[1].

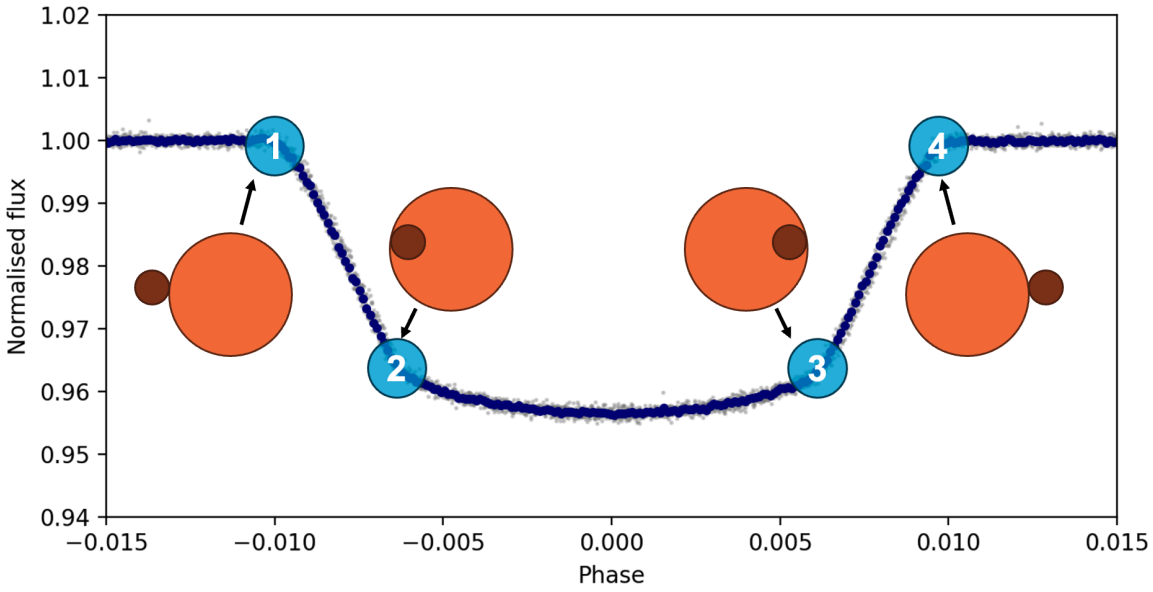

Figure 1.4: Labelled example primary eclipse light curve (*TESS* data for EBLM J0723+79). Numbers in blue circles give contact points of an eclipse. Schematics shown in orange is an example of what would be seen at that point in the light curve of an eclipsing companion from left to right. Point 1: point when companion first begins transiting. Point 2: the full disk of the companion is first over the host. Point 3: companion starts to leave the disk of the host. Point 4: companion no longer eclipses the host.

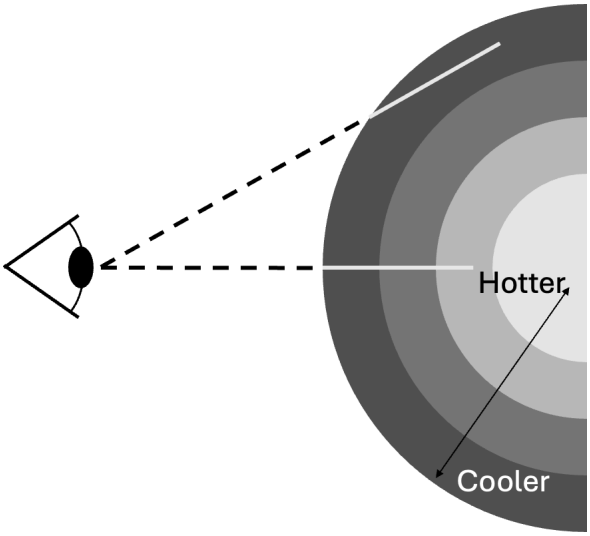

Figure 1.5: Diagram to illustrate why we observe limb darkening. Image not to scale and representative of the photosphere of a star. The white lines inside the star are approximately the same length.

$$I_\lambda(\mu) = 1 - c\,(1 - \mu) \tag{1.2}$$

$$I_\lambda(\mu) = 1 - c\,(1 - \mu^\alpha) \tag{1.3}$$

$$I_\lambda(\mu) = 1 - \sum_{j=1}^{4} a_j (1 - \mu^{j/2}) \tag{1.4}$$

Equation (1.2) is known as the linear limb darkening law (Schwarzschild, 1906). This was the first law proposed to describe limb darkening, from observations of the Sun. The coefficient c determines the limb darkening profile.

Equation (1.3) is known as the power-2 law (Hestroffer, 1997). The coefficients c and α determine the limb darkening profile. The power-2 limb darkening law is explored further in Section 1.3.2.

From the light curves of star and planetary transits we are able to obtain information about the limb darkening of the primary star. If we are to compare with stellar atmosphere models, we want to make as few assumptions about the limb darkening

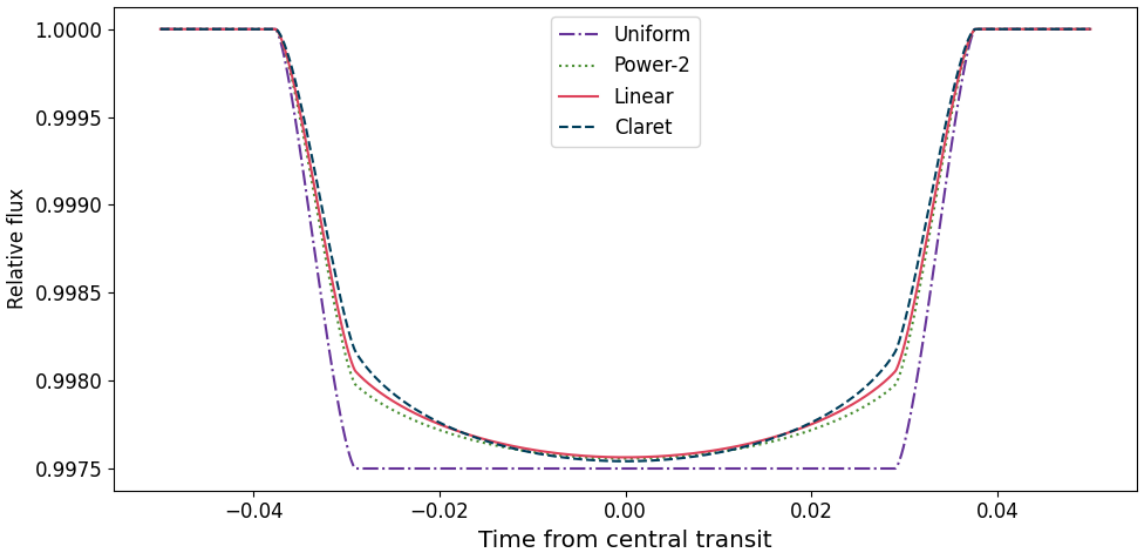

Figure 1.6: Light curves predicted by linear, power-2 and the Claret 4-parameter law for $h_1' = 0.833$ and $h_2' = 0.201$ in comparison to no limb darkening. Purple dot dashed line: uniform disk (i.e. no limb darkening). Solid red line: linear limb darkening (Equation (1.2)). Light green dotted line: Power-2 law (Equation (1.3)). Dark green dashed line: Claret law (Equation (1.4)). Period = 5 days, companion:host radius = 0.05, semi-major axis in terms of stellar radius = 14.9, inclination = 87°, eccentricity = 0. Generated using the `BATMAN` transit model (Kreidberg, 2015).

of the star as possible. The limb darkening law used in this project was the Claret 4-parameter limb darkening law (Claret, 2000) shown in Equation (1.4). This law allowed us to capture as much of the true shape of the limb darkening profile as possible due to its flexibility (Espinoza & Jordán, 2016). The coefficients a_1, a_2, a_3, a_4, here represented by a_j determine the limb darkening profile.

The coefficients in these laws do not represent a physical parameter of the star or system, they simply determine the shape of the limb darkening profile for their respective laws.

1.3.2 The Power-2 law

The power-2 law has been identified as the best 2 parameter limb darkening law especially for cooler stars (Morello et al., 2017). This law can be very useful when analysing cool stars, like the primary star in EBLMs. As it is only two parameters, Bayesian methods are able to sample the limb darkening parameters faster than four parameter laws, however, to specifically investigate limb darkening this law is not flexible enough to capture the true profile. This is discussed further in Section 1.3.3.

In Maxted (2018) the summary parameters h_1 and h_2 were defined.

$$\begin{aligned} h_1 &= I_\lambda(1/2) \\ h_2 &= h_1 - I_\lambda(0) \end{aligned} \tag{1.5}$$

This selection of h_1 and h_2 gives much less correlated parameters allowing easy comparison to grids of stellar parameters when using the power-2 law. This selection of h_1 and h_2 however has some drawbacks that cannot be ignored. This is talked about further in Section 1.3.3.

1.3.3 Claret's 4-parameter limb darkening law

This project mainly uses the Claret 4-parameter law or non-linear limb darkening (subsequently referred to as the "Claret law") as it is the law that gives us enough flexibility to capture the true limb darkening profile (Espinoza & Jordán, 2016). Unlike

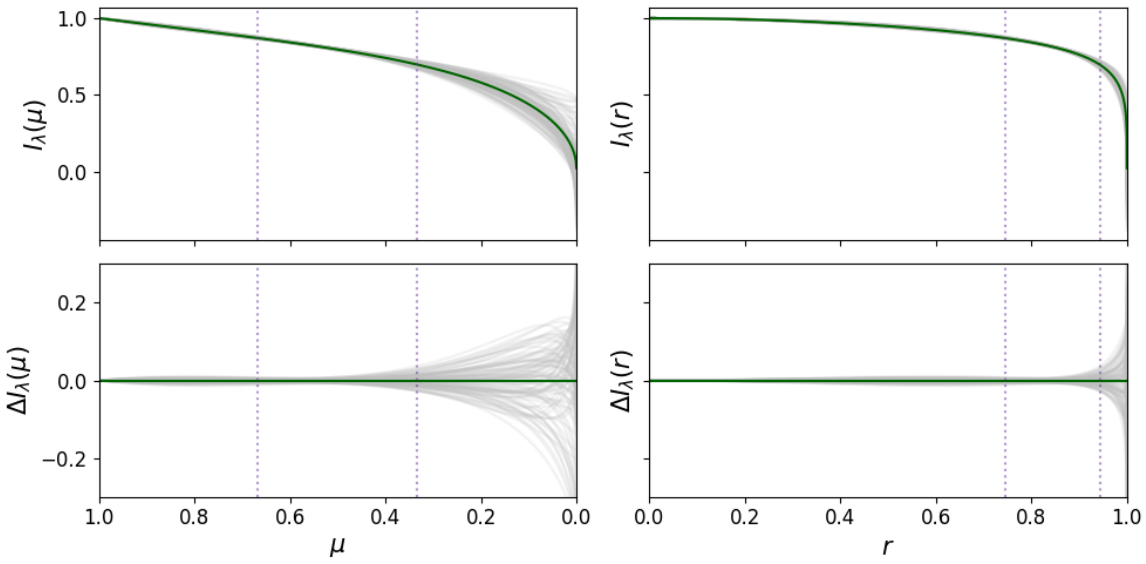

Figure 1.7: The Limb-darkening profiles from a fit to the light curve for J0723+79 was sampled using `EMCEE` and the intensity profile for the best fit and a random sample of 100 tested parameters plotted. The left panels show the intensity as a function of μ. The right panels show the intensity as a function of radius. The grey lines are calculated the values of the Claret limb darkening coefficients recovered from a random selection of 100 chains. The green line gives the profile calculated with best fit parameters. The purple dotted lines show where in the profile h_1' and h_2' are dependant.

the power-2 law, the Claret law allows us to have large uncertainties at the edges of the star where the light curve contains less information about the limb darkening profile.

Negatives to using the Claret law is that the coefficients $a_1, \ldots, a_4$ are highly correlated. The value chosen for one of the coefficients will greatly affect the values of the others that fit and multiple sets of values can produce the same or similar profile (Morello et al., 2017; Maxted, 2023). This can cause a problem when trying to compare the resultant coefficients from a fit to stellar atmosphere models. The summary parameters h_1 and h_2 could be used for comparison instead however the definition of h_2 causes problems. h_2 is dependent on the intensity at $\mu = 0$ and as can be seen in Figure 1.7, at this value of μ the limb darkening profile is not well constrained by the light curve data.

Instead the transformed parameters h'_1 and h'_2 were defined in Maxted (2023).

$$\begin{aligned} h'_1 &= I_\lambda(2/3) \\ h'_2 &= h'_1 - I_\lambda(1/3) \end{aligned} \tag{1.6}$$

Their dependencies are given in Figure 1.7 by the purple dotted lines. Here we can see that the profile is much more well defined. Looking at the left panels, one might try to convince oneself that the limb darkening profile is generally not well defined for the final third section of the star, however this is not truly the case. μ scales as $\sqrt{1-r^2}$ where r is the linearly scaled radius of the star such that the centre is set at 0 and the limb at 1. This means that this region where the profile is not well defined is actually only a small portion ($\sim 6\%$) of the profile right near the limb is not well defined. This is shown in the right hand side set of panels.

1.3.4 Measuring limb darkening

Even the closest exoplanet host stars are barely resolved by the current generation of long-baseline optical interferometers, we cannot directly see a star's limb darkening profile. Transiting companions offer a chance to measure this effect. As a companion transits across a host star, a section of the flux from the host is blocked out meaning the flux across the radius of the host can be sampled.

Maxted (2023) uses transits of hot Jupiters to parameterise limb darkening. Due to the properties of hot Jupiters, we can assume the following two things.

- The hot Jupiter is appears as a circular opaque disc with a well-defined edge.
- As it is cool, the flux emitted from the hot Jupiter is negligible.

Maxted (2023) Uses this technique of measuring limb darkening, which this project follows on from. A negative to only using transiting hot Jupiters is that Jupiter mass exoplanets have been proven to more commonly orbit metal rich stars and has been investigated thoroughly across the years. After the discovery of the first four exoplanets, it was already suggested there was a trend between the likelihood of a giant

planet orbiting a star (Gonzalez, 1997) and soon after efforts were made to quantify this (Santos et al., 2000, 2001). Adibekyan (2019) provides their own study finding that Jupiter mass planets are more likely to orbit metal rich stars than metal poor stars. Osborn & Bayliss (2020) more recently confirm that hot Jupiters are more likely to orbit high metallicity stars than low metallicity stars. It is hence important to extend our range of metallicities to investigate whether there are any trends in the limb darkening profile with respect to the metallicity. EBLMs offer a chance for this as they have very similar properties to transiting hot Jupiters so similar assumptions can be made. By definition they were originally flagged as false positive hot Jupiter transits (Triaud et al., 2017). But they do not appear to suffer as much from this same metallicity bias. The distributions of the metallicities of the EBLM targets investigated in this project vs the hot Jupiter targets in Maxted (2023) is shown in Figure 1.8 (using the data in Table 4.1 for the targets characterised in this thesis and data from Table 1 of Maxted (2023) for their targets). For their sample of stars the skew to a higher metallicity can be seen where as our systems show a peak closer to solar metallicity with each sample a mean metallicity of $+0.147$ and -0.092 respectively.

EBLMs tend to show secondary eclipses, they cause a dip in flux on the order of $\sim 0.1\%$ versus the flux when neither star is eclipsed. This is enough such that we are able to characterise these secondary eclipses, helping confirm eccentricities from radial velocity analysis and estimate eccentricities that have not been measured yet.

1.4 Atmospheric models

Three types of atmospheric model treatment were initially investigated. These models are called 1D plane-parallel, 1D spherically-symmetric and 3D radiative hydrodynamic. This project ultimately focused on limb darkening profiles calculated from 1D plane-parallel and 1D spherically-symmetric models so the final type of model is not discussed. Each of these models comes with a set of assumptions and approximations which are covered in the subsequent subsections.

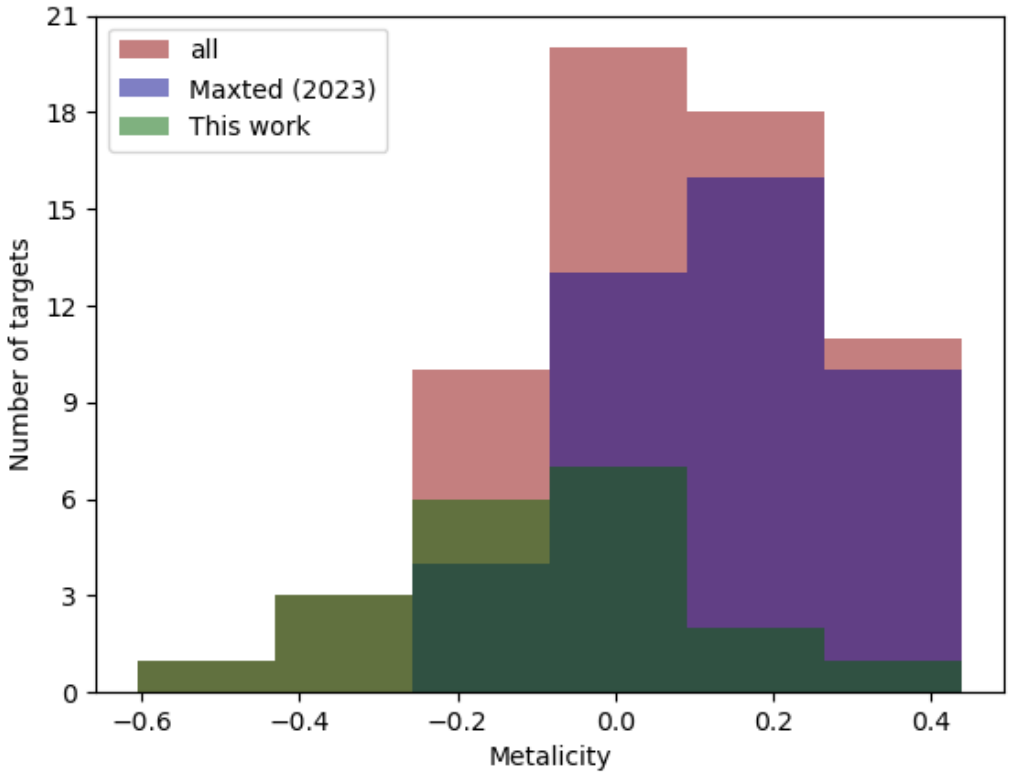

Figure 1.8: Histogram showing distribution of metallicities of targets used in this project compared to those used in Maxted (2023).

An important first step in discussing atmospheric models is to define what we consider a stellar atmosphere. The lecture series by Niemczura et al. (2014) provides useful summaries of building stellar atmosphere models and defines the stellar atmosphere as the external layers from which radiation is able to escape freely. This is the region from which we observe all photons coming from a star so a basic understanding of how these models are formed is important when discussing how well they describe limb darkening.

A general stellar atmosphere model is dependant mostly on effective temperature, composition, surface gravity and radius. All of the models we have used assume local thermodynamic equilibrium (LTE) because this is much simpler than non-LTE calculations. Non-LTE can be used to compute the strength of specific emission lines using radiative transfer calculations for an atmospheric structure computed using LTE.

Inside stars, energy is transported via convection or radiation. In radiative transfer, energy in the form of electromagnetic radiation travels through the medium of the star. In convection, hot matter floats to the surface, cools and sinks back down. Modelling convection is computationally very expensive so instead mixing length theory is used to approximate the transport of energy due to the movement of matter. Both models investigated here use this approximation. Mixing length theory says that energy transport is achieved by a bubble of gas raising in the atmosphere of a star and after it has travelled a certain length, the energy is dispersed (Böhm-Vitense, 1958, 1960; Smalley, 2014).

Both of these models also ignore the affects of magnetism within the star. The main difference between 1D plane-parallel and 1D spherically-symmetric models is that the latter account for the curvature of the photosphere. While I previously stated that radius is an important part of an atmospheric model, for the very low mass stars investigated in this project, this is much less important than for much more massive stars. The pressure scale height is the distance over which the pressure reduces by a factor of Euler's number. As the atmospheres of high mass stars are inflated compared to very low mass stars, the scale height is a large fraction of the overall radius, where as for very low mass stars, the scale height is much less than the radius meaning the

radius becomes less relevant when modelling atmospheres for these stars.

The two models investigated in this thesis use the grids of limb darkening parameters calculated by Claret (2018) for the PHOENIX-COND model and parameters calculated by Kostogryz et al. (2022) for their MPS-ATLAS model. Here "MPS" stands for Merged Parallelised Simplified, referencing that their code calculates components of their model simultaneously allowing the code to run faster than previous models. PHOENIX-COND is how Claret (2018) refers to the code from Husser et al. (2013).

1.4.1 1D plane-parallel

The stellar atmosphere is typically representative of a small portion of the radius (LeBlanc, 2010), hence the atmosphere can be considered very thin. This assumption is especially true for the lower mass stars studied in this sample that do not suffer from the same inflated atmosphere as their massive counterparts. Because of this, we can consider the gravity in this layer to be constant and quantities to not be dependant on radius. This means plane-parallel models ignore the curvature of the star they are modelling, massively simplifying equations of state that have to be solved.

1.4.2 1D spherically-symmetric

Spherically-symmetric models use spherical shells to model the atmosphere hence allowing a dependence on radius. This means the models are able to replicate the sharp characteristic reduction in the specific intensity at the limb of the star very well unlike 1D plane-parallel models (Claret, 2018). This often means that the definition of the limb of the star when using different types of models can be in different places. In this project, the limb darkening parameters predicted by the spherically-symmetric model in Claret (2018) were scaled as in Maxted (2023).

As discussed above, we are not able to very accurately characterise the region close to the limb of the star As this area accounts for such a small percentage of the star's radius, perfect characterisation of this area is not necessary to consider here.

1.5 Markov chain Monte Carlo sampling

1.5.1 Sampling theory

MCMC sampling allows us to generate random points in the parameter space that sample a multi-dimensional probability distribution. This is a very powerful tool for sampling multi-parameter models where direct sampling of the parameter space is difficult or not possible.

Bayes' theorem can be used to formulate the relationship between a model and some data that is to be fit (Equation (1.7)). Here we will take θ to represent the parameter set for some model and D to represent some data.

$$P(\theta|D) = \frac{P(D|\theta)P(\theta)}{P(D)} \tag{1.7}$$

In Equation (1.7) P is the probability of an event occurring, and $P(\theta|D)$ is the probability of the model given the data and vice versa. $P(D|\theta)$ can be thought of as the likelihood of the data fitting that iteration of the model, also referenced as: $\mathcal{L}$. $P(\theta|D)$ is the "posterior" (i.e. what we are aiming to sample), also referenced as $\mathcal{P}$. $P(\theta)$ contains information about the data we already know such as pre-published parameters and is known as the "prior", also referenced as ρ. $P(D)$ is called the "evidence" and is constant if we are comparing different models with the same data, so is often ignored in this type of analysis.

Here I will briefly discuss two MCMC algorithms: Metropolis–Hastings (Metropolis et al., 1953; Hastings, 1970) and Goodman-Weare (Goodman & Weare, 2010). The first gives an introduction to the iterative method of MCMC algorithms, while the second is a more advanced algorithm that avoids some of the problems with "classic" MCMC.

The Metropolis–Hastings algorithm involves the following steps. First a random point in the parameter space is chosen as an initial point, x_1. The posterior is calculated at this point and then the following steps are iterated over.

- Take the previous number in the chain as x_n
- A second point is chosen randomly from x_n as a "step", x_{n+1} such that the chance of x_{n+1} being selected after x_n is the same as the chance of x_n being selected after x_{n+1}.
- The posterior is calculated for this new point.
- A random number between 0 and 1 is generated, y.
- If the posterior probability of x_{n+1} is **greater than** the posterior probability of x_n: the step is accepted.
- If the posterior probability of x_{n+1} is **less than** than the posterior probability of x_n **but** the ratio of posterior x_{n+1} to posterior x_n is greater than y: the step is accepted.
- Else: the step is rejected and x_{n+1} is instead taken as x_n again (i.e. x_n is repeated in the chain).

The Metropolis–Hastings algorithm does have a few drawbacks. For models with large numbers of parameters to fit, the computational time before convergence becomes very long. When trying to deal with parameters that are highly correlated, complex calculations to change coordinate system or specific decisions about how each step is taken may be necessary to reduce convergence time.

The `EMCEE`[2] (Foreman-Mackey et al., 2013) package uses the Goodman-Weare algorithm to perform MCMC sampling. This particular method is very useful as it is affine-invariant, this means that the coordinate space that is chosen to sample does not affect how the space is sampled. A number of so called "walkers" wander the parameter space taking "steps" determined by the likelihood term in Equation (1.7) and the position of the other walkers. As the movement of the walkers in `EMCEE` is

[2] `https://emcee.readthedocs.io/`

not dependant on the coordinate system, each step is usually referred to as a "jump" At each of these jumps, the posterior is evaluated (i.e. a set of parameters are chosen and the likelihood and prior terms are calculated hence the posterior for that point in the parameter space). In this analysis we are able to directly measure the parameters sampled from the light curve, meaning the parameter space is uncomplicated making `EMCEE` a good choice to use to sample the posterior.

A set of starting parameters are given and walkers placed in an n-dimensional ball around the point (n being the number of parameters varied by the sampler). The walkers are initially placed tightly around this point, ensuring the walkers are less likely to get stuck in areas of low probability. The parameters selected should be near where we expect the area of maximum likelihood to be however accurate estimates are not always available. For these reasons, the walkers are first given a period of burn-in. This burn-in phase is completed when there are no trends in the mean and variance of the chains and the chains from each walker look similar to each other. As with the Metropolis–Hastings algorithm, this method does not solve convergence time problems caused by multiplicity.

1.5.2 Likelihood and priors

If we assume uncorrelated Gaussian noise for the light curve data then we can compute the likelihood using Equation (1.8). In this equation, we assume that the quoted errors on the light curve data, Δx, are underestimated by some factor f. x is the input flux and μ is the flux predicted by the model.

$$\mathcal{L} = \frac{1}{\sigma\sqrt{2\pi}} \exp\left(-\frac{1}{2}\left(\frac{x-\mu}{\sigma}\right)^2\right) \tag{1.8}$$

$$\text{where} \quad \sigma = f\,\Delta x$$

For n data points the equation becomes Equation (1.9), assuming all data points

have the same standard error, σ.

$$\mathcal{L} = \left(\frac{1}{\sigma\sqrt{2\pi}}\right)^n \prod_{i=1}^{n} \exp\left(-\frac{1}{2}\left(\frac{x_i - \mu_i}{\sigma}\right)^2\right) \tag{1.9}$$

$$\ln(\mathcal{L}) = -n\ln(\sigma) - \frac{1}{2}\sum_{i=1}^{n}\frac{(x_i - \mu_i)^2}{\sigma^2} \tag{1.10}$$

Taking the natural log of both sides simplifies the equation to Equation (1.10). Where $\sum_{i=1}^{n}\frac{(x_i-\mu_i)^2}{\sigma^2} = \chi^2$ producing Equation (1.11).

$$ln(\mathcal{L}) = -n\ln(\sigma) - \frac{1}{2}\chi^2 \tag{1.11}$$

For the priors, there are generally two different types that can be applied during MCMC analysis: flat or functional. So-called flat priors apply a uniform probability of a solution being in a large range around an estimate of the parameter value, or the full allowed range of the parameter if there are physical limits. Functional priors assume some function dictates the probability. In this project Gaussian priors were used on e and ω where independent estimates of these parameters were available from an analysis of the spectroscopic orbit. This is shown in Equation (1.12) where n is the number of parameters we are applying Gaussian priors to, x is the fit parameter being tested, y is the initial input parameter and Δy is the standard deviation of the normalised distribution which can be characterised by the standard error.

$$\ln(\rho) = \sum_{i=1}^{n} -\frac{1}{2}\frac{(x_i - y_i)^2}{\Delta y_i^2} \tag{1.12}$$

For the case where prior values on e were not available, and the time of mid secondary eclipse visibly deviated from 0.5, non uniform priors were applied to $e\cos(\omega)$ and $e\sin(\omega)$ to ensure that the implied prior on e is uniform while varying $e\cos(\omega)$ and $e\sin(\omega)$. The transform on the probability distribution function is given by Equation (1.13) as follows from methods describing prior calculations outlined in Carter et al. (2008).

$$f(e\cos\omega, e\sin\omega) = \frac{g(e,\omega)}{|\mathbf{J}|} \tag{1.13}$$

Here, $g(e, \omega)$ is the combined probability distribution function on e and ω, $f(e\cos\omega, e\sin\omega)$ is the combined probability distribution function on $e\cos\omega$ and $e\sin\omega$ and $|\mathbf{J}|$ is the Jacobian determinant of the matrix (1.14) given in Equation (1.15).

$$\begin{vmatrix} \partial(e\cos\omega, e\sin\omega) \\ \partial(e, \omega) \end{vmatrix} \tag{1.14}$$

$$|\mathbf{J}| = \begin{vmatrix} \frac{\partial e\cos\omega}{\partial e} & \frac{\partial e\sin\omega}{\partial e} \\ \frac{\partial e\cos\omega}{\partial \omega} & \frac{\partial e\sin\omega}{\partial \omega} \end{vmatrix} = e \tag{1.15}$$

Dividing the prior distribution, e and ω by the eccentricity gives the prior distribution that is uniform for $g(e, \omega)$ but non uniform for $f(e\cos\omega, e\sin\omega)$.

The posterior distribution is then determined by the following equation by taking the natural log of Equation (1.7).

$$\ln(\mathcal{P}) = \ln(\mathcal{L}) + \ln(\rho) \tag{1.16}$$

2 Pre-analysis

2.1 Light curve processing

2.1.1 Target selection

The initial list of targets were taken from objects of interest found in the BEBOP survey (Martin et al., 2019) and the EBLM project (Triaud et al., 2017). I use short-cadence (120 s exposures) *TESS* data for my analysis so targets without this were excluded. Accurate limb-darkening measurements need a lot of high-quality data in order to increase the signal-to-noise ratio. Having multiple visits of transit data allows the light curves to be folded at the period, increasing the signal to noise ratio. Data for targets were downloaded using their *TESS* input catalogue identifier (TIC ID) cross referenced using Simbad[1]. This folded light curve was visually inspected to ensure the primary eclipses were central around time zero and all the eclipses were aligned.

The number of sectors of *TESS* data was checked using `LIGHTKURVE`[2] (Lightkurve Collaboration et al., 2018). Generally, if there were less than three sectors of *TESS* data or an orbital period longer than 15 days, a system would be excluded as there would not be enough transits to measure the limb darkening profile in any detail. The long period system EBLM J1705+55 ($P \approx 23$ days) was included as it had 21 sectors of *TESS* data. A high proportion of targets selected were near the ecliptic poles as *TESS* observes this location more often, hence, there is more data.

Systems with $b > 0.8$ were excluded as secondary stars that transit too far from the centre of the primary star do not probe enough of the stars surface to obtain accurate limb darkening parameters (Müller et al., 2013). Of the targets left, if there was published evidence of drift in the radial velocities due to a third body, the system was excluded to simplify interpretation of the results. The list of selected targets is in Section 3.1.1, Table 3.2

[1] `https://simbad.cds.unistra.fr/simbad/` [2] `https://docs.lightkurve.org/`

2.1.2 Data processing

TESS pre-search data conditioning simple aperture photometry (PDCSAP) with a cadence of 120s were downloaded using `LIGHTKURVE`. As `LIGHTKURVE` downloads *TESS* sectors separately, the light curves were first combined.

Outliers 10 sigma from the median of the data set were excluded. Either side of the time of mid primary eclipse, data within 1.5 times the primary eclipse duration were kept for fitting. Similarly for the secondary eclipses, data within 1.5 times the secondary eclipse duration was kept.

For each primary and each secondary eclipse, a straight line was fit to the data either side of each eclipse and divided through the data to bring all the data onto a consistent flux scale. Each of the primary and secondary eclipses found were plotted with the straight line fits to visually check: the fit was sensible, the eclipses were being aligned correctly and to look if any cycles containing bad data that could add noise or new signals had been included. With the primary eclipses for each visit converted in terms of phase to overlay multiple visits, the data were binned in 120s intervals. Unbinned data points that fell outside of 5 times the standard error on their bin were removed. This was repeated for the secondary eclipses. The data for the primary and secondary eclipses were then saved into separate files. An example for EBLM J0723+79 is shown in Figure 2.1. The vertical green dashed lines allowed me to check the initial estimate of the eclipse width was correct and the horizontal yellow dashed line allowed me to check the initial estimate of the eclipse depth.

2.2 Atmospheric parameters

For analysis of stellar densities and comparing limb darkening parameters measured to atmospheric models, access to effective temperatures ($T_{\rm eff}$), log of the gravities ($\log g$) and metallicities ([M/H]) was necessary. Analysis of stellar densities is described in section 5. Limb darkening model comparisons are available in section 4.

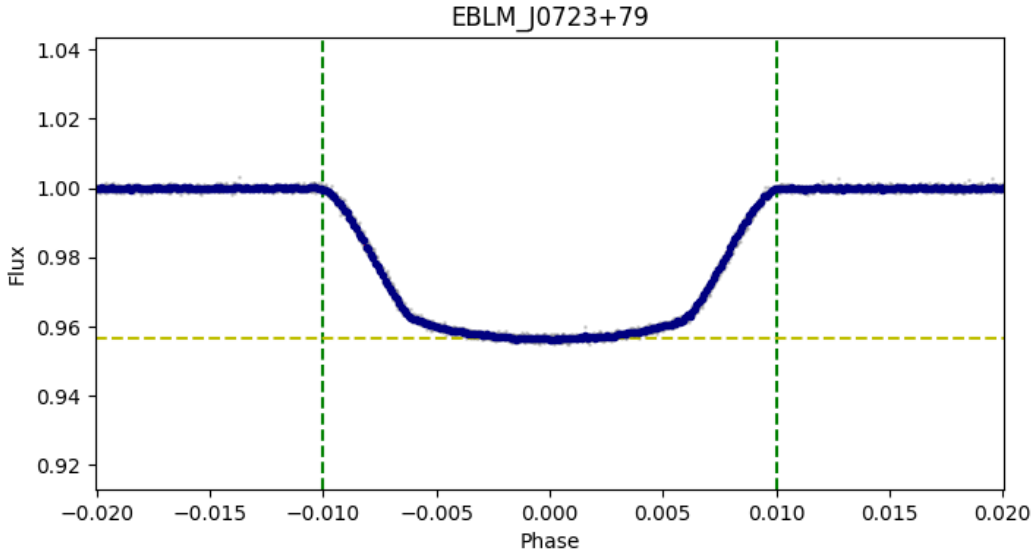

Figure 2.1: Cleaned primary eclipse light curve for EBLM J0723+79 folded at the orbital period of the binary. The horizontal yellow dashed line gives the initial estimate of the primary eclipse depth and the difference between the vertical green dashed lines gives the initial estimate of the primary eclipse width.

2.2.1 Finding a data set

A large portion of the target stars appear in The Gaia survey, data release 3 (GDR3) (Gaia Collaboration et al., 2021) so this sample was considered to provide atmospheric parameters. To test the accuracy of the atmospheric parameters provided by GDR3, a catalogue of published parameters for exoplanet hosts was used. SWEET-Cat (Santos et al., 2013; Sousa et al., 2021) aims to provide a largely homogeneous catalogue of these parameters. Parameters not from the homogeneous data set are generally taken from high quality spectral analysis however sometimes, where none of the previously mentioned sources were available, parameters from other methods are used such as from photometry or asteroseismology.

The list of targets for this comparison was taken from Maxted (2023) as they were known to appear in SWEET-Cat across a similar range of temperatures as the

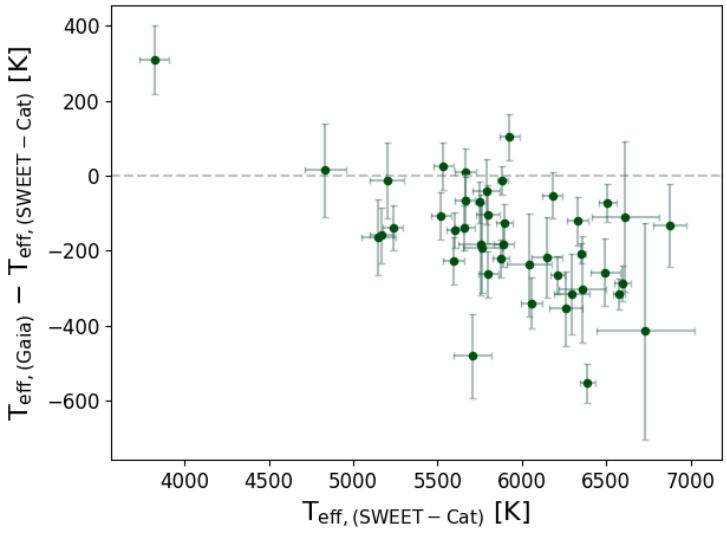

Figure 2.2: Graph comparing Gaia model $T_{\rm eff}$ to spectroscopic $T_{\rm eff}$ listed in SWEET-Cat

targets selected for analysis. The metallicities from GSP-Phot were re-calibrated using `gdr3apcal`[3] as Andrae et al. (2022) found significant offsets between literature and the model values.

Andrae et al. (2022) found, over their sample of stars, an average difference of 110 K and $0.2 - 0.25$ (for $T_{\rm eff}$ and $\log(g)$ respectively) between model and literature values. Across our sample the mean average difference in $T_{\rm eff}$ was found to be 187 K with only 18.6% of Gaia values within one error bar of literature values. Versus the mean average error on the effective temperatures determined by Gaia of around 19 K, the average difference is very significant.

Figures 2.2, 2.3 and 2.4 show the difference between literature values and the Gaia model parameters for 43 test stars with at least one orbiting exoplanet. In the sample of targets, literature parameters for 15 came from the homogeneous study (Sousa et al., 2021), 24 came from alternative high quality spectral analysis and 4 came

[3] `https://mpi-astronomy.github.io/gdr3apcal/`

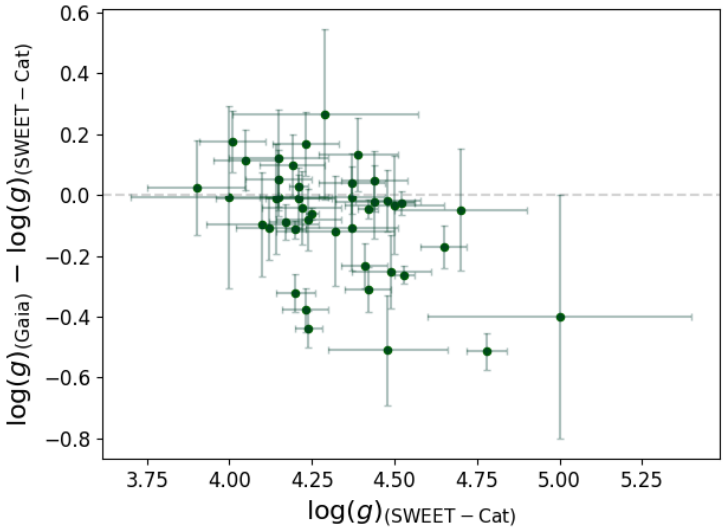

Figure 2.3: Graph comparing Gaia model $\log(g)$ to spectroscopic $\log(g)$ listed in SWEET-Cat

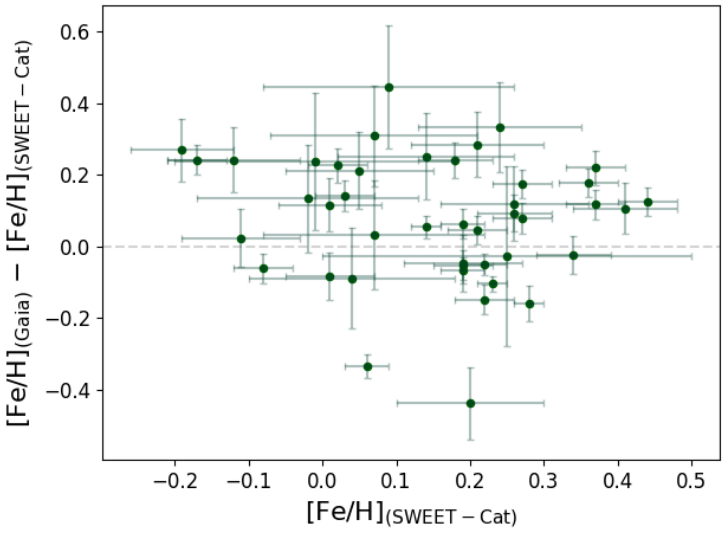

Figure 2.4: Figures comparing Gaia model metallicities to spectroscopic metallicities listed in SWEET-Cat

from photometry.

The mean average difference in $\log(g)$ was 0.142 with 53.5% of targets within one error bar of literature values. When considering the mean average Gaia error on $\log(g)$ of 0.016, this discrepancy is very significant.

The metallicity had a mean average difference of 0.158 with only 18.6% of values within one error bar of literature values. The mean average error on the metallicities produced by Gaia was around 0.02 so when considering the difference between Gaia and literature, the average difference is very significant

Estimates for $\log(g)$ offered the most consistent values but both $\log(g)$ and $T_{\rm eff}$ a seemingly linear offset trend with some scatter between Gaia models and literature across our sample. Often the $T_{\rm eff}$ and $\log(g)$ predicted by Gaia was too low in comparison to literature especially for higher temperatures and values of $\log(g)$ respectively. Before this conclusion could truly be drawn, a larger sample at lower $T_{\rm eff}$ to fill the gap and higher $\log(g)$ would be necessary, this however was beyond the scope of this project. As the M dwarf in the binary contributes less than 1% of the flux in the wavelength we are observing at, we could expect similar offsets in EBLM systems. There is no discernible trends in the metallicity predicted by Gaia with a large scatter around predictions being too high or too low.

In conclusion the offset, especially in $T_{\rm eff}$, was too large to reliably use the temperatures, gravities and metallicities from Gaia in this project. Until this offset is understood we cannot recommend using these parameters from Gaia for F/G/K stars with companions. Parameters calculated from high quality spectroscopy are required.

3 Light curves

3.1 Calculating light curves

The transit and eclipse models in the Python package `BATMAN`[1] version 2.4.9 by Kreidberg (2015) were used to analyse the light curve data for the selected EBLM systems. Characteristic parameters of the selected targets are given in Table 3.1. Spectral type in Table 3.1 are assigned according to Pecaut & Mamajek (2013)

3.1.1 Starting parameters

For each star, the following orbital parameters were collected: time of mid primary eclipse, T_0; period, P; primary and secondary eclipse width and depth; impact parameter, b; phase of secondary eclipse. These were used to calculate initial values for the free parameters. Values for P were collected from literature from the references as shown in Table 3.1, and where available, b was used from the same source. Where no value for b was available, 0.5 was used as high impact parameter systems were filtered out of the sample in Section 2. The rest of the parameters listed above were estimated by looking at the LCs.

The primary eclipse depth, D, and secondary eclipse depth, L, can be used to calculate an initial estimate of the secondary-primary star radius ratio, k.

$$k = \frac{R_{sec}}{R_{pri}} = \sqrt{\frac{D}{1-L}} \tag{3.1}$$

This equation can however be simplified in this case. As L for EBLMs is very low (on the order of 0.001 normalised flux units), k can be approximated to Equation (3.2).

$$k = \sqrt{D} \tag{3.2}$$

[1] `http://lkreidberg.github.io/batman/docs/html/index.html`

Table 3.1: Characteristic parameters and labels of targets for reference. Target EBLM and TIC IDs; magnitudes in the TESS band; Effective temperature gravity and metallicity of the primary star (for references see Table 4.1; masses and radii of stars found in Section 5; orbital periods with references as footnotes. Numbers in brackets are the errors on the final digits.

EBLM ID	TIC ID	TESS mag.	Approximate spectral type	$T_{\rm eff}$[K]	$\log(g)$	[M/H]	M_1	R_1	M_2	R_2	Period
J0228+05	422844353	9.86	F2V	6912(134)	4.15(14)	+0.08(8)	1.38(9)	1.53(4)	0.168(7)	0.196(5)	6.6347[a]
J0247−51	231275247	9.11	F8V	6130(191)	3.97(12)	−0.43(33)	1.20(8)	1.76(4)	0.224(9)	0.241(6)	4.0079[a]
J0400−51	237342298	11.77	F9V	6010(180)	3.96(10)	−0.21(19)	1.17(8)	1.64(4)	0.254(11)	0.271(6)	2.6921[a]
J0432−33	170749770	10.7	F8V	6166(134)	3.55(14)	−0.61(5)	1.27(9)	2.13(5)	0.254(11)	0.258(7)	5.30553[a]
J0440−48	259470701	11.06	F8V	6113(286)	4.08(13)	−0.31(37)	1.20(8)	1.72(4)	0.182(8)	0.218(5)	2.543[a]
J0500−46	161577376	11.31	G2V	5788(116)	4.22(18)	−0.15(5)	1.08(7)	1.37(4)	0.171(7)	0.202(5)	8.28444[a]
J0526−34	24397947	10.76	F6V	6307(128)	3.97(15)	−0.05(7)	1.33(9)	1.98(5)	0.335(14)	0.327(8)	10.1909[a]
J0608−59	260128333	11.49	G1V	5865(103)	3.69(25)	+0.01(5)	1.10(8)	1.31(3)	0.307(13)	0.306(7)	14.6085[a]
J0625−43	232030067	11.48	G4V	5678(118)	4.01(12)	−0.10(16)	1.13(8)	1.75(4)	0.287(12)	0.304(7)	3.969[a]
J0627−67	167201539	10.97	F5V	6498(117)	4.24(27)	−0.16(13)	1.22(8)	1.33(3)	0.216(9)	0.226(5)	9.4689[a]
J0709−52	343963409	12.53	F8V	6097(312)	3.96(10)	−0.21(39)	1.31(9)	2.17(5)	0.398(16)	0.394(10)	9.108[a]
J0723+79	289949453	8.71	F9V	6014(121)	4.01(19)	−0.08(3)	1.14(8)	1.40(3)	0.265(11)	0.278(6)	13.2177[b]
J0829+66	102841799	11.32	G7V	5635(126)	4.13(15)	+0.16(6)	1.01(7)	0.91(2)	0.185(9)	0.204(5)	5.2604[b]
J0941−31	25776767	10.64	F3V	6686(134)	3.77(18)	−0.26(4)	1.36(9)	1.86(5)	0.24(1)	0.249(6)	5.54563[a]
J0955−39	45599777	12.37	F7V	6223(165)	3.90(66)	+0.32(22)	1.16(8)	1.05(3)	0.218(9)	0.226(6)	5.3136[d]
J1626+57	207493152	10.06	G0V	5968(118)	3.92(17)	+0.04(4)	1.15(8)	1.45(3)	0.180(9)	0.212(5)	9.1276[b]
J1640+49	274238240	9.97	F5V	6459(127)	3.76(17)	+0.01(4)	1.36(9)	1.93(5)	0.209(12)	0.232(6)	6.2062[b]
J1705+55	198358825	11.44	G3V	5706(112)	3.63(19)	−0.15(6)	1.09(8)	1.51(4)	0.33(3)	0.305(8)	23.5144[b]
J1850+50	48191564	11.74	G1V	5830(103)	3.63(16)	+0.24(4)	1.21(8)	1.78(5)	0.30(3)	0.282(8)	9.5692[c]

[a]Triaud et al. (2017)
[b]Collins et al. (2018)
[c]Schanche et al. (2019)
[d]Swayne et al. (2023)

The estimate of the orbital semi-major axis in terms of the host star radius, a/R_{pri}, was found using b, k from Equation (3.2) and the width of primary eclipse (W).

$$\frac{a}{R_{pri}} = \frac{\sqrt{(1+k)^2 - b^2}}{\pi\, W} \tag{3.3}$$

This equation assumes a circular orbit which is not always the case for these systems but is a close enough approximation for small eccentricities, especially as an initial estimate.

The estimate for the inclination in degrees i, was calculated from b and a/R_{pri}.

$$i = \cos^{-1}\left(b\,\frac{R_{pri}}{a}\right) \tag{3.4}$$

Equation (3.4) assumes circular orbits which is acceptable for the purpose of estimating some initial starting values.

The transit and eclipse models from `BATMAN` were used to calculate model LCs that were fit to the observed TESS light curves for each of the chosen systems. The parameters that were always varied when fitting were T_0; P; k; R_{pri}/a; b; L; and the limb darkening parameters from the Claret 4-parameter law (see Equation (1.4)), a_1, a_2, a_3, a_4. Systems found in literature without significant eccentricity ($e < 0.003$) had eccentricity, e and longitude of periastron, ω set to 0 and 90°, respectively.

For systems with significant eccentricity, one of two approaches were taken when fitting. For systems with published measurements of eccentricity, e; and longitude of periastron, ω measured from a spectroscopic orbit, these values were used as free parameters with Gaussian priors set to keep our fit consistent with the published values. For systems without measurements for e and ω, the free parameters $e\cos(\omega)$ and $e\sin(\omega)$ were used instead. These were selected as they are less correlated than e and ω. This selection of $e\cos(\omega)$ and $e\sin(\omega)$ required a transformation when calculating the prior distribution to produce a non uniform prior distribution to ensure a uniform distribution for e. This is covered further in Section 1.5.2. The list of targets along with how they were treated whilst fitting is shown in Table 3.2. From here onward, the letters 'EBLM' will be omitted from star names for conciseness.

Table 3.2: List of stars analysed with note of how they were analysed. Targets marked "Circular" had no eccentricity variation in fitting. Targets marked "Eccentricity priors" had an eccentricity prior obtained from literature applied. Targets marked "No available priors" had no eccentricity priors applied and instead $e\cos(\omega)$ and $e\sin(\omega)$ were varied.

Target	Treatment	Reference
EBLM J0228+05	Circular	–
EBLM J0247−51	No available priors	–
EBLM J0400−51	Circular	–
EBLM J0432−33	Circular	–
EBLM J0440−48	Circular	–
EBLM J0500−46	Eccentricity priors	Triaud et al. (2017)
EBLM J0526−34	Eccentricity priors	Triaud et al. (2017)
EBLM J0608−59	Eccentricity priors	Triaud et al. (2017)
EBLM J0625−43	Circular	–
EBLM J0627−67	Eccentricity priors	Triaud et al. (2017)
EBLM J0709−52	Eccentricity priors	Triaud et al. (2017)
EBLM J0723+79	No available priors	–
EBLM J0829+66	No available priors	–
EBLM J0941−31	Eccentricity priors	Swayne et al. (2023)
EBLM J0955−39	Circular	–
EBLM J1626+57	No available priors	–
EBLM J1640+49	No available priors	–
EBLM J1705+55	Eccentricity priors	Gaia Collaboration (2022b)
EBLM J1850+50	No available priors	–

The parameters that `BATMAN` accepts to calculate a primary eclipse light curve are T_0; P; k; a/R_{pri}; inclination in degrees, i; e; ω; the name of the limb darkening law and the corresponding coefficients. Modelling secondary eclipses required adding the arguments f_{sec}/f_{pri} and time of secondary eclipse, $T_{0,\,sec}$.

3.1.2 Initialising Models

The `BATMAN` transit model does not account for the time delay seen for a secondary eclipse due to the finite speed of light. This is called the Rømer delay or light travel

time (LTT). When the secondary star is at the point where it will be eclipsed, it is at the furthest point in its orbit and so furthest from the Earth. This compared to the distance when the secondary star is eclipsing the primary star leads to a delay in the order of minutes. This was accounted for using Equation (3.5) (Fabrycky, 2010; Borkovits et al., 2015). These equations give values in units of seconds when using standard index units for the other values.

$$LTT = \frac{a}{\mathrm{R}_1}\frac{\sin(i)}{c}\frac{1-q}{1+q}\frac{1-e^2}{1-e\sin^2(\omega)} \tag{3.5}$$

As `BATMAN` was built with the main aim to calculate planetary transit LCs, the programme is set to compute the primary and secondary eclipses separately. Because of this, the final calculated primary and secondary LCs were combined to ensure the whole LC was fit simultaneously instead of having two potentially different sets of fit parameters.

The `BATMAN` primary eclipse model assumes that the companion emits no light. The LC produced for the primary eclipse model is normalised where the flux from the primary star is also unity. For the secondary eclipse model, the flux calculated outside of eclipse is the combination of the flux from the primary and secondary stars with the flux from the primary star set to unity. To combine these two parts of the model LCs, the flux from the primary star (= 1) in the secondary eclipse model was subtracted, leaving the flux measured from the secondary component. This was then added to the primary eclipse LC and the final LC normalised.

3.2 Fitting

The Markov chain Monte Carlo sampler (MCMC) python package `EMCEE` was used to sample the posterior probability distribution. I use this to examine the likelihood of the value of a parameter of the model being at a particular point. The chain used 100 walkers and for most systems after 4000 burn-in steps, a 1000 step chain was used to randomly sample the posterior distribution. The trail plots were visually inspected

for convergence. The chains are considered converged when there is no relationship between the mean or variance as a function of the step and all the chains are behaving this way. At this point the trail plots look like there is no structure. Corner plots were also generated using `corner.py`[2] and visually inspected for multi-modal distributions.

For the target J0432−33 I used 19000 burn-in steps due to problems caused by the chains for the impact parameter becoming bimodal. While bimodal distributions in MCMC analysis can cause problems, as the function of impact parameter here is symmetric around 0 (i.e. solutions at $b = 0.5$ are equivalent to solutions at $b = -0.5$) the absolute value of the chains can be taken to get the distribution. Bimodal solutions of the impact parameter occurred in systems with low impact parameters as the distributions would overlap. This occurred for J0432−33 and J0608−59. While J0400−51 and J1640+49 did not strictly become bimodal as the impact parameter for these systems is so low the distributions overlap so much the peaks are indistinguishable. These systems were however treated the same as their bimodal counterparts.

3.3 Best fit parameters

The best fit model parameters, i.e. the parameters where the log probability of the chain was highest, were used to generate plots. Note that for the impact parameter, the absolute value of the chain value was taken first. Finally, these best fit parameters were used to generate lines of best fit for the light curves and then residuals calculated. These plots were visually inspected to ensure the model parameters result in a good fit to the data.

Tables 3.3, 3.4 and 3.5 give a summary of the fit results for each target. These use the medians of the chains as the value and use the difference between the 15.87% and 84.13% percentiles of the sample as an estimate of the standard error on each parameter. Targets with a standard error > 0.03 on h_1' were removed from further analysis. Hence, J0500−46 and J0709−52 are excluded in the comparison to atmospheric models.

[2] `https://corner.readthedocs.io/`

Table 3.3: Light curve model parameters obtained from `EMCEE` fit of `BATMAN` to *TESS* data. Values in parentheses are the standard errors on the final two digits of the preceding value. D is the primary eclipse depth, W is the primary eclipse width, b is the impact parameter and L is the secondary eclipse depth

Target	D	W	b	L
J0228+05	0.01648(13)	0.029853(88)	0.411(18)	0.000626(26)
J0247−51	0.01894(11)	0.05183(15)	0.273(17)	0.001110(14)
J0400−51	0.02749(17)	0.06616(19)	0.058(48)	0.001713(47)
J0432−33	0.01472(18)	0.05110(17)	0.174(77)	0.000926(27)
J0440−48	0.01588(21)	0.06336(28)	0.486(23)	0.000917(32)
J0500−46	0.02184(35)	0.02276(14)	0.619(15)	0.001213(50)
J0526−34	0.02719(33)	0.03063(12)	0.241(27)	0.002138(35)
J0608−59	0.05436(33)	0.018267(45)	0.094(45)	0.004111(29)
J0625−43	0.02992(30)	0.05468(20)	0.190(32)	0.002480(36)
J0627−67	0.02847(21)	0.020286(86)	0.5832(90)	0.001506(28)
J0709−52	0.03302(72)	0.03228(21)	0.5833(80)	0.002806(83)
J0723+79	0.03895(23)	0.019164(38)	0.4054(58)	0.002506(12)
J0829+66	0.05025(80)	0.02528(18)	0.341(21)	0.003518(85)
J0941−31	0.01795(19)	0.04101(17)	0.378(31)	0.001198(32)
J0955−39	0.04599(68)	0.02664(14)	0.442(25)	0.00290(14)
J1626+57	0.02145(17)	0.02579(13)	0.206(29)	0.000877(17)
J1640+49	0.014658(62)	0.04144(31)	0.041(35)	0.000645(21)
J1705+55	0.04093(37)	0.014308(46)	0.319(17)	0.003663(42)
J1850+50	0.02524(29)	0.03012(32)	0.080(62)	0.001472(50)

Table 3.4: Limb darkening parameters obtained from `EMCEE` fit of `BATMAN` to *TESS* data. Values in parentheses are the standard errors on the final two digits of the preceding value. h_1' and h_2' are the limb darkening profile summary statistics as defined in Equation (1.6).

Target	h_1'	h_2'
J0228+05	0.9010(91)	0.130(18)
J0247−51	0.9035(32)	0.127(12)
J0400−51	0.8896(48)	0.116(19)
J0432−33	0.8818(48)	0.154(24)
J0440−48	0.927(10)	0.168(31)
J0500−46	0.877(34)	0.145(33)
J0526−34	0.8804(44)	0.186(27)
J0608−59	0.8801(22)	0.160(15)
J0625−43	0.8847(36)	0.152(24)
J0627−67	0.899(11)	0.191(17)
J0709−52	0.849(59)	0.153(42)
J0723+79	0.8723(42)	0.172(12)
J0829+66	0.8788(95)	0.161(38)
J0941−31	0.8947(92)	0.138(22)
J0955−39	0.885(24)	0.102(37)
J1626+57	0.8787(28)	0.159(16)
J1640+49	0.8876(35)	0.130(12)
J1705+55	0.8817(50)	0.168(21)
J1850+50	0.8671(56)	0.147(29)

Table 3.5: Parameters obtained from `EMCEE` fit of `BATMAN` to *TESS* data. Values in parentheses are the standard errors on the final two digits of the preceding value. Where k is the radius ratio, and J is the surface brightness ratio

Target	k	R_1/a	$\sin i$	e	J
J0228+05	0.12838(52)	0.08928(66)	0.999326(68)	–	0.0380(16)
J0247−51	0.13761(39)	0.14744(70)	0.99919(11)	0.0037(11)	0.05860(78)
J0400−51	0.16580(52)	0.17867(76)	0.99995(10)	–	0.0623(18)
J0432−33	0.12132(74)	0.1450(14)	0.99968(26)	–	0.0628(18)
J0440−48	0.12602(83)	0.1960(20)	0.99545(51)	–	0.0578(21)
J0500−46	0.1478(12)	0.07402(80)	0.998952(70)	0.22980(44)	0.0555(23)
J0526−34	0.1649(10)	0.08443(48)	0.999792(47)	0.12605(18)	0.0786(15)
J0608−59	0.23316(71)	0.04669(18)	0.9999903(87)	0.15625(30)	0.07561(62)
J0625−43	0.17298(86)	0.14841(86)	0.99960(14)	–	0.0829(13)
J0627−67	0.16873(62)	0.06292(31)	0.999326(26)	0.15868(63)	0.05289(93)
J0709−52	0.1817(20)	0.09864(91)	0.998344(67)	0.3435(13)	0.0850(29)
J0723+79	0.19736(59)	0.05344(14)	0.9997654(76)	0.0629(26)	0.06434(49)
J0829+66	0.2242(18)	0.06753(61)	0.999735(35)	0.1605(51)	0.0701(21)
J0941−31	0.13399(71)	0.1205(12)	0.99896(19)	0.19841(36)	0.0668(18)
J0955−39	0.2145(16)	0.07399(83)	0.999466(71)	–	0.0632(31)
J1626+57	0.14646(58)	0.07185(52)	0.999890(31)	0.0390(21)	0.04087(83)
J1640+49	0.12107(26)	0.11628(90)	0.999989(23)	0.0649(76)	0.0440(15)
J1705+55	0.20232(90)	0.03878(19)	0.9999235(89)	0.26455(12)	0.0895(12)
J1850+50	0.15886(93)	0.0819(10)	0.999979(36)	0.1081(80)	0.0583(21)

4 Comparing to atmospheric models

4.1 Extracting theoretical parameters

The final sample of targets from this project contains 17 targets. Combined with Maxted (2023), the final sample contained 27 targets in the *TESS* passband and 33 in the *Kepler* passband. For each of the remaining targets, the parameters $T_{\rm eff}$, $\log(g)$ and [M/H] were collected from Freckelton et al. (2023) and Fitzpatrick et al. (2024, in prep) (Freckleton, private communication). This allowed us to compare our measurements to the limb darkening parameters generated using the models in the following papers.

- ATLAS (Claret, 2017)
- MPS−ATLAS Set 1 (Kostogryz et al., 2022)
- MPS−ATLAS Set 2 (Kostogryz et al., 2022)
- PHOENIX−COND (Claret, 2018)
- Stagger-grid (Maxted, 2018)

Comparisons with the PHOENIX−COND and MPS−ATLAS Set 1 were focused on as the results from the other models are similar.

Systems below an impact parameter of 0.65 from this project and Maxted (2023) were used. The final sample contains 23 *Kepler* systems with $\langle T_{\rm eff}\rangle = 5944$K $\langle$[M/H]$\rangle = 0.135$ and $\langle\log(g)\rangle = 4.31$ and 27 *TESS* systems with $\langle T_{\rm eff}\rangle = 6136$K $\langle$[M/H]$\rangle = 0.004$ and $\langle\log(g)\rangle = 4.05$.

`SCIPY`'s `LinearNDInterpolator` was used to make a grid of theoretical limb darkening parameters for each model with a linear interpolation between points. The *TESS* and *Kepler* bands had their own grid of theoretical limb darkening parameters dependant on $T_{\rm eff}$, $\log(g)$ and [M/H] for each model.

Table 4.1: Atmospheric parameters with relevant references

Target	$T_{\rm eff}$ [K]	$\log(g)$	[M/H]	Reference
J0228+05	6912 ± 134	4.15 ± 0.14	$+0.08 \pm 0.08$	Freckelton et al. (2023)
J0247−51	6130 ± 191	3.97 ± 0.12	-0.43 ± 0.33	Fitzpatrick et al., 2024, in prep
J0400−51	6010 ± 180	3.96 ± 0.10	-0.21 ± 0.19	Fitzpatrick et al., 2024, in prep
J0432−33	6166 ± 134	3.55 ± 0.14	-0.61 ± 0.05	Freckelton et al. (2023)
J0440−48	6113 ± 286	4.08 ± 0.13	-0.31 ± 0.37	Fitzpatrick et al., 2024, in prep
J0500−46	5788 ± 116	4.22 ± 0.18	-0.15 ± 0.05	Freckelton et al. (2023)
J0526−34	6307 ± 128	3.97 ± 0.15	-0.05 ± 0.07	Freckelton et al. (2023)
J0608−59	5865 ± 103	3.69 ± 0.25	$+0.01 \pm 0.05$	Freckelton et al. (2023)
J0625−43	5678 ± 118	4.01 ± 0.12	-0.10 ± 0.16	Fitzpatrick et al., 2024, in prep
J0627−67	6498 ± 117	4.24 ± 0.27	-0.16 ± 0.13	Freckelton et al. (2023)
J0709−52	6097 ± 312	3.96 ± 0.10	-0.21 ± 0.39	Fitzpatrick et al., 2024, in prep
J0723+79	6014 ± 121	4.01 ± 0.19	-0.08 ± 0.03	Freckelton et al. (2023)
J0829+66	5635 ± 126	4.13 ± 0.15	$+0.16 \pm 0.06$	Freckelton et al. (2023)
J0941−31	6686 ± 134	3.77 ± 0.18	-0.26 ± 0.04	Freckelton et al. (2023)
J0955−39	6223 ± 165	3.90 ± 0.66	$+0.32 \pm 0.22$	Fitzpatrick et al., 2024, in prep
J1626+57	5968 ± 118	3.92 ± 0.17	$+0.04 \pm 0.04$	Freckelton et al. (2023)
J1640+49	6459 ± 127	3.76 ± 0.17	$+0.01 \pm 0.04$	Freckelton et al. (2023)
J1705+55	5706 ± 112	3.63 ± 0.19	-0.15 ± 0.06	Freckelton et al. (2023)
J1850+50	5830 ± 103	3.63 ± 0.16	$+0.24 \pm 0.04$	Freckelton et al. (2023)

The limb darkening parameters predicted by the individual model were extracted for each target using the parameters in Table 4.1 to use for comparison with observations. Targets outside the parameter range of the model limits were excluded. A Monte-Carlo simulation was performed to determine an error bar caused by the uncertainty in the input parameters. A random sample of 100 points were taken for $T_{\rm eff}$, $\log(g)$ and [M/H] respectively with a Gaussian distribution and standard deviation equal to the values and errors given in Table 4.1. The arrays were then fed into the interpolator to produce a distribution of theoretical h_1' and h_2' to calculate errors on the theoretical values for each system. The PHOENIX−COND coefficients are only available for solar metallicity so a small linear correction was applied to theoretical limb darkening parameters as per Maxted (2023). This was done using Equation (4.1) for the *TESS* systems.

$$\begin{aligned} h'_{1,cal} &= h'_{1,cal} - 0.0027 \times [\mathrm{M/H}]/0.23 \\ h'_{2,cal} &= h'_{2,cal} + 0.0035 \times [\mathrm{M/H}]/0.23 \end{aligned} \tag{4.1}$$

Once the theoretical values and errors were extracted, the observed limb darkening coefficients could be compared. The following parameters are defined for readability during comparison.

$$\begin{aligned} \Delta h'_1 &= h'_{1,obs} - h'_{1,cal} \\ \Delta h'_2 &= h'_{2,obs} - h'_{2,cal} \end{aligned} \tag{4.2}$$

Here $h'_{1,obs}$ and $h'_{2,obs}$ are the parameters h'_1 and h'_2 calculated from the light curves in the analysis described in Chapter 3 and $h'_{1,cal}$ and $h'_{2,cal}$ are the parameters predicted by a particular atmospheric model. $\Delta h'_1$ and $\Delta h'_2$ were then plotted against [M/H] and T_{eff} to determine relationships in the form of Equation (4.3) using a least squares fit. Where Y is the parameter on the y axis ($\Delta h'_1$ or $\Delta h'_2$) and X is the parameter on the x axis (($T_{\mathrm{eff}} - 6000\mathrm{K})/1000\mathrm{K}$ or [M/H])

$$Y = a_X + b_X\, X \tag{4.3}$$

Temperature relations are also drawn only from targets with $T_{\mathrm{eff}} > 5500$K. This is for continuity with Maxted (2023) and as the sample of systems $T_{\mathrm{eff}} < 5500$K was not increased and so is too sparse to with any confidence state if the relation is truly applicable below this.

4.2 Model Comparisons

4.2.1 PHOENIX−COND model

PHOENIX−COND is a 1D spherically-symmetric model. The limb darkening parameters were computed by Claret (2018) using the PHOENIX−COND model as generated by Husser et al. (2013). Henceforth, references to the "PHOENIX model" or "PHOENIX coefficients" are referring to this set calculated in Claret (2018). All systems in the initial sample were within the bounds of the PHOENIX model coefficients.

Table 4.2: Relationship from least-squares fit for a straight line (Equation (4.3)) determined for different models and bands and their respective limb darkening coefficient as a function of $(T_{\rm eff} - 6000{\rm K})/1000{\rm K}$. σ_X is the additional scatter added in quadrature to the standard error on $\Delta h'_1$ or $\Delta h'_2$ to obtain $\chi^2 = N_{df}$ (which is equal to the number of targets).
(*) Magnitude of the gradient trend is more than two times the standard error.
([1]) Limb darkening parameters compared to Claret (2018).
([2]) Limb darkening parameters compared to Kostogryz et al. (2022), Set 1.

#	Band	Model	Coefficient	$a_X \times 10^3$	$b_X \times 10^3$	σ_X
Maxted (2023)						
1	Combined	PHOENIX−COND[1]	h'_1	$+9.5 \pm 1.9$	$+15 \pm 5^*$	0.0097
2	Combined	PHOENIX−COND[1]	h'_2	$+0.8 \pm 3.1$	-15 ± 8	0.0164
This work						
3	*Kepler*	PHOENIX−COND[1]	h'_1	11.7 ± 1.8	$+19.8 \pm 4.9^*$	0.0083
4	*Kepler*	PHOENIX−COND[1]	h'_2	-2.9 ± 3.6	-18.6 ± 9.8	0.0164
5	*TESS*	PHOENIX−COND[1]	h'_1	$+15.0 \pm 3.0$	$+0.8 \pm 7.3$	0.0138
6	*TESS*	PHOENIX−COND[1]	h'_2	$+0.6 \pm 4.9$	-5.7 ± 12.0	0.0228
7	*Kepler*	MPS−ATLAS[2]	h'_1	$+5.9 \pm 1.8$	$+6.6 \pm 5.0$	0.0084
8	*Kepler*	MPS−ATLAS[2]	h'_2	-11.4 ± 3.6	-3.5 ± 9.8	0.0165
9	*TESS*	MPS−ATLAS[2]	h'_1	$+8.4 \pm 2.8$	-7.8 ± 6.8	0.0129
10	*TESS*	MPS−ATLAS[2]	h'_2	-9.6 ± 4.9	$+6.0 \pm 12.1$	0.0229

4.2.1.1 Metallicity relation

Figure 4.1 shows $\Delta h'_1$ and $\Delta h'_2$ for *TESS* systems as a function of metallicity to see if there is a relationship. The relation in Equation (4.4) was determined from the combined using a least-squares fit. The value 0.01331 was added in quadrature to the standard error on h'_1 to obtain $\chi^2 = N_{df}$ (which is equal to the number of targets). $\Delta h'_2$ does not show any significant gradient across this sample.

$$\Delta h'_1 = (0.0152 \pm 0.0025) + (-0.0119 \pm 0.0106)\,[{\rm M/H}] \tag{4.4}$$

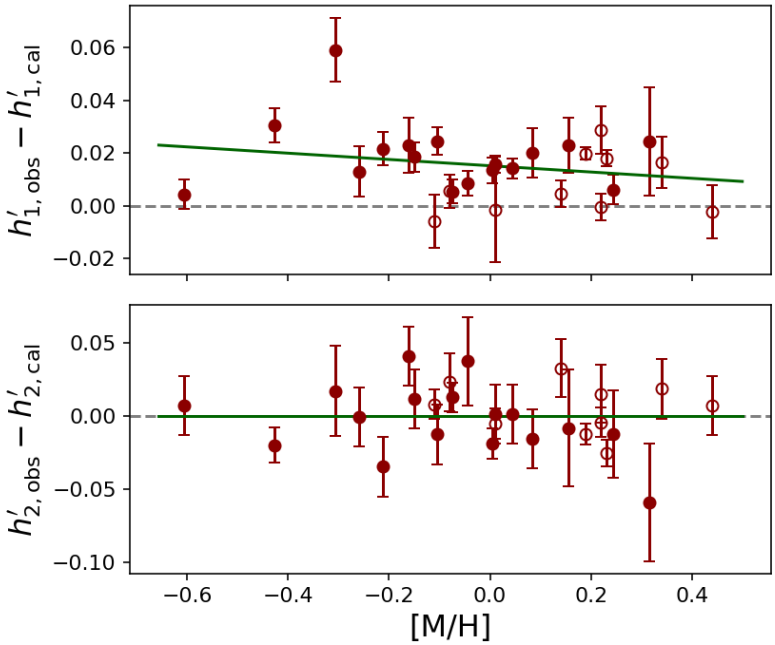

Figure 4.1: Figure showing observed limb darkening profile in the *TESS* band compared with the theoretical limb darkening profile as calculated by Claret (2018) as a function of metallicity.

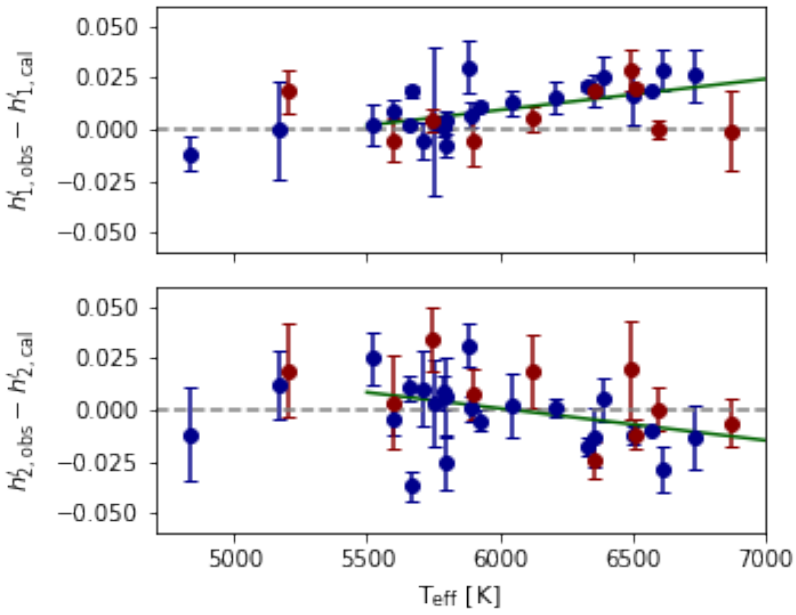

Figure 4.2: Figure 10 from Maxted (2023). Blue points are results in the *Kepler* band and red points in the *TESS* band. The green line is the line of best fit for all systems plotted above 5500K (relations given in rows 1 and 2 of Table 4.2 in the form of Equation (4.3)). Note, systems above an impact parameter of 0.65 were excluded.

4.2.1.2 Temperature relation

Figure 4.2 shows the observed limb darkening parameters determined in Maxted (2023) compared with the PHOENIX model limb darkening parameters. The figure displays 33 systems that were within the bounds of the PHOENIX model. Here a clear relation between the temperature and the offsets in $\Delta h'_1$ and $\Delta h'_2$ can be seen. The relation was determined from the combined *Kepler* and *TESS* systems and is shown in Table 4.2, rows 1 and 2.

Maxted (2023) only had a small sample of systems investigated in the *TESS* band so when extracting a relation between the observed and actual limb darkening as a function of $T_{\rm eff}$, both the *Kepler* and *TESS* data were combined. However, the results in Fig. 4.2 suggest that the *TESS* systems might not follow the same trend for $\Delta h'_1$ as the *Kepler* systems.

Figure 4.3 shows the complete combination of the accepted systems from Maxted (2023) and the accepted systems investigated in this project. From this split figure of a larger sample it becomes obvious that the *TESS* systems are not following the same trend as the *Kepler* systems hence the relationship is skewed to a lower trend than the *Kepler* sample actually shows. The relation was redetermined here separately for both samples. Rows 3 and 4 of Table 4.2 give the relation parameters for $\Delta h'_1$ and $\Delta h'_2$ for the *Kepler* systems ($\Delta h'_{1,Kepler}$ and $\Delta h'_{2,Kepler}$ respectively).

For reference, the green dotted line in Figure 4.3 gives the relation determined in Maxted (2023) making the slight suppression caused by the *TESS* systems visible. This does not change the relation significantly for $\Delta h'_{1,Kepler}$ or $\Delta h'_{2,Kepler}$ with the gradients and y-intercepts having overlapping error bars. It is however worth noting that for $\Delta h'_{1,Kepler}$, the gradient error bars only just overlap.

Rows 5 and 6 give the relation for $\Delta h'_1$ and $\Delta h'_2$ for the *TESS* systems ($\Delta h'_{1,TESS}$ and $\Delta h'_{2,TESS}$ respectively). This line of best fit was determined to justify the separation of the *TESS* and *Kepler* systems so while the relations are displayed, it can be seen that both $\Delta h'_{1,TESS}$ and $\Delta h'_{2,TESS}$ are consistent with having no gradient. The gradient relation for $\Delta h'_{2,TESS}$ does overlap errors with with the original relation from Maxted

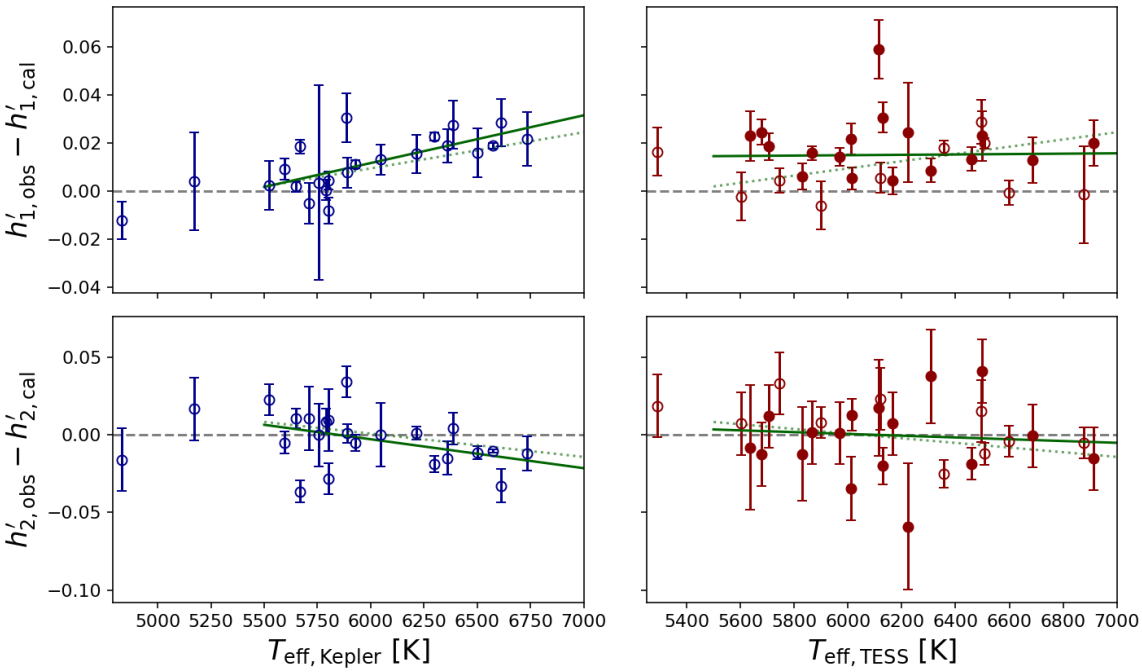

Figure 4.3: Figure showing the observed limb darkening profile compared to the parameters predicted by the PHOENIX−COND model calculated in Claret (2018). *Kepler* systems are in blue on the left panels and *TESS* systems are in red on the right panels. Data from Maxted (2023) uses unfilled circles, data from this project uses filled circles. The solid green line is the best fit for each set of systems for $T_{\mathrm{eff}} > 5500$ and the dotted green line is the relation from Maxted (2023). The grey dashed line is the zero line. Rows 3 and 4 of Table 4.2 in the form of (4.3) give the trends for the *Kepler* systems and rows 5 and 6 give the trends for *TESS*.

(2023) however the relation here is not statistically significant (not greater than three times the error from zero) unlike the one from Maxted (2023).

4.2.2 MPS−ATLAS Set 1 and Set 2

MPS−ATLAS is a 1D plane parallel model that computes atmospheric parameters for different stellar compositions and mixing lengths. Kostogryz et al. (2022) presents two grids of limb darkening profiles. "Set 1" uses the same abundances and mixing-length as Castelli & Kurucz (2003) Meanwhile "Set 2" uses the more recent Asplund et al. (2009) abundances and treats the mixing-length parameter as a function of $T_{\rm eff}$, $\log g$ and [M/H] from Viani et al. (2018). Note that they only use this functional mixing length over the range used by Viani et al. (2018), outside this range the boundary value from the relationship mixing length parameter was used. This boundary could minimally affect the errors of values in Set 2 as the Gaussian sample will overlap the edge of this boundary for some stars. This should not affect the actual values as the best value falls within the boundary of the mixing length function for all systems. Here, however, I focus on Set 1 as the results from both are extremely similar.

4.2.2.1 Metallicity relation

Figure 4.4 shows $\Delta h'_1$ and $\Delta h'_2$ for *TESS* systems as a function of metallicity to see if there are any trends. All 27 *TESS* systems were within the bounds of the model coefficients. Fitting a line to the data gives a gradient encompassing zero so on the whole the data has no significant trend, just a small average offset.

4.2.2.2 Temperature relation

Figure 4.5 shows $\Delta h'_1$ and $\Delta h'_2$ as a function of $T_{\rm eff}$ for systems in the *Kepler* band (left hand side panels) and the *TESS* band (right hand side panels). Rows 7 and 8 of Table 4.2 give the relation and additional scatter for $\Delta h'_1$ and $\Delta h'_2$ for the *Kepler* systems

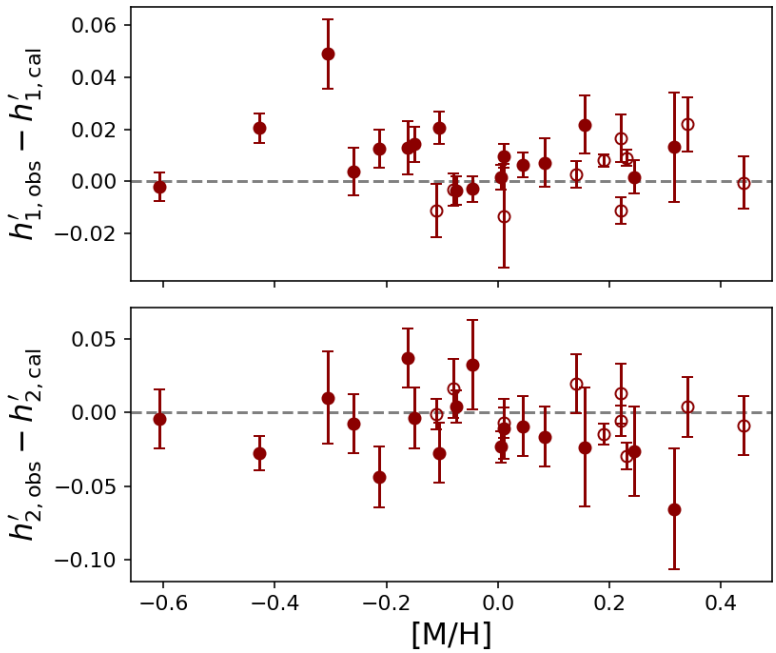

Figure 4.4: Figure showing observed limb darkening profile in the *TESS* band compared with the theoretical limb darkening profile as calculated by Kostogryz et al. (2022) (Set 1) as a function of metallicity.

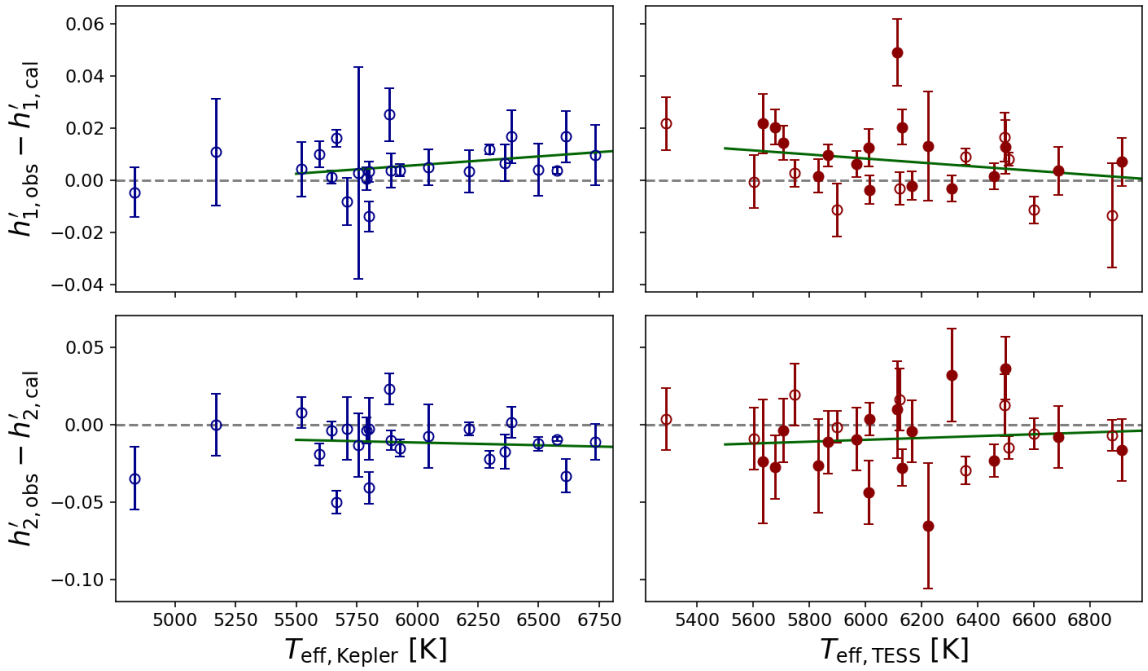

Figure 4.5: Figure showing observed limb darkening profile compared with the theoretical limb darkening profile as calculated by Kostogryz et al. (2022) (Set 1) as a function of T_{eff}. *Kepler* systems are in blue on the left panels and *TESS* systems are in red on the right panels. Data from Maxted (2023) uses unfilled circles, data from this project uses filled circles. The solid green line is the best fit for each set of systems for $T_{\mathrm{eff}} > 5500\,\mathrm{K}$. The grey dashed line is the zero line. Rows 7 and 8 of Table 4.2 in the form of (4.3) give the trends for the *Kepler* systems and rows 9 and 10 give the trends for *TESS*.

($\Delta h'_{1,Kepler}$ and $\Delta h'_{2,Kepler}$ respectively). $\Delta h'_{2,Kepler}$ gives a gradient consistent with zero however, $\Delta h'_{1,Kepler}$ shows a very small (but statistically insignificant) gradient. The *TESS* systems tell a very similar story but are provided for reference. Row 9 of Table 4.2 gives the relation and additional scatter for $\Delta h'_{1,TESS}$ and row 10 for $\Delta h'_{2,TESS}$.

4.3 Discussion

From the initial sample of confirmed EBLM systems from BEBOP and the EBLM project, 17 of these systems with the most precisely determined limb darkening parameters were combined with the sample of transiting hot Jupiters from Maxted (2023). These 50 targets were used to compare with limb darkening coefficients from the PHOENIX−COND and MPS−ATLAS atmospheric models and determine any trends. The sample of metallicities were extended as well as number of targets in the *TESS* band. This allowed the *Kepler* and *TESS* systems to now be analysed separately and I found that they often showed different trends.

For the PHOENIX−COND model, the *TESS* systems showed no significant trend with temperature or metallicity for h'_1 or h'_2, only a small offset. The *Kepler* systems however showed a significant trend for h'_1 with effective temperature. Even though the *Kepler* and *TESS* wavelength bands largely overlap, they do operate over different ranges, these can be seen in Figure 4.3. Areas of spectra where there are many spectral features overlapping is called "line blanketing". From Figure 4.3 we can also see example spectra for a G dwarf star, much like those seen as the primary star in EBLMs, there is a large section around 400 to 600 nm that contains one of these areas of line blanketing. Only the *Kepler* band is sensitive to much of this area of the spectra so I suggest that an insufficient characterisation of this area of the spectrum for similar stars as a potential cause for the trend seen in the *Kepler* band for these systems.

For the MPS−ATLAS model no significant trends for h'_1 or h'_2 with metallicity or temperature were found for *Kepler* or *TESS* systems, only an offset. Kostogryz et al. (2022) suggest that the cause of this offset is not accounting for magnetic activity,

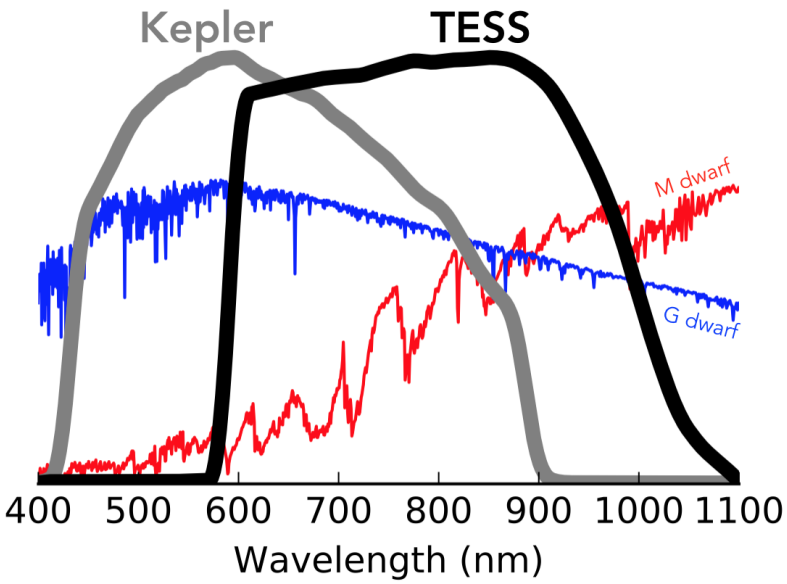

Figure 4.6: Image credit: Zach Berta Thompson[1] using data from Sullivan et al. (2015). Figure shows a schematic of typical spectra of a G dwarf star and M dwarf star in blue and red respectively compared to the *Kepler* and *TESS* bandpass response curves.

hence, for this discussion it is worth mentioning WASP−18. WASP−18 is a star with a transiting $10\,M_{Jup}$ hot Jupiter with a period of 0.94 days, hence, this planet orbits very close to its host star. This star exhibits a remarkably low level of magnetic activity, it is suggested that this is caused by this close orbiting massive planet (Lanza, 2014; Fossati et al., 2018). This has made it an interesting system to see if the current discrepancies between models and observed parameters is caused by magnetic activity as was investigated in Maxted (2023). WASP−18 has a temperature of $6599 \pm 48\,K$ and from Figures 4.3 and 4.5 we observe that the model predictions align very well with observations. For the PHOENIX−COND model, the errors of $\Delta h'_1$ and $\Delta h'_2$ both encompass the zero line and for the MPS−ATLAS model $\Delta h'_2$ encompasses zero and $\Delta h'_1$ is within 2.5 standard deviations of the zero line. So both these models in the *TESS* band are doing well at describing what we observe for the low magnetic activity

[1] https://heasarc.gsfc.nasa.gov/docs/tess/the-tess-space-telescope.html

cases. This means however that we will be able to measure magnetic activity from limb darkening as is currently being worked on in literature (Kostogryz et al., 2022, 2023; Maxted et al., 2023).

5 Investigations into the radius inflation problem

The radii predicted by stellar models for cool stars are often too small compared those computed from observations. This discrepancy is dubbed the radius inflation problem. I calculate gravities, temperatures, masses and radii for the M dwarf companion in EBLM systems to investigate whether the stars in this sample show evidence of the radius inflation problem when comparing to the set of MIST models (Dotter, 2016; Choi et al., 2016).

5.1 Methods

5.1.1 Light curve fitting

The light curves for each target were re-analysed, instead fitting using the power-2 law. This was done to obtain the best possible precision on the radius compared to what can be done with much looser constraints on the limb darkening from the highly correlated limb darkening parameters of the Claret law. Specifically the power-2 law is chosen as it is found to outperform other 2 parameter laws especially for cooler stars (Morello et al., 2017) such as the hosts in our sample. Here we care more about the limb darkening being precisely defined as opposed to complete accuracy as limb darkening is no longer the focus.

Other than this different limb darkening law, the light curve analysis was the same as in Section 3. Parameters from this were used to determine the parameters M_1, M_2, R_1, R_2, ρ_1, $\log g_2$ and $\mathrm{T_{eff,2}}$.

5.1.2 Model isochrones

The stellar isochrones used for reference in this analysis are the MIST isochrones and read in using the python package `READ_MIST_MODELS`[1]. The ages 1, 4 and 10 Gyr are used and over this analysis and I use metallicities in the range -1.5 and $+0.5$. These ages are chosen from looking at the Kepler LEGACY sample of solar-like main sequence stars (Silva Aguirre et al., 2017) and these metallicities were chosen by looking at the range of metallicities of our targets. Isochrones for M, $\log(T_{\rm eff})$ and $\log(L)$ are read in and transformed as follows.

We can use the Stefan-Boltzmann law in the form of Equation (5.1) to gain the radius R by rearranging. Where L is the luminosity and $\sigma_{\rm SB}$ is the Stefan-Boltzmann constant.

$$L = 4\pi\sigma_{\rm SB}\, R^2\, {T_{\rm eff}}^4 \tag{5.1}$$

The average stellar density was calculated using $\log(\rho) = \log(M) - 3\log(R)$ with M and R in solar units. The surface gravity is given by Equation (5.2).

$$g = \frac{GM}{R^2} \tag{5.2}$$

5.1.3 Determining primary star mass, radius and average density and secondary star mass, radius and gravity

From the fits described in Sections 3 and 5.1.1, the parameters: k, R_1/a, e, J, $\sin i$ and their relevant errors and P were collected along with $T_{\rm eff}$, $\log(g)$ and [M/H] and their errors as in Table 4.1; K_1 from Triaud et al. (2017) or the Gaia Collaboration (2022b), and an initial mass estimate, M_1, from Triaud et al. (2017) where available. Where no initial mass was found in literature, the value 1.2 $M_\odot$ was taken as this is around the average mass of the primary star in EBLM systems. An initial estimate of the radius of the primary star was calculated from Equation (5.2) using the primary star's mass and gravity.

[1] `https://github.com/jieunchoi/MIST_codes/blob/master/scripts/read_mist_models.py`

The `PYCHEOPS` Mote Carlo simulation function, `massradius` was used to gain a test sample of stellar densities for the primary star for 100,000 simulations. A Gaussian sample of random numbers are generated for k, a/R_1, e, K and $\sin i$ with standard deviations equal to the quoted standard errors. The error on the orbital period is very small and so was assumed to negligible. To get a sample of test primary densities, the secondary mass was calculated across the sample of parameters. The mass function, $f(m)$, is calculated from the observables on the left hand side of the Equation (5.3) and by rearranging, a cubic polynomial can be solved to determine M_2.

$$f(m) = \frac{P(1-e^2)^{3/2}}{2\pi G} K_1^3 = \frac{{M_2}^3 \sin^3 i}{(M_1 + M_2)^2} \tag{5.3}$$

From this, the mass ratio could be calculated by dividing by M_1 and for each set of parameters, the test values of ρ_1 were calculated using Equation (5.4) in solar units.

$$\rho_1 = \frac{\rho_\odot}{(1+q)P^2} \frac{R_1}{a} \tag{5.4}$$

I used the relation from Enoch et al. (2010) to gain M_1 from ρ_1, $T_{\rm eff}$ and [M/H] as shown in Equation (5.5) where $X = \log(T_{\rm eff}) - 4.1$. Then to this test sample of $\log(M_1)$ I added scatter by adding a random number between 0 and 0.023 to each of the test masses to account for the observed scatter around the relation determined by Enoch et al. (2010) for primary star mass as a function of its density, effective temperature and metallicity.

$$\begin{aligned} \log M = \; & 0.458 + 1.430X + 0.329X^2 \\ & -0.042\log(\rho) + 0.067\log(\rho)^2 + 0.010\log(\rho)^3 + 0.044[\mathrm{M/H}] \end{aligned} \tag{5.5}$$

From this a test sample of R_1 were calculated from the test densities from the `massradius` function and the test masses above using $R = (M/\rho)^{1/3}$. These primary star test masses and radii were then passed back through the `massradius` function along with the previous P, k, a/R_1, e, K and $\sin i$ to ensure the sample of determined parameters remain consistent with the fit parameters. From the Monte Carlo simulation, the mean and standard error of M_1, R_1, ρ_1, M_2, R_2 and $\log(g_2)$ were extracted.

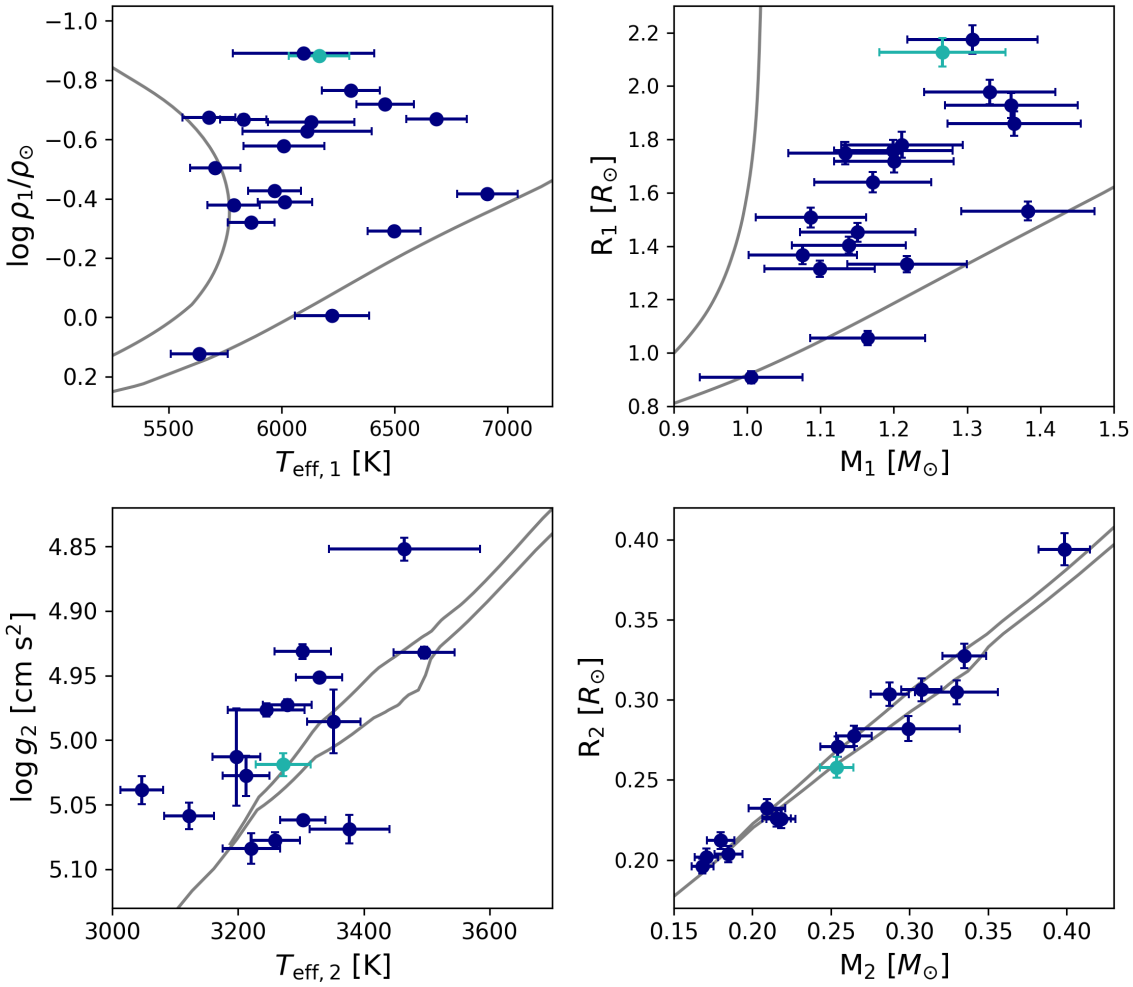

Figure 5.1: Figure showing parameters determined for the primary and secondary stars, plotted with isochrones for comparison. Dark blue points with error bars are EBLMs analysed using synthetic photometry assuming solar alpha element abundance ([α/Fe] = 0.0). The turquoise points and error bars show target J0432−33 which has α-element abundance [α/Fe] = +0.24. The grey lines are MIST isochrones (Dotter, 2016; Choi et al., 2016) plotted for ages 10Gyr and 1Gyr at solar metallicity. The top panels give parameters for the primary star and the bottom panels for the secondary star.

The sample of M_2 and R_2 from this are saved as well as the sample of metallicities for use in Section 5.1.5.

Figure 5.1 gives plots showing the results for M_1, R_1, ρ_1, M_2, R_2 and $\log(g_2)$ as well as with $T_{\rm eff,1}$ from Freckelton et al. (2023) and $T_{\rm eff,2}$ found in Section 5.1.4 below.

5.1.4 Determining secondary star temperature

To find $T_{\rm eff,2}$ I used synthetic photometry from the BT-NextGen (AGSS2009) model grid accessed through the Spanish Virtual Observatory (SVO). This model assumes solar abundances as computed by Asplund et al. (2009) and use the vapour line list from Barber et al. (2006). The models are further described in Allard et al., (2012; 2011). This model was chosen because of the range of effective temperatures, metallicities and gravities available with some flexibility in α-element abundances, [α/Fe]. Note [α/Fe] is measured relative to the solar abundance.

The `LinearNDInterpolator` function was used to make two separate grids of values from the synthetic photometry to output the surface brightness as a function of a star's effective temperature, metallicity, α-element abundance and the gravity. The resulting grids cover the following parameter ranges.

- $T_{\rm eff}$: grid 1: 2600 to 5000K, grid 2: 5000 to 8100K
- [M/H]: -1.0 to $+0.5$
- $\log(g)$: 3.0 to 5.5
- [α/Fe]: -0.2 to $+0.6$

As many of our systems did not have literature values for [α/Fe], this variable was cycled over the range above (in increments of 0.2). With the list of α-element abundances available, $T_{\rm eff,1}$, [M/H] and $\log(g_1)$ from Table 4.1 were used to extract primary star surface brightnesses (SB_1 for associated α-element abundances). This used the higher temperature range grid of synthetic photometry.

To obtain an error on the surface brightness, the value of $T_{\rm eff,1}$ had the error bar added (or subtracted depending on if the error put the temperature outside of the

grid range). The surface brightness was evaluated with [M/H] and $\log(g_1)$ kept at their best values and the surface brightness extracted from all parameters at their best value subtracted. This gave an idea of the error contributed by the uncertainty on $T_{\rm eff,1}$. This was repeated for [M/H] and $\log(g_1)$ and then all three of these uncertainties added in quadrature to give $\Delta \mathrm{SB}_1$.

The surface brightness ratio J was multiplied by SB_1 to get the surface brightness of the secondary star and the fractional error on J and SB_1 added in quadrature to give $\mathrm{SB}_2 \pm \Delta \mathrm{SB}_2$. These surface brightnesses were then converted into temperatures using the cooler grid of synthetic photometry. The `SCIPY` root finding function, `brentq`, was used to find $T_{\rm eff,2}$ and the same method as for $\Delta \mathrm{SB}_1$ was used to find the error on $T_{\rm eff,2}$ except with this added step of interpolating over temperature to find the temperature at that point of the grid.

Due to grid restraints, errors for $T_{\rm eff,2}$ could not be found for targets J0247−51, J0440−48 and J0941−51 so their points are omitted for the secondary star parameters. This means they are completely omitted from the bottom panels of Figure 5.1 even though M_2 and R_2 were found. For the most part, systems are plotted for $T_{\rm eff,2}$ determined using synthetic photometry at $[\alpha/\mathrm{Fe}] = 0$ unless a target had a particularly high α-element abundance. This was true of J0432−33, shown in turquoise. Freckelton et al. (2023) gives this target's α-element abundance to be +0.24 as well as Steinmetz et al. (2020) finding it to be $+0.24 \pm 0.19$.

After generating Figure 5.1, it was noticed that the most apparent feature is the large amount of scatter on the bottom left panel showing $T_{\rm eff,2}$ vs $\log(g_2)$. To test whether metallicity could be causing this, I have re-plotted $T_{\rm eff,2}$ vs $\log(g_2)$ with isochrones of different metallicity in Figure 5.2. It seems that metallicity could be a contributing factor to the scatter shown in Figure 5.2, however, the scatter predicted by the MIST models is greater than the scatter seen. Further investigation into the cause of this scatter was beyond the scope of this project.

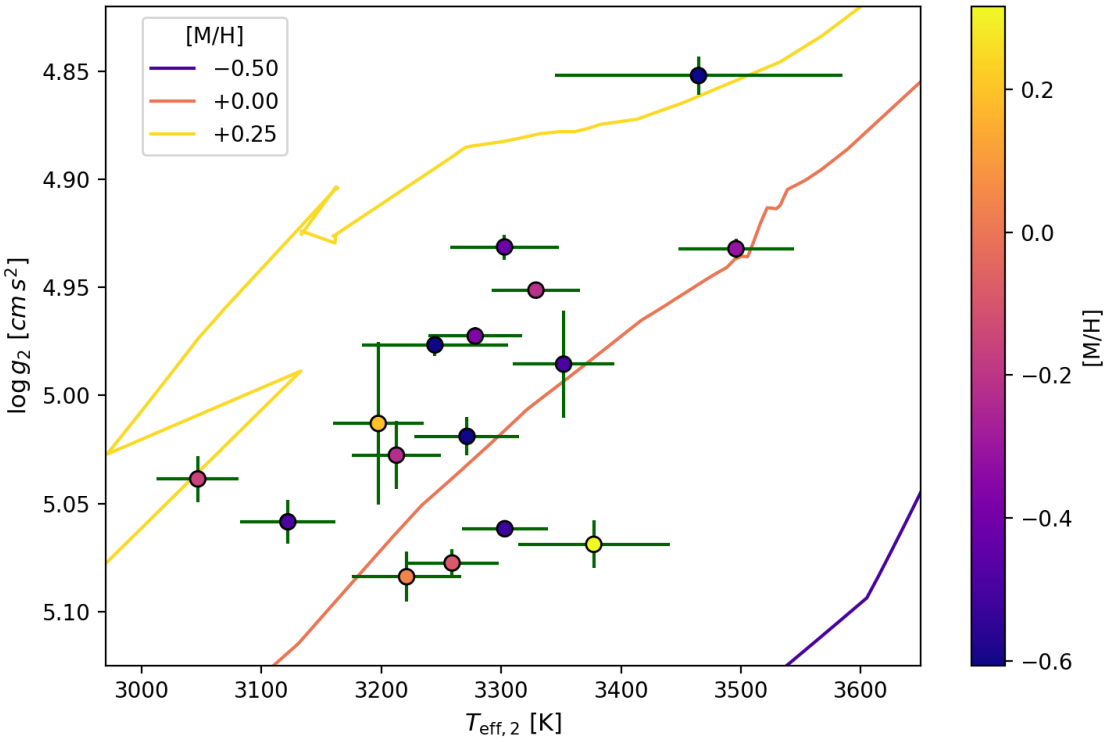

Figure 5.2: $T_{\mathrm{eff},2}$ vs $\log(g_2)$ and errors plotted for 16 EBLMs from the analysis with their colour corresponding to their metallicity (colour bar shown to the left hand side). MIST isochrones at 4 Gyr, plotted for metallicity −0.5 (purple), +0.0 (orange) and +0.25 (yellow), corresponding to the same colour mapping as the points plotted. See Section 5.1.5 for brief description of isochrone +0.25.

Table 5.1: Data behind Figures 5.1, 5.2 and 5.3. Numbers in brackets give errors on the lattermost digits.

Target	$\log(\rho_1/\rho_\odot)$	$\log(g_2)$	$T_{\rm eff,2}$	M_1	R_1	M_2	R_2
J0228+05	−0.417(9)	5.078(6)	3259(39)	1.38(9)	1.53(4)	0.168(7)	0.196(5)
J0247−51	−0.658(6)	–	–	1.20(8)	1.76(4)	0.224(9)	0.241(6)
J0400−51	−0.579(6)	4.977(5)	3245(61)	1.17(8)	1.64(4)	0.254(11)	0.271(6)
J0432−33	−0.882(13)	5.019(9)	3271(44)	1.27(9)	2.13(5)	0.254(11)	0.258(7)
J0440−48	−0.628(11)	–	–	1.20(8)	1.72(4)	0.182(8)	0.218(5)
J0500−46	−0.379(14)	5.059(10)	3122(40)	1.08(7)	1.37(4)	0.171(7)	0.202(5)
J0526−34	−0.765(7)	4.932(5)	3496(48)	1.33(9)	1.98(5)	0.335(14)	0.327(8)
J0608−59	−0.320(4)	4.951(2)	3329(37)	1.10(8)	1.31(3)	0.307(13)	0.306(7)
J0625−43	−0.674(7)	4.931(6)	3303(45)	1.13(8)	1.75(4)	0.287(12)	0.304(7)
J0627−67	−0.292(4)	5.062(3)	3303(36)	1.22(8)	1.33(3)	0.216(9)	0.226(5)
J0709−52	−0.890(11)	4.852(9)	3465(120)	1.31(9)	2.17(5)	0.398(16)	0.394(10)
J0723+79	−0.388(3)	4.973(4)	3278(39)	1.14(8)	1.40(3)	0.265(11)	0.278(6)
J0829+66	0.123(12)	5.084(12)	3221(46)	1.01(7)	0.91(2)	0.185(9)	0.204(5)
J0941−31	−0.670(13)	–	–	1.36(9)	1.86(5)	0.24(1)	0.249(6)
J0955−39	−0.005(14)	5.069(11)	3377(63)	1.16(8)	1.05(3)	0.218(9)	0.226(6)
J1626+57	−0.426(9)	5.039(11)	3047(34)	1.15(8)	1.45(3)	0.180(9)	0.212(5)
J1640+49	−0.719(10)	5.028(16)	3213(37)	1.36(9)	1.93(5)	0.209(12)	0.232(6)
J1705+55	−0.5033(99)	4.985(25)	3352(42)	1.09(8)	1.51(4)	0.33(3)	0.305(8)
J1850+50	−0.668(17)	5.013(38)	3197(38)	1.21(8)	1.78(5)	0.30(3)	0.282(8)

5.1.5 Quantifying radius inflation in the sample

We needed a way to extract model parameters to compare to to see if our observations showed evidence of radius inflation. A grid of masses and metallicities were made to extract expected radii. MIST model isochrones in metallicities −1.5, −1.0, −0.5, +0.0 and +0.5 were extracted for an age of 4 Gyr (as this is about halfway between the ages previously plotted). The isochrone for metallicity +0.25 can be seen in Figure 5.2 for age 4 Gyr to not follow similar trends to the surrounding model, investigating the reasons for this was beyond the scope of this project. Because of this, the +0.25 model was omitted from the interpolation to avoid potential extra scatter due to this

unexplained feature. The MIST interpolator[2] was used to interpolate these isochrones. The `SCIPY polyfit` function was used to extrapolate up to metallicity +1.0 in order to calculate errors on extracted parameters for some systems. For this I used MIST outputs with metallicity +0.0 and +0.5 and then this array of masses and radii at metallicity +1.0. The `LinearNDInterpolator` was used to put all these values into a grid allowing for linear interpolation between the points.

The samples of M_2, R_2 and [M/H] from Section 5.1.3 were used to investigate the offset between our observed radii and those predicted by the MIST models. Across the sample, the test masses and metallicities were passed through the grid to find a sample of MIST radii. The radius inflation was calculated for each target using Equation (5.6) where, $R_{2,\mathrm{obs}}$ is the observed radius and R_{MIST} is the MIST model radius.

$$R_{\%} = \frac{R_{2,\mathrm{obs}} - R_{2,\mathrm{MIST}}}{R_{2,\mathrm{MIST}}} \times 100 \tag{5.6}$$

This was run through for each of the test radii, then the mean and standard deviation of the sample of offsets calculated. These percentage offsets are plotted against observed M_2 in Figure 5.3. A metallicity colour bar was included to also check for a metallicity trend across the sample.

The `PYCHEOPS combine` function was then used to sample the mean offset of the sample and variance, helping us describe the radius inflation. As described in Maxted et al. (2022), the `combine` function uses `EMCEE` and samples the posterior probability using the function in Equation (5.7) where y_i is the series of radius inflations and ${s_i}^2 = {\sigma_y}^2 + {\sigma_{ext}}^2$. Here σ_y is the series of radius inflation errors and σ_{ext} is the additional standard deviation in the radius values due to unknown factors.

$$\ln \mathcal{L} = -\frac{1}{2} \sum_{i=1}^{n} \left(\frac{(y_i - \mu)^2}{{s_i}^2} + \ln ({s_i}^2) \right) \tag{5.7}$$

The mean μ and $\ln \sigma_{ext}$ were sampled assuming broad uniform priors. The function was run with 128 walkers for 3000 steps, discarding the first 2000 Taking the

[2] `https://waps.cfa.harvard.edu/MIST/interp_isos.html`

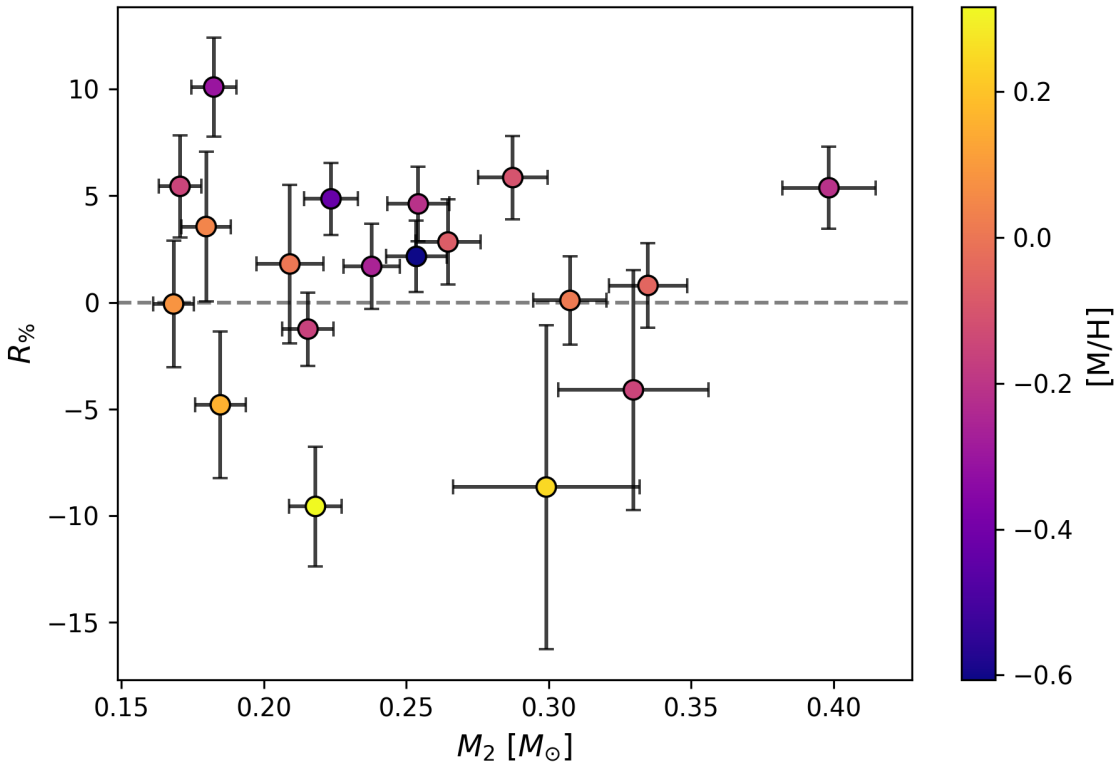

Figure 5.3: Plot of the radius inflation ($R_{\%}$) vs mass (M_2) for the secondary star in the full sample of 19 EBLMs. Points are plotted with colour mapping correlated to metallicity.

mean and standard deviation of the μ chain, the mean $R_{\%}$ was found to be $1.9 \pm 1.0\%$. The 95^{th} percentile of the sample gives a radius inflation of 3.6%. From this we can conclude that the radius inflation across our sample is minimal, hence our observations align quite well with the MIST set of models. It should be noted that excluding the higher metallicity points, would increase the radius inflation seen across our sample.

5.1.6 Population assignment

Due the enhanced α-element abundance of J0432−33 in comparison to the rest of the stars in the sample, it was interesting to find out whether our targets were members of the thin or thick disk. It is established that stars within the thick disk of the Milky Way tend to have a higher α-element abundance than those in the thin disk (Bensby et al., 2003, 2005).

`STEPARKIN`[3] (Montes et al., 2001; Cortés-Contreras et al., 2020) uses the Galactic space-velocity components to assign stars to parts of the Milky Way. For my targets and those from Maxted (2023) I took equatorial coordinates, proper motions and parallaxes with errors (Gaia Collaboration, 2020) and radial velocities (Díaz et al., 2013; Gaia Collaboration, 2018; Soubiran et al., 2018; Steinmetz et al., 2020; Jönsson et al., 2020; Buder et al., 2021; Su et al., 2022; Gaia Collaboration, 2022a). `STEPARKIN` then uses the method outlined in Johnson & Soderblom (1987) to calculate U, V and W in km s^{-1} and assign stars to various groups according to the criteria given in Bensby et al. (2003, 2005).

Stars are either flagged as thin disk, thick disk, intermediate between the thin and thick disk or in the galactic halo. From the input stars, only Kepler−489 from the Maxted (2023) sample is assigned between the thin and thick disks, we find the rest are assigned to the thin disk.

[3] `https://github.com/dmontesg/SteParKin/tree/main`

5.2 Discussion

In this section of the project I found that the effect of radius inflation seen in this sample of stars is very minimal. The 95^{th} percentile of targets show a radius inflation of only around 3%. This aligns well with current literature around the analysis of M dwarf secondary stars in EBLM systems. This can be seen in Figure 7 of Maxted et al. (2023) with masses, radii and temperatures falling well along the MIST isochrones.

From Figures 5.1 and 5.2 we observe scatter around the isochrones for the companion parameters, especially for the $\log(g_2)$ vs $T_{\rm eff,2}$ graph. This was investigated further by obtaining isochrones for metallicity -0.5 and $+0.25$. The isochrones for $\log(g_2)$ and $T_{\rm eff,2}$ are seen to be quite sensitive to metallicity, leading to the conclusion that this scatter is likely being caused by variations in metallicity. Visually inspecting Figure 5.3 one can start to see a trend where lower metallicity targets (shown in blue to purple) tend to show a higher radius inflation in comparison to solar and higher metallicity targets (shown in orange to yellow). So, even when using models that take into account for the M dwarf's metallicity, we still see a small average radius inflation, agreeing with findings in Swayne et al. (2023). Further investigation into the full affect of metallicity on the sample was beyond the scope of this project.

We currently find that our samples of transiting hot Jupiters and EBLMs likely originate from the thin disk in the Milky Way limiting the populations of M dwarfs we are able to investigate.

6 Conclusions

In this project I investigated how well atmospheric models predict limb darkening and determined if our target secondary components showed evidence of the radius inflation problem. From an initial list of known EBLMs, I characterised a total of 19 EBLM systems with well-defined secondary eclipses.

6.1 Stellar atmospheric models

Inaccurate models of stellar atmospheres lead to inaccurate estimations of stellar parameters so it is important to test how accurately current models are predicting the properties of stars. An important factor to consider that has been tested in this project is the variation of specific intensity from the centre to the limb of the star.

As part of this analysis I took measurements of limb darkening, radius ratio, scaled primary radius, inclination, surface brightness ratio, eccentricity, primary and secondary eclipse depth, primary eclipse width and impact parameter. This was done by fitting the `BATMAN` transit model to the light curves of the final sample of EBLMs and using the Claret 4-parameter limb darkening law. Effective temperatures, gravities and metallicities were then collected to enable comparison with various stellar atmosphere models. 17 targets from this project and systems from Maxted (2023) were combined to extract relations between h'_1, h'_2 and $T_{\rm eff}$, [M/H] from a sample of 23 *Kepler* systems and 27 *TESS* systems. It was determined that for *TESS* systems, both the MPS−ATLAS model limb darkening parameters calculated in Kostogryz et al. (2022) and PHOENIX−COND model parameters calculated in Claret (2018) show no significant trends with temperature or metallicity, only an offset likely caused by magnetic activity. The MPS−ATLAS model limb darkening parameters for the *Kepler* systems also only show a small offset. On the other hand, h'_1 determined from the PHOENIX−COND model shows a significant trend with $T_{\rm eff}$ and h'_2 as a function of $T_{\rm eff}$ shows a more significant trend than was found in Maxted (2023) from the com-

bined *Kepler* and *TESS* sample. The trend with h_2' however is only approximately 1.9 standard deviations from showing no trend, so much less significant than the 4σ of h_1'. However, it should be noted that h_2' is dependant on h_1'.

We suggest insufficiently defined spectral lines in the *Kepler* band due to line blanketing as a potential cause of this trend in limb darkening parameter predictions but further investigation is needed to determine if this is the case. The trends determined in this project can be used to help constrain limb darkening parameters fits for similar stars and will hopefully contribute to the continued improvement of atmospheric models.

6.2 Radius inflation

The radius ratio, scaled primary radius, surface brightness ratio, eccentricity, and orbital period of the EBLM's were used to extract primary and secondary radii and masses and secondary star temperatures and gravities. The gravities were calculated directly from orbital parameters so were not reliant on models. Calculations of $T_{\rm eff,2}$ were reliant only on a set of synthetic photometry to give a relation between the surface brightness observed in the *TESS* band and $T_{\rm eff}$. M_2 and R_2 were much more reliant on determined empirical relations.

Masses and radii were found for all stars in the sample however $T_{\rm eff,2}$ was not found for 3 systems due to constraints of the synthetic spectra. Across the sample, the average radius inflation was found to be $1.9 \pm 1.0\%$ when comparing to MIST models at an assumed age of 4 Gyr at the same metallicity as the primary star. Systems within the 95^{th} percentile show less than 3% radius inflation. This means I have not found a very significant discrepancy between models and observations which agrees with new literature saying that radius inflation is a much smaller effect than previously believed.

A Light curve fits

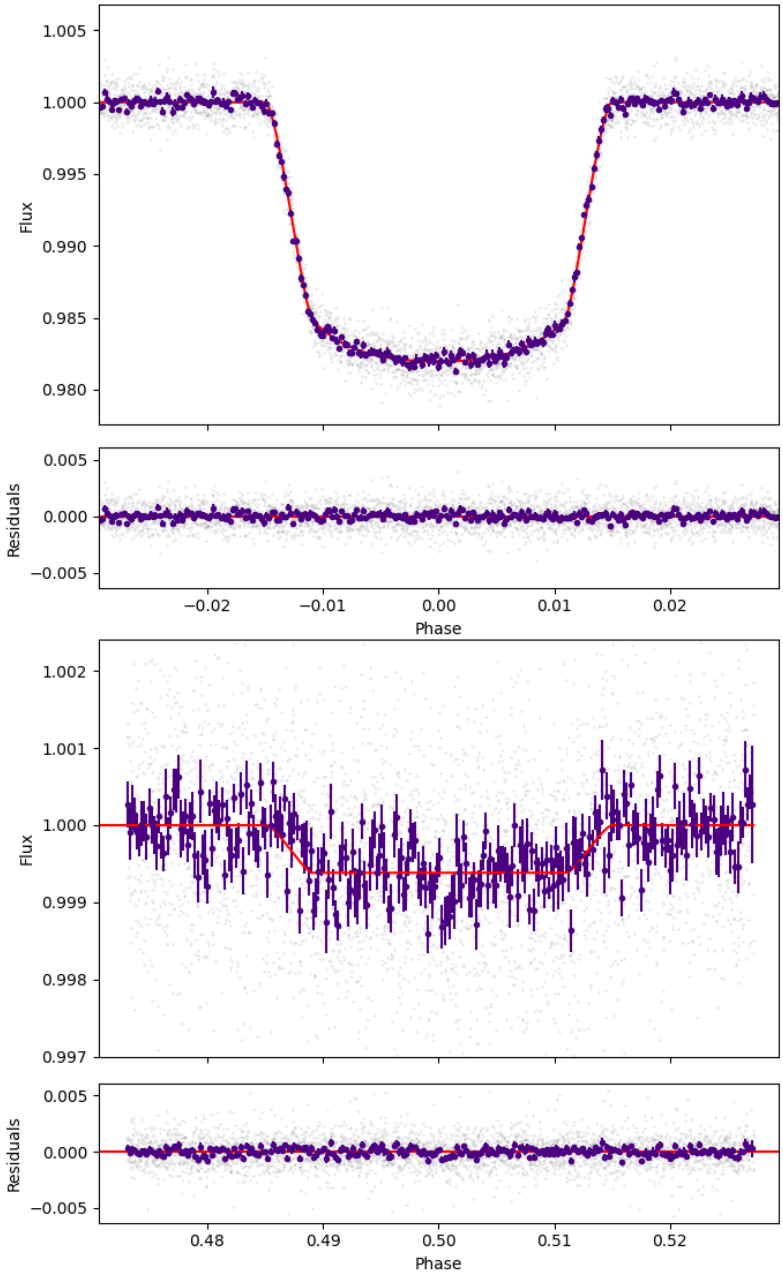

Figure A.1: *TESS* light curves (grey points) for J0228+05 with best fit of `BATMAN` from my analysis in Section 3 (red line) from `EMCEE` analysis. Data binned in 120 s intervals with errors equivalent to the mean absolute deviation are shown for reference in purple. Top panel: primary eclipse. Bottom panel: secondary eclipse.

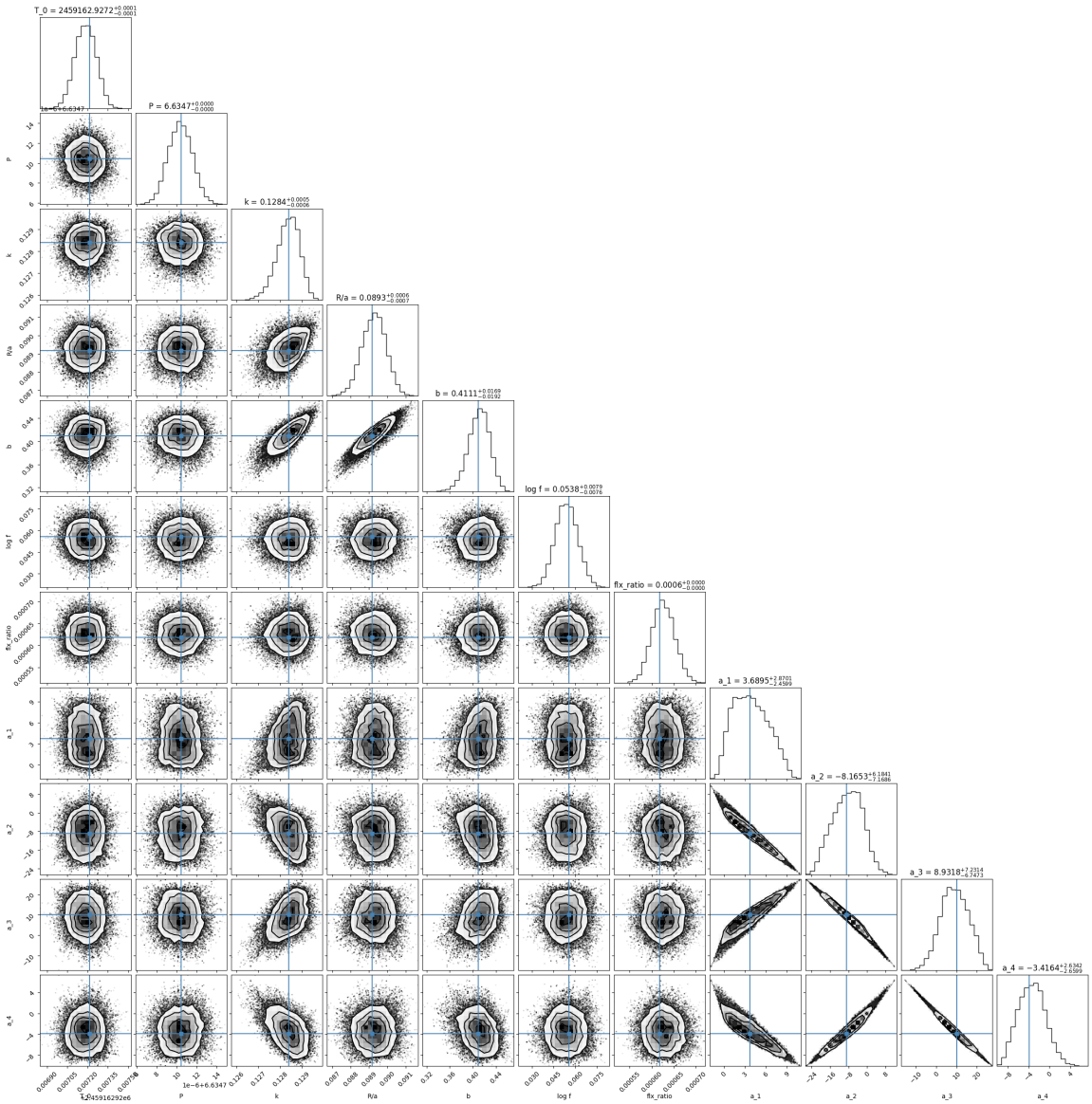

Figure A.2: Corner plots from best fits of `BATMAN` to *TESS* data using `EMCEE` from my analysis in Section 3 for J0228+05.

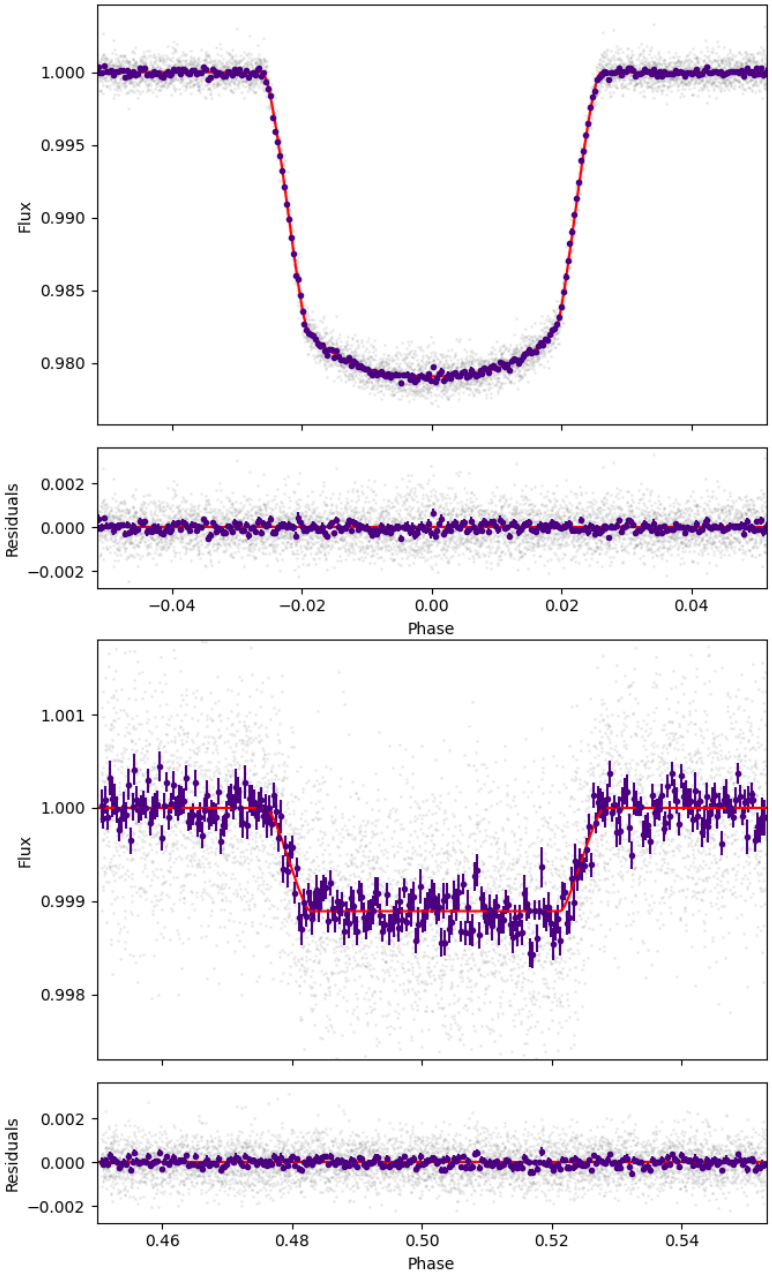

Figure A.3: *TESS* light curves (grey points) for J0247−51 with best fit of `BATMAN` from my analysis in Section 3 (red line) from `EMCEE` analysis. Data binned in 120 s intervals with errors equivalent to the mean absolute deviation are shown for reference in purple. Top panel: primary eclipse. Bottom panel: secondary eclipse.

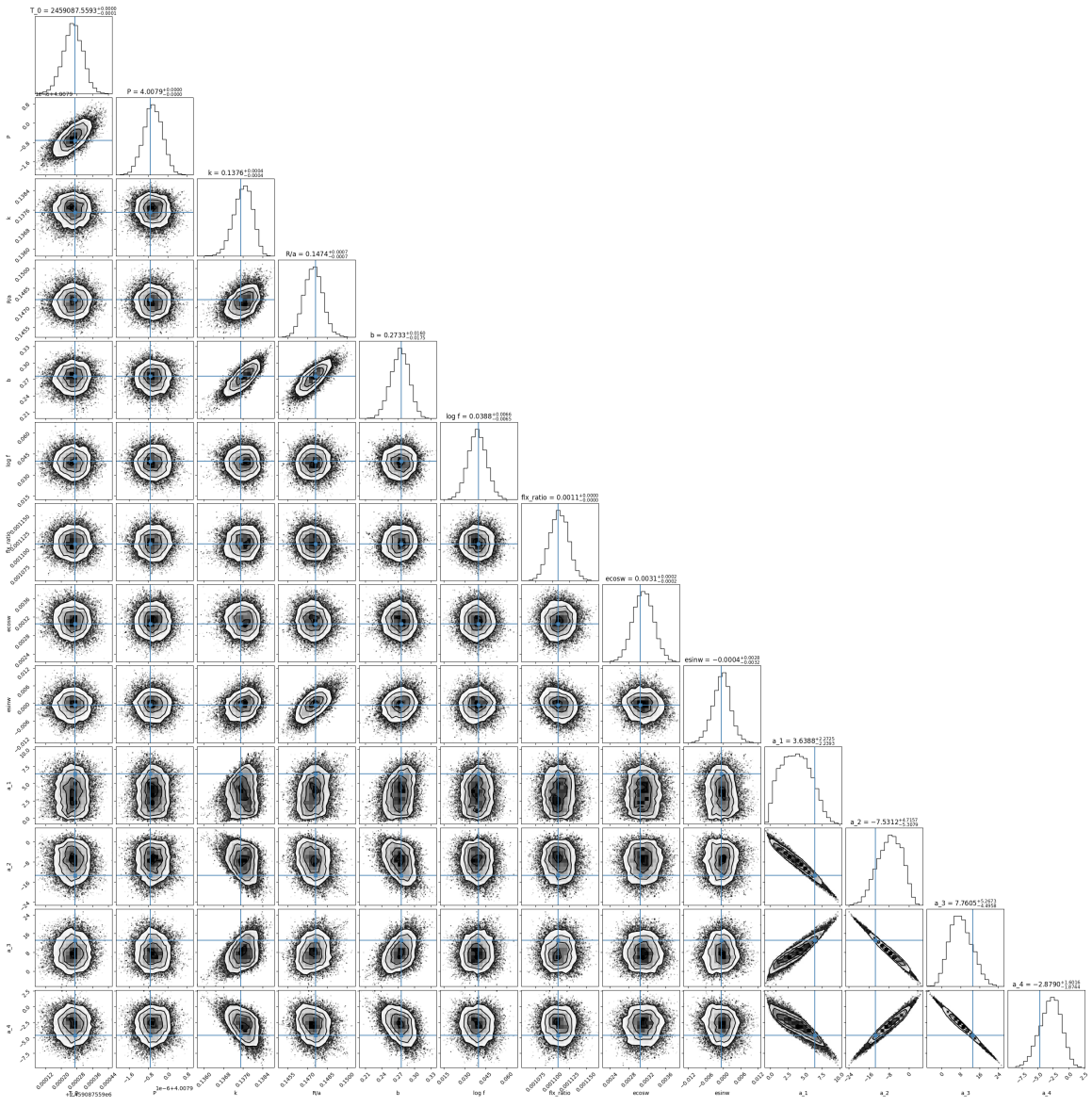

Figure A.4: Corner plots from best fits of `BATMAN` to *TESS* data using `EMCEE` from my analysis in Section 3 for J0247−51.

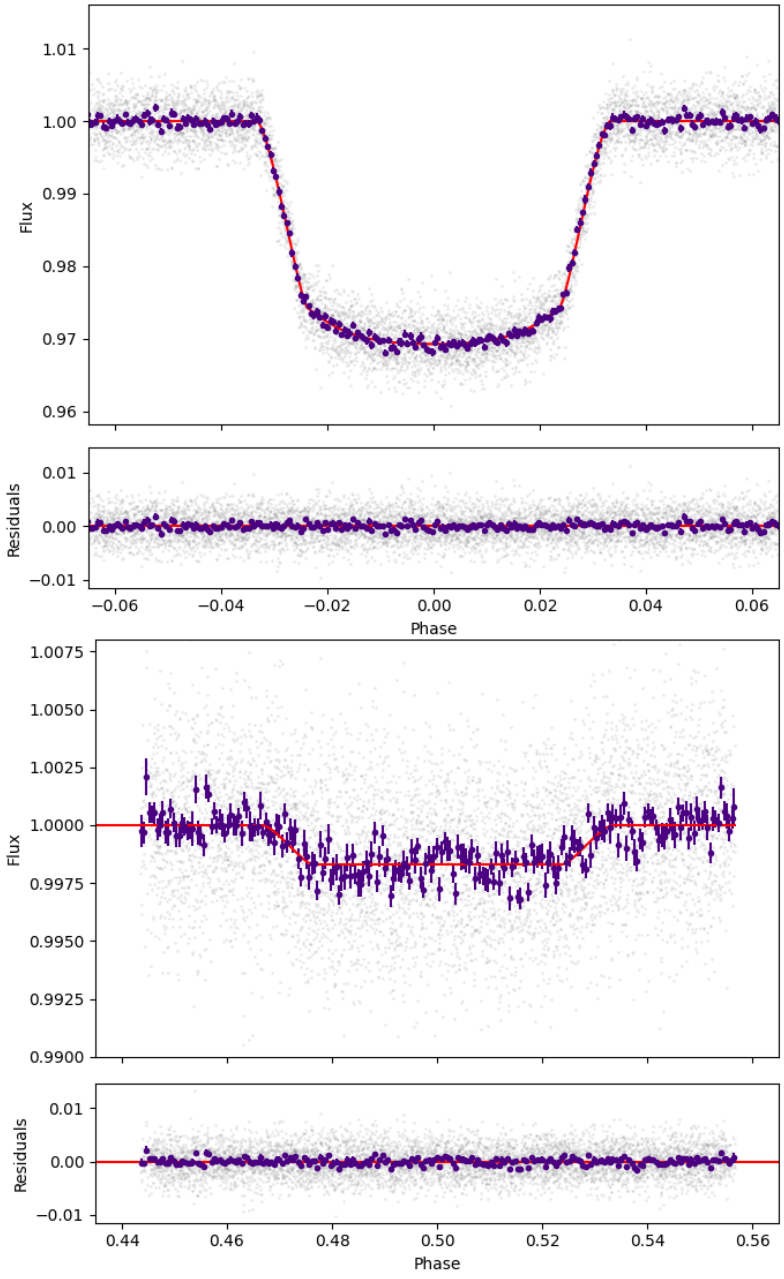

Figure A.5: *TESS* light curves (grey points) for J0400−51 with best fit of `BATMAN` from my analysis in Section 3 (red line) from `EMCEE` analysis. Data binned in 120 s intervals with errors equivalent to the mean absolute deviation are shown for reference in purple. Top panel: primary eclipse. Bottom panel: secondary eclipse.

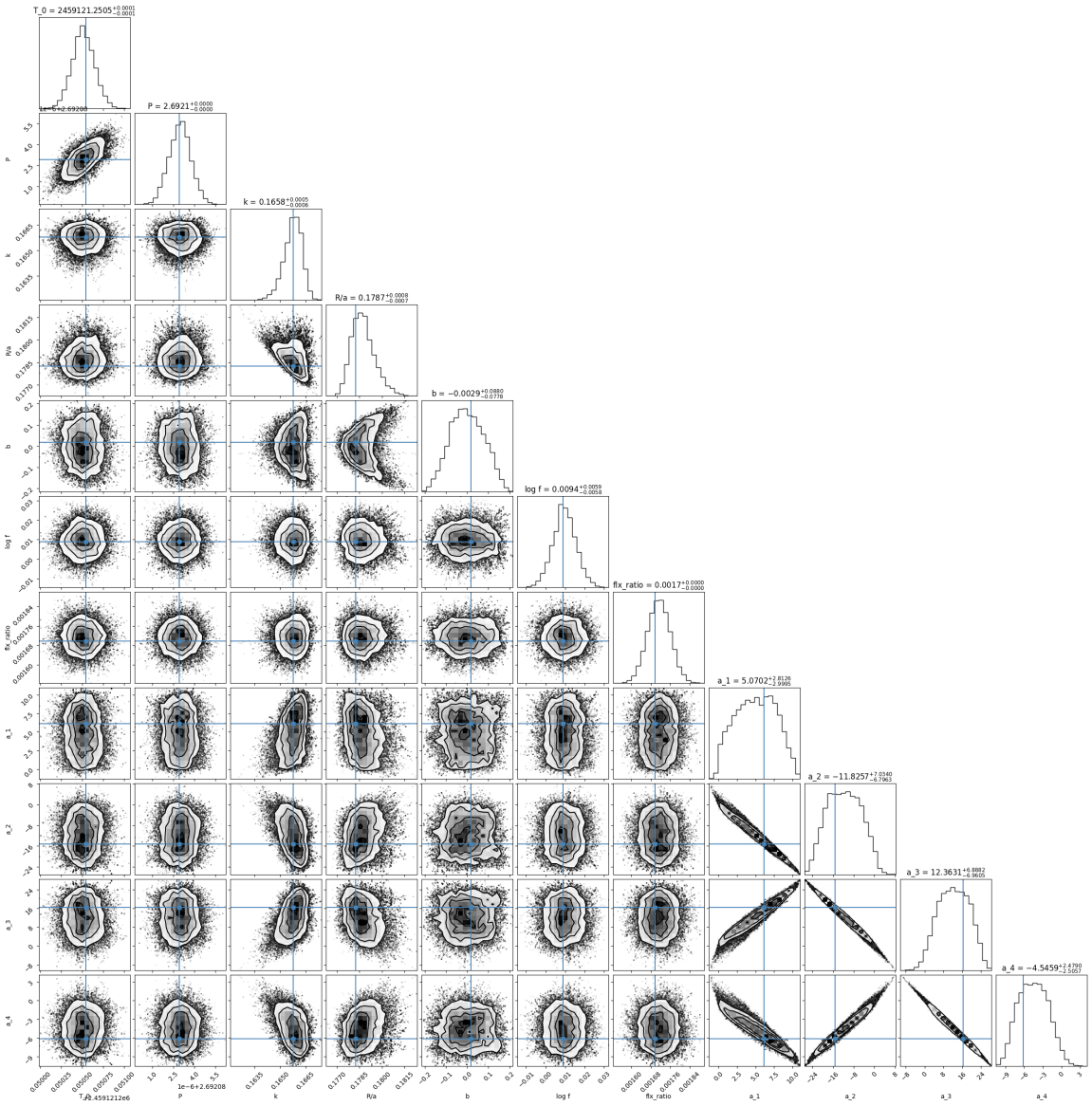

Figure A.6: Corner plots from best fits of `BATMAN` to *TESS* data using `EMCEE` from my analysis in Section 3 for J0400−51.

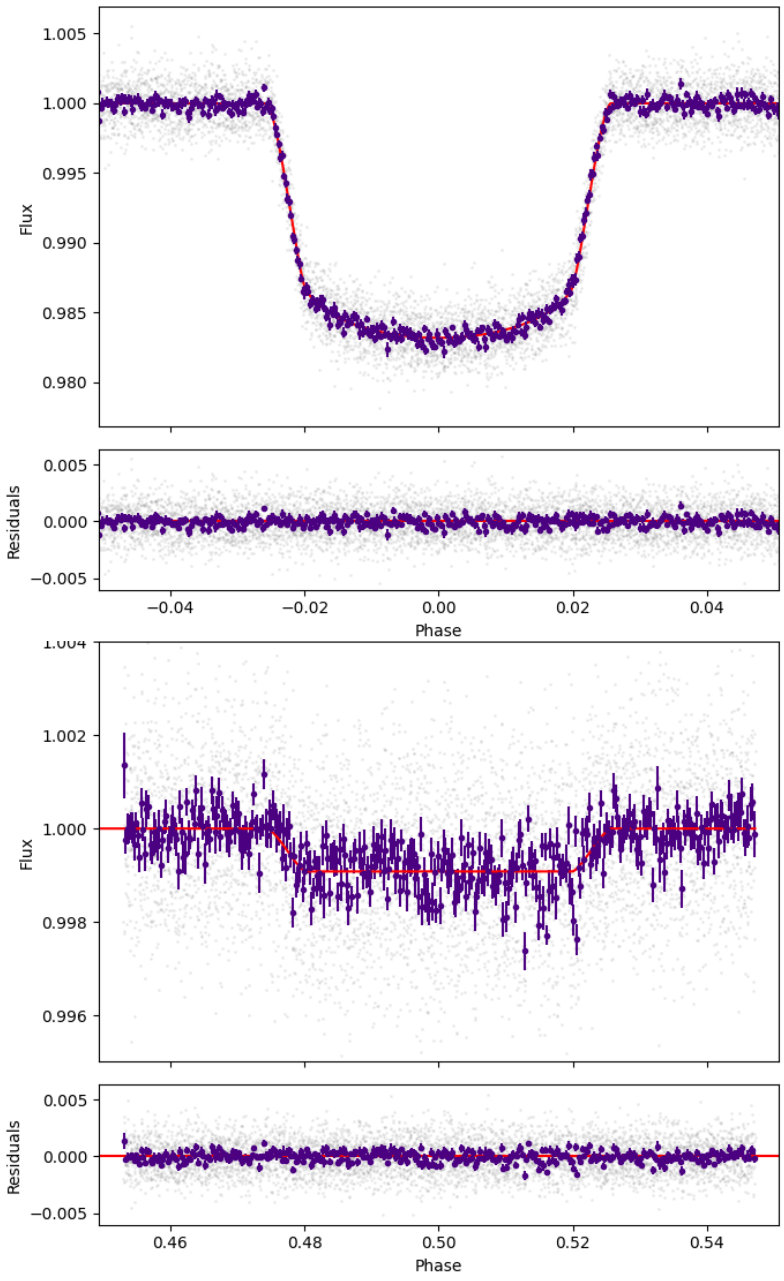

Figure A.7: *TESS* light curves (grey points) for J0432−33 with best fit of `BATMAN` from my analysis in Section 3 (red line) from `EMCEE` analysis. Data binned in 120 s intervals with errors equivalent to the mean absolute deviation are shown for reference in purple. Top panel: primary eclipse. Bottom panel: secondary eclipse.

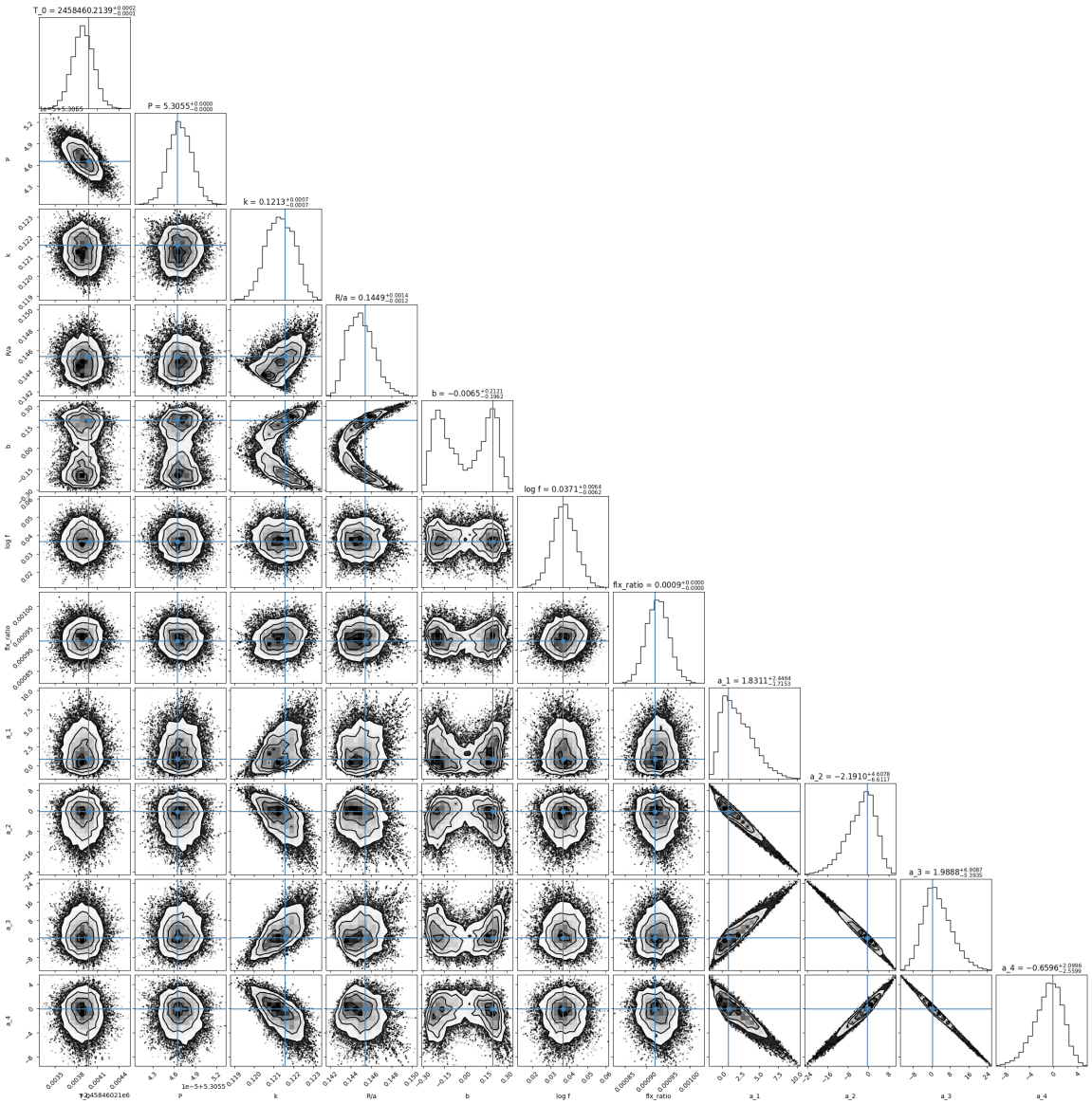

Figure A.8: Corner plots from best fits of `BATMAN` to *TESS* data using `EMCEE` from my analysis in Section 3 for J0432−33.

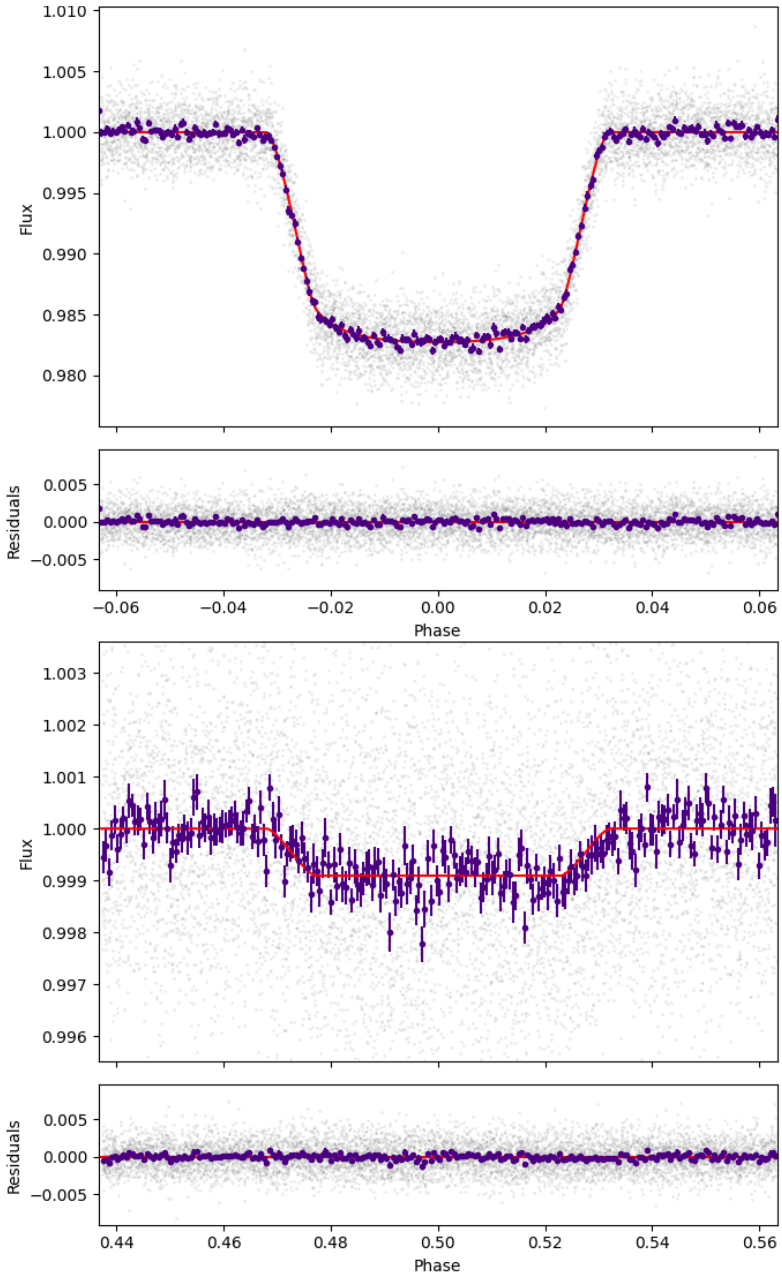

Figure A.9: *TESS* light curves (grey points) for J0440−48 with best fit of `BATMAN` from my analysis in Section 3 (red line) from `EMCEE` analysis. Data binned in 120 s intervals with errors equivalent to the mean absolute deviation are shown for reference in purple. Top panel: primary eclipse. Bottom panel: secondary eclipse.

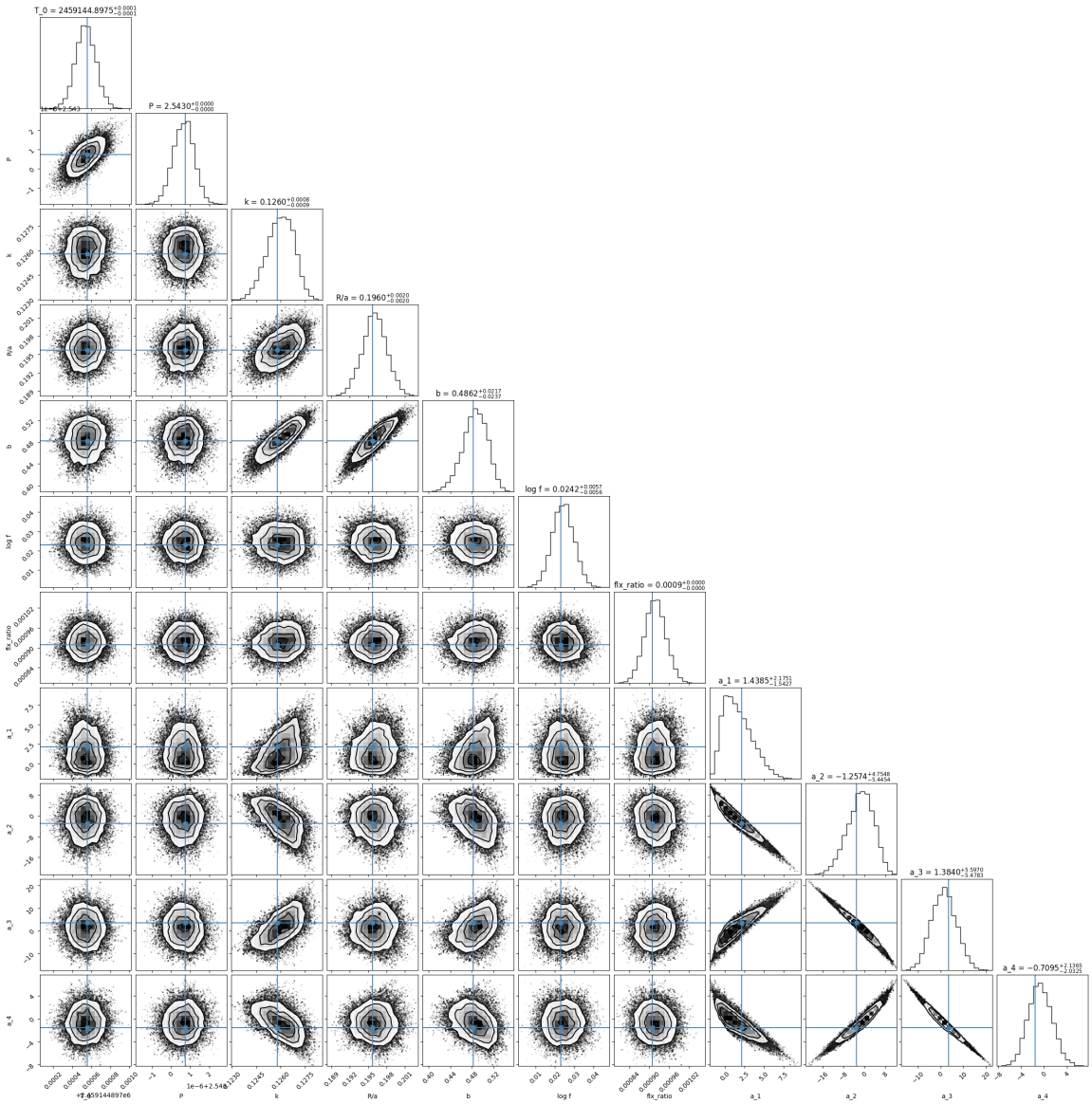

Figure A.10: Corner plots from best fits of `BATMAN` to *TESS* data using `EMCEE` from my analysis in Section 3 for J0440−48.

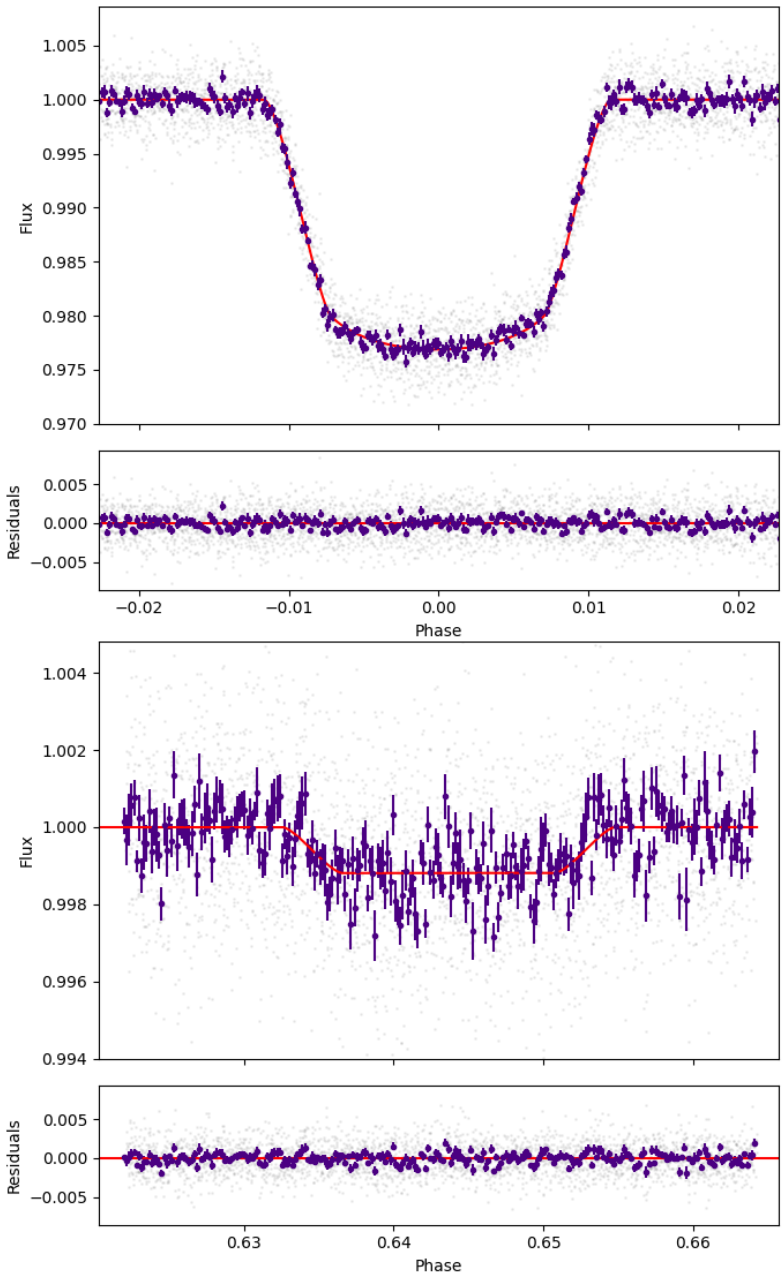

Figure A.11: *TESS* light curves (grey points) for J0500−46 with best fit of `BATMAN` from my analysis in Section 3 (red line) from `EMCEE` analysis. Data binned in 120 s intervals with errors equivalent to the mean absolute deviation are shown for reference in purple. Top panel: primary eclipse. Bottom panel: secondary eclipse.

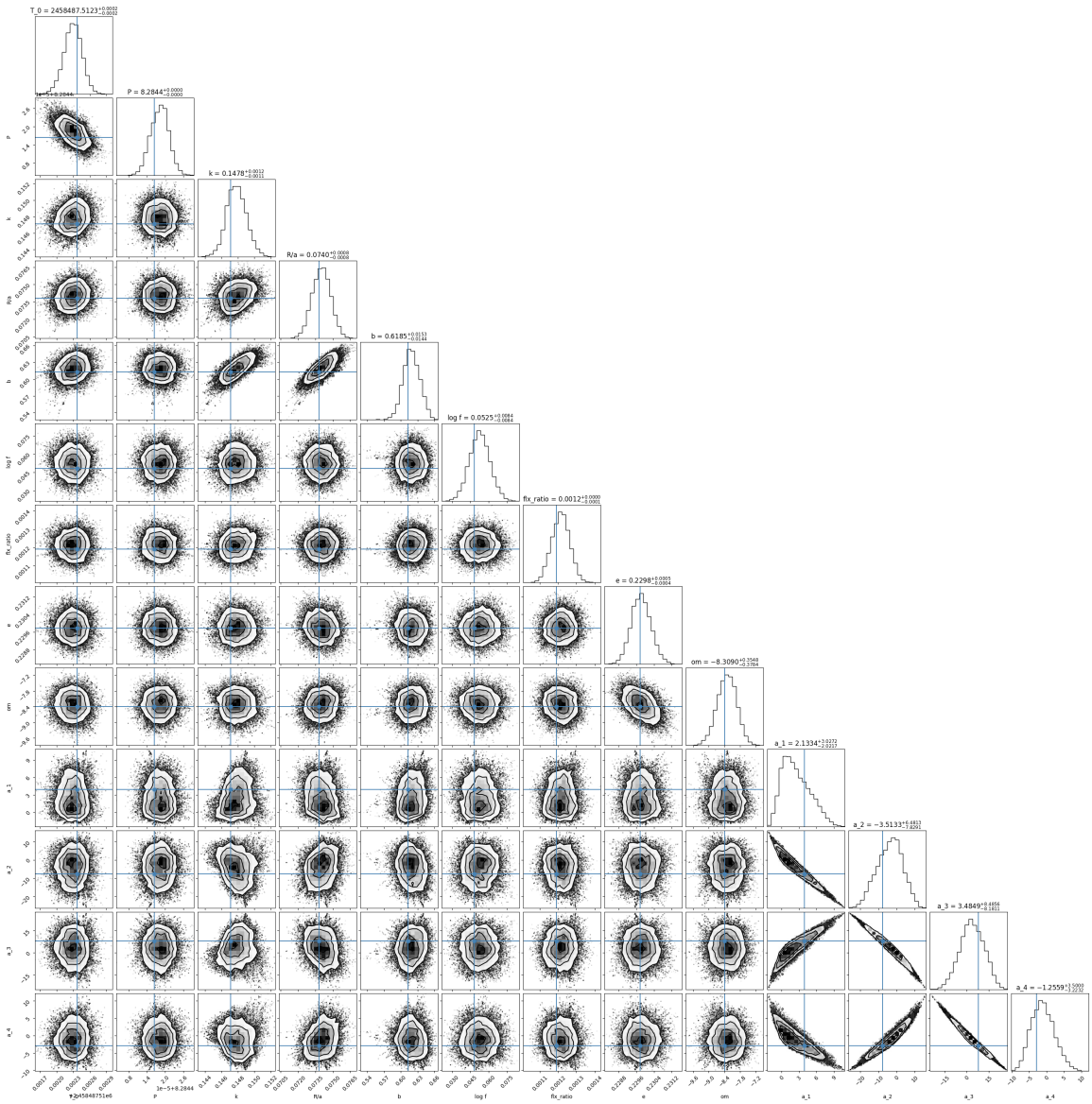

Figure A.12: Corner plots from best fits of `BATMAN` to *TESS* data using `EMCEE` from my analysis in Section 3 for J0500−46.

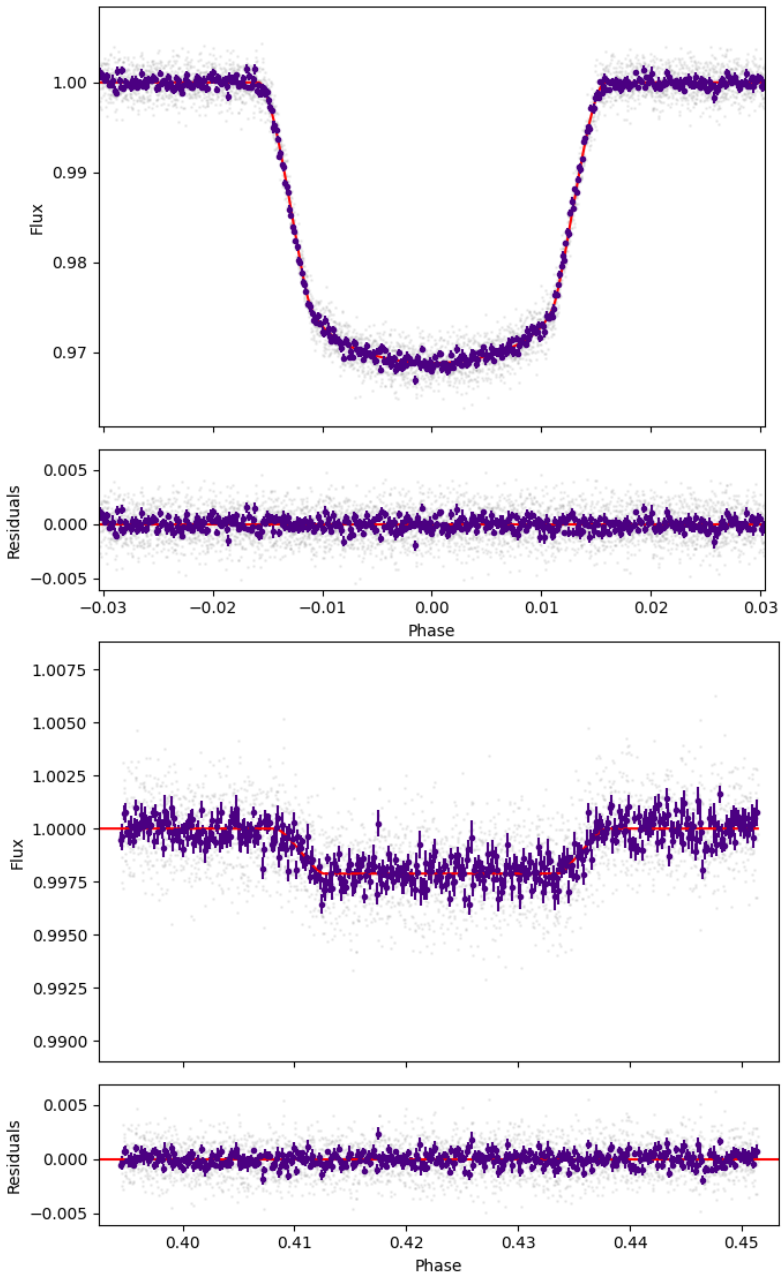

Figure A.13: *TESS* light curves (grey points) for J0526−34 with best fit of `BATMAN` from my analysis in Section 3 (red line) from `EMCEE` analysis. Data binned in 120 s intervals with errors equivalent to the mean absolute deviation are shown for reference in purple. Top panel: primary eclipse. Bottom panel: secondary eclipse.

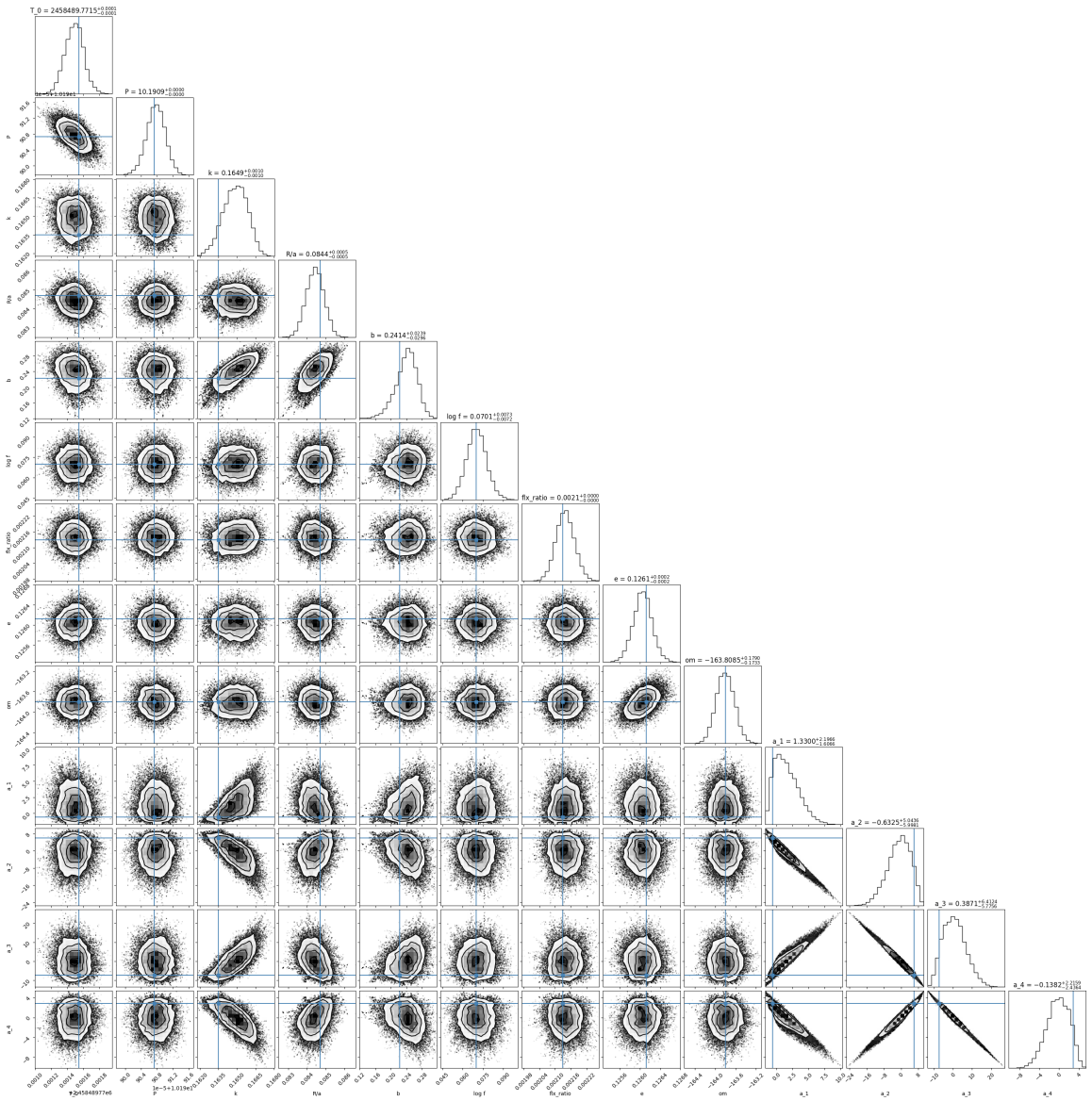

Figure A.14: Corner plots from best fits of `BATMAN` to *TESS* data using `EMCEE` from my analysis in Section 3 for J0526−34.

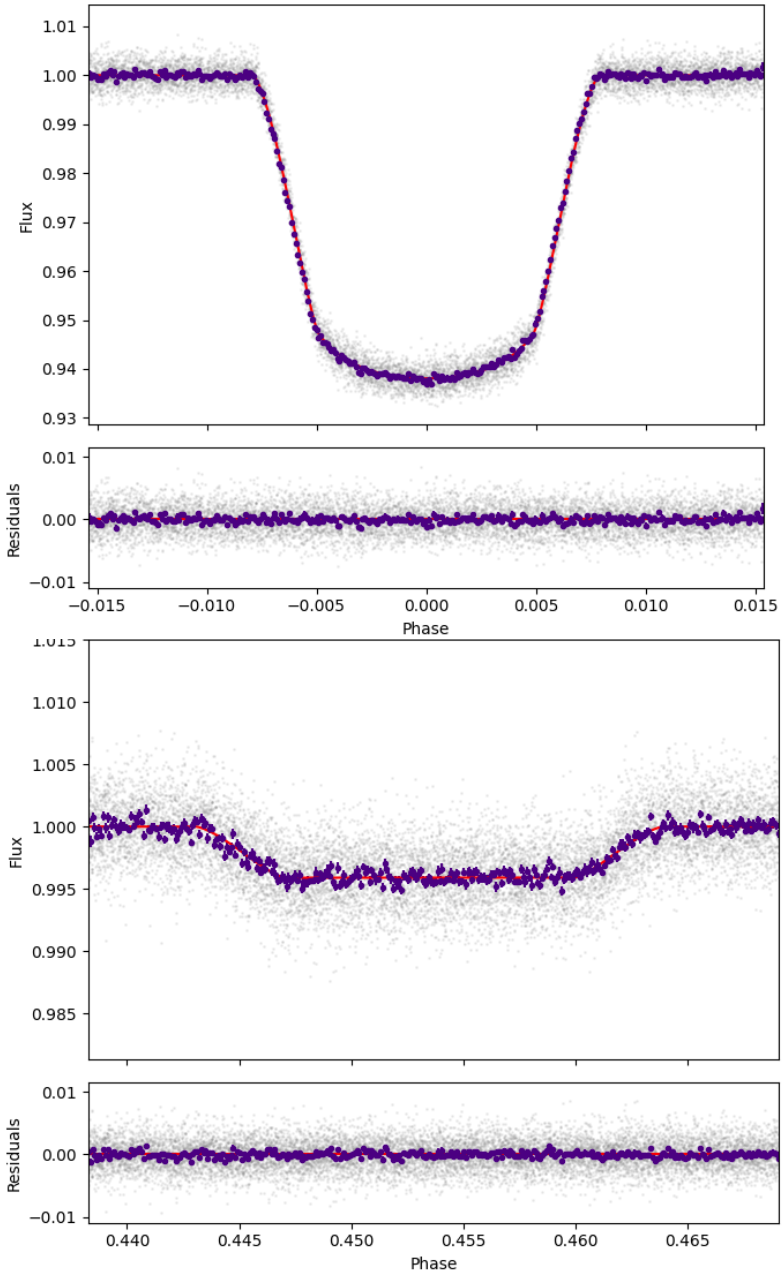

Figure A.15: *TESS* light curves (grey points) for J0608−59 with best fit of `BATMAN` from my analysis in Section 3 (red line) from `EMCEE` analysis. Data binned in 120 s intervals with errors equivalent to the mean absolute deviation are shown for reference in purple. Top panel: primary eclipse. Bottom panel: secondary eclipse.

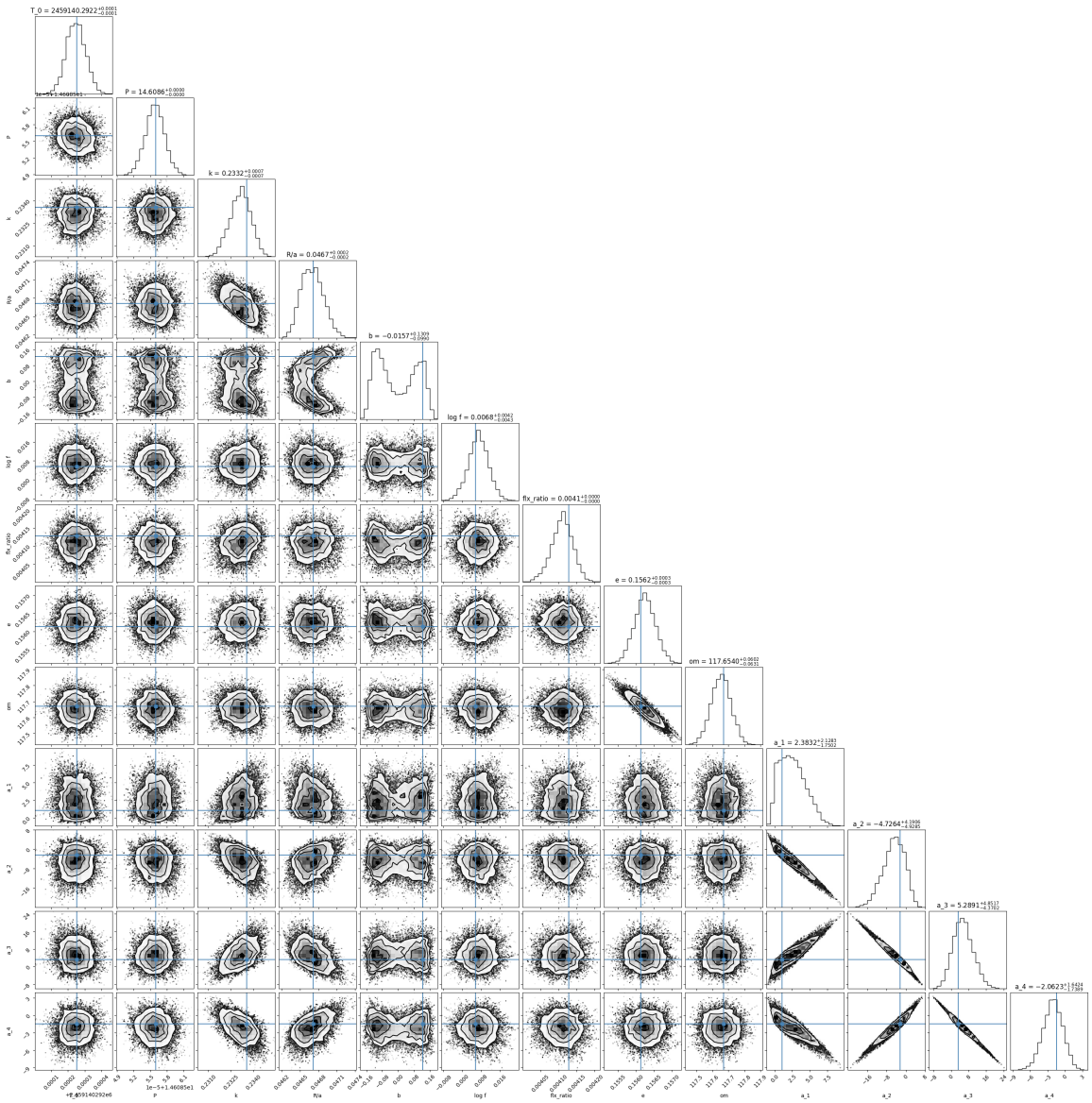

Figure A.16: Corner plots from best fits of `BATMAN` to *TESS* data using `EMCEE` from my analysis in Section 3 for J0608−59.

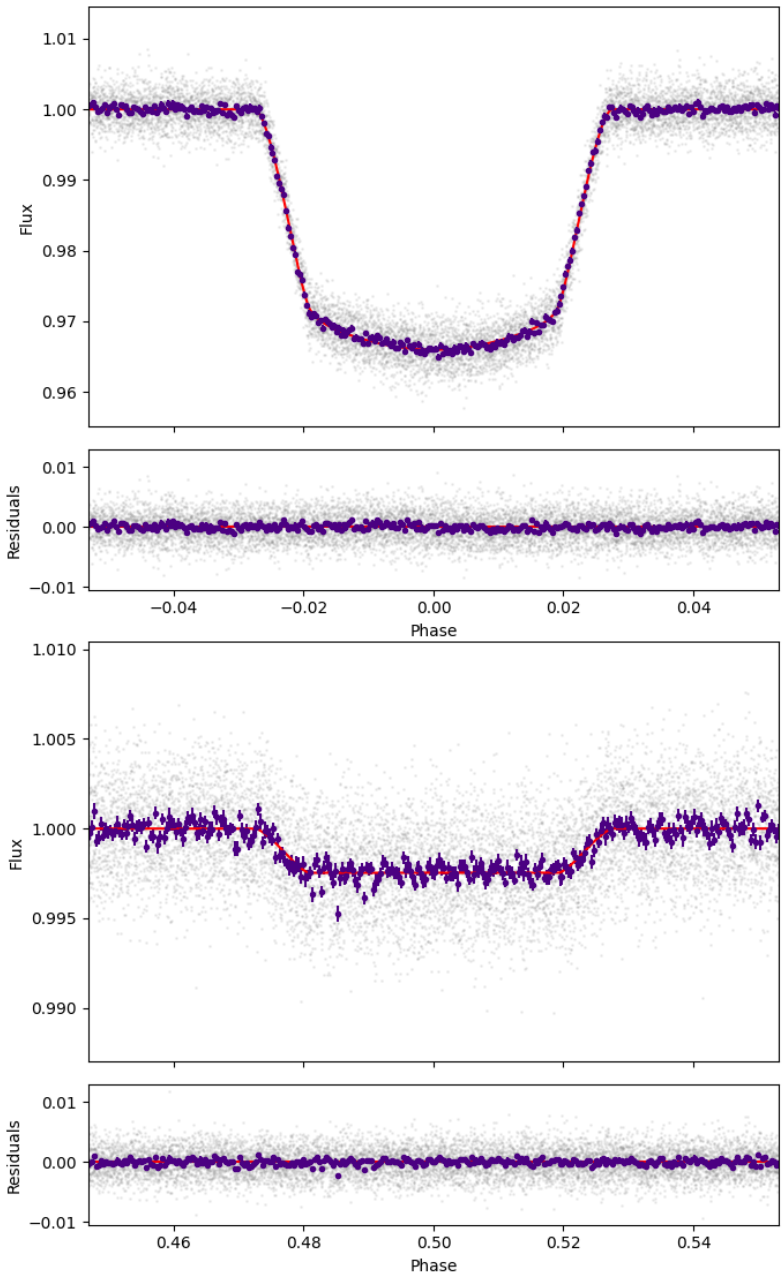

Figure A.17: *TESS* light curves (grey points) for J0625−43 with best fit of `BATMAN` from my analysis in Section 3 (red line) from `EMCEE` analysis. Data binned in 120 s intervals with errors equivalent to the mean absolute deviation are shown for reference in purple. Top panel: primary eclipse. Bottom panel: secondary eclipse.

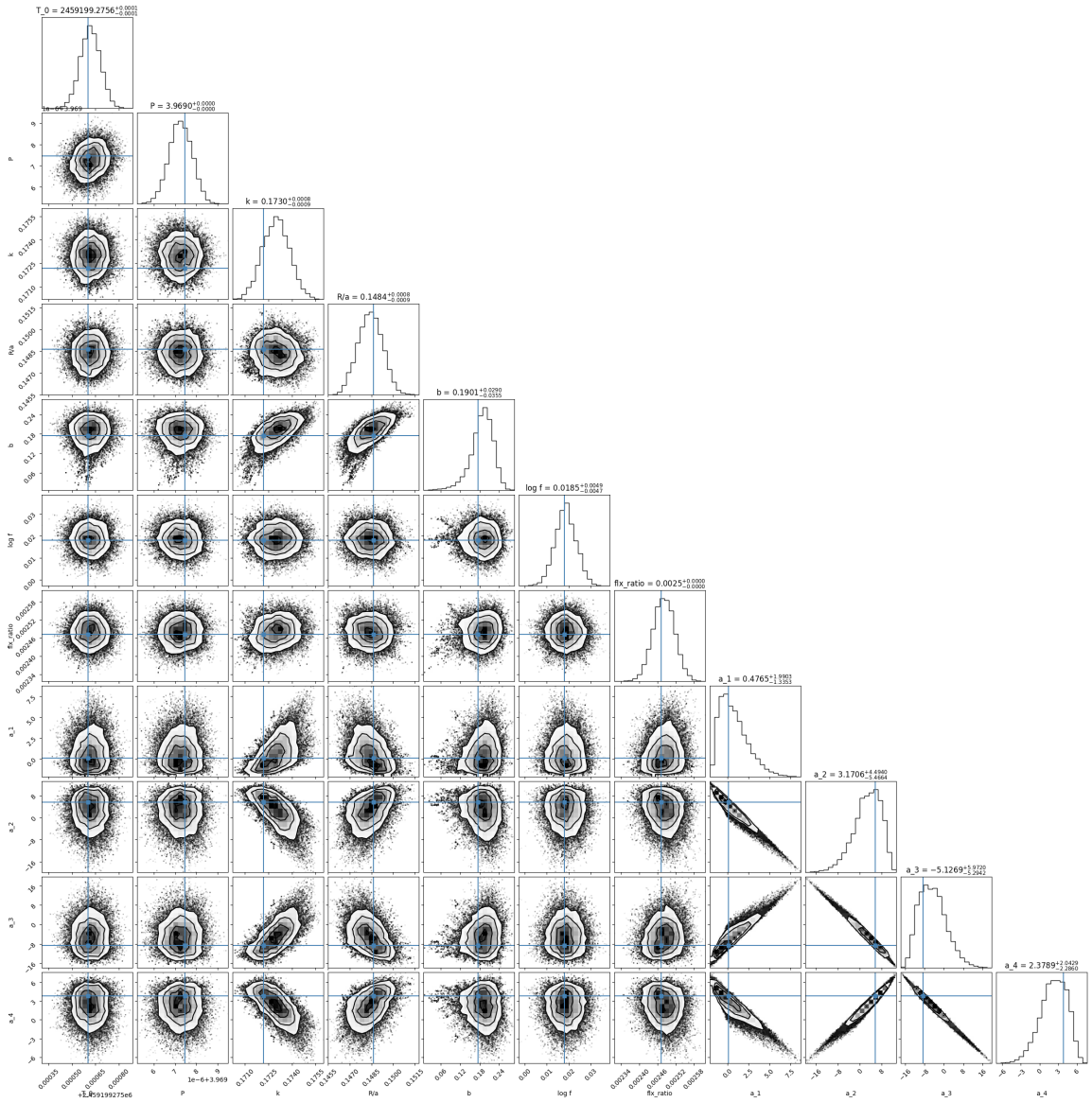

Figure A.18: Corner plots from best fits of `BATMAN` to *TESS* data using `EMCEE` from my analysis in Section 3 for J0625−43.

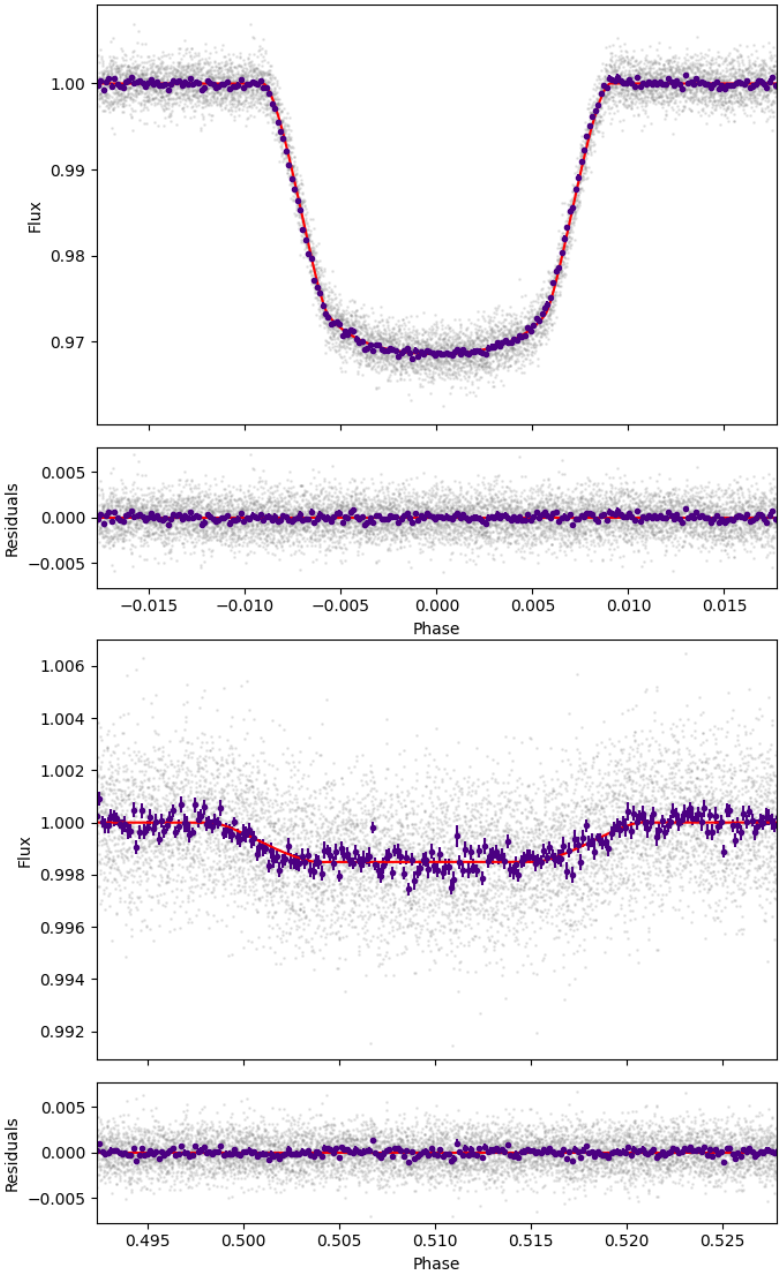

Figure A.19: *TESS* light curves (grey points) for J0627−67 with best fit of `BATMAN` from my analysis in Section 3 (red line) from `EMCEE` analysis. Data binned in 120 s intervals with errors equivalent to the mean absolute deviation are shown for reference in purple. Top panel: primary eclipse. Bottom panel: secondary eclipse.

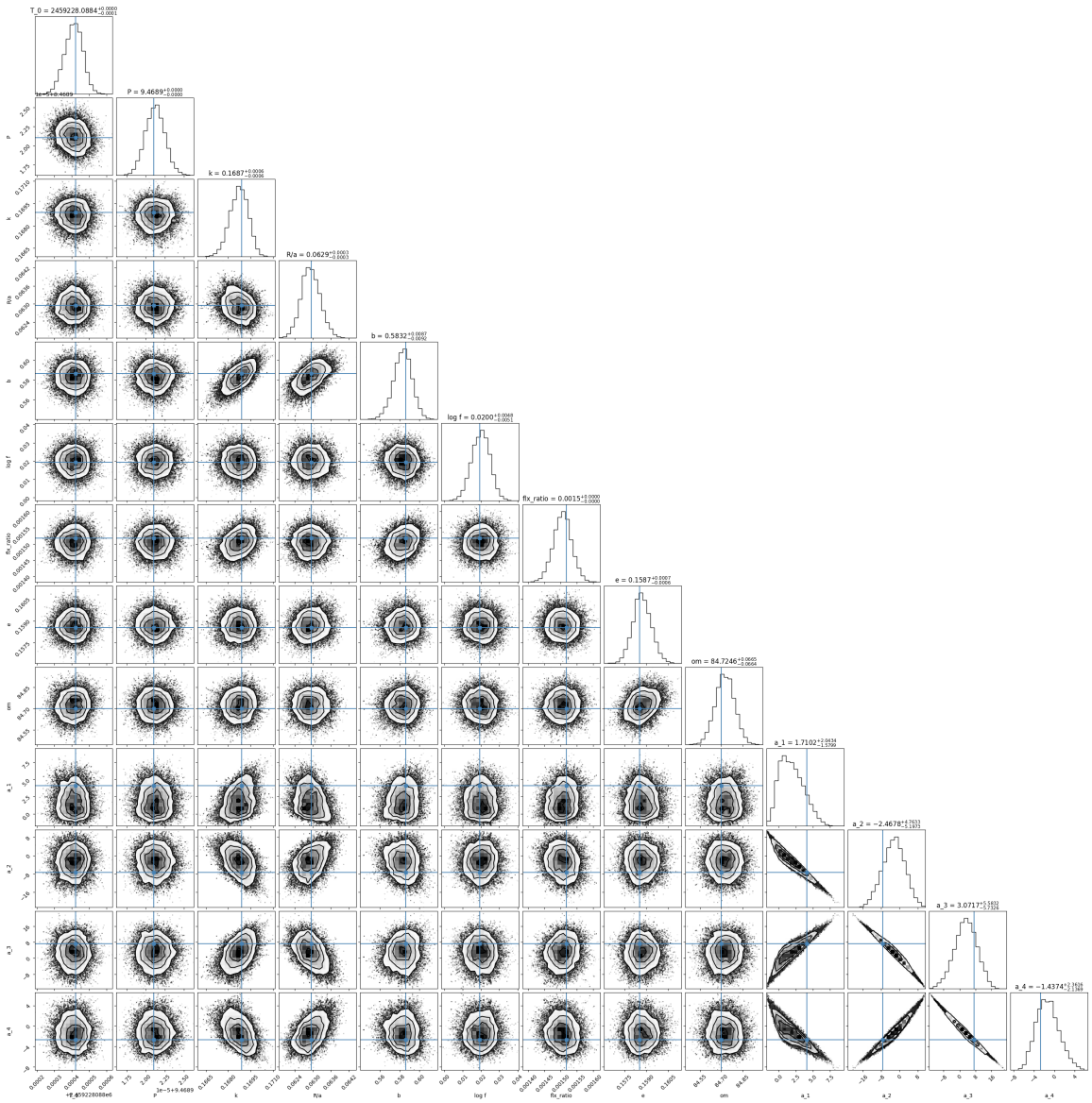

Figure A.20: Corner plots from best fits of `BATMAN` to *TESS* data using `EMCEE` from my analysis in Section 3 for J0627−67.

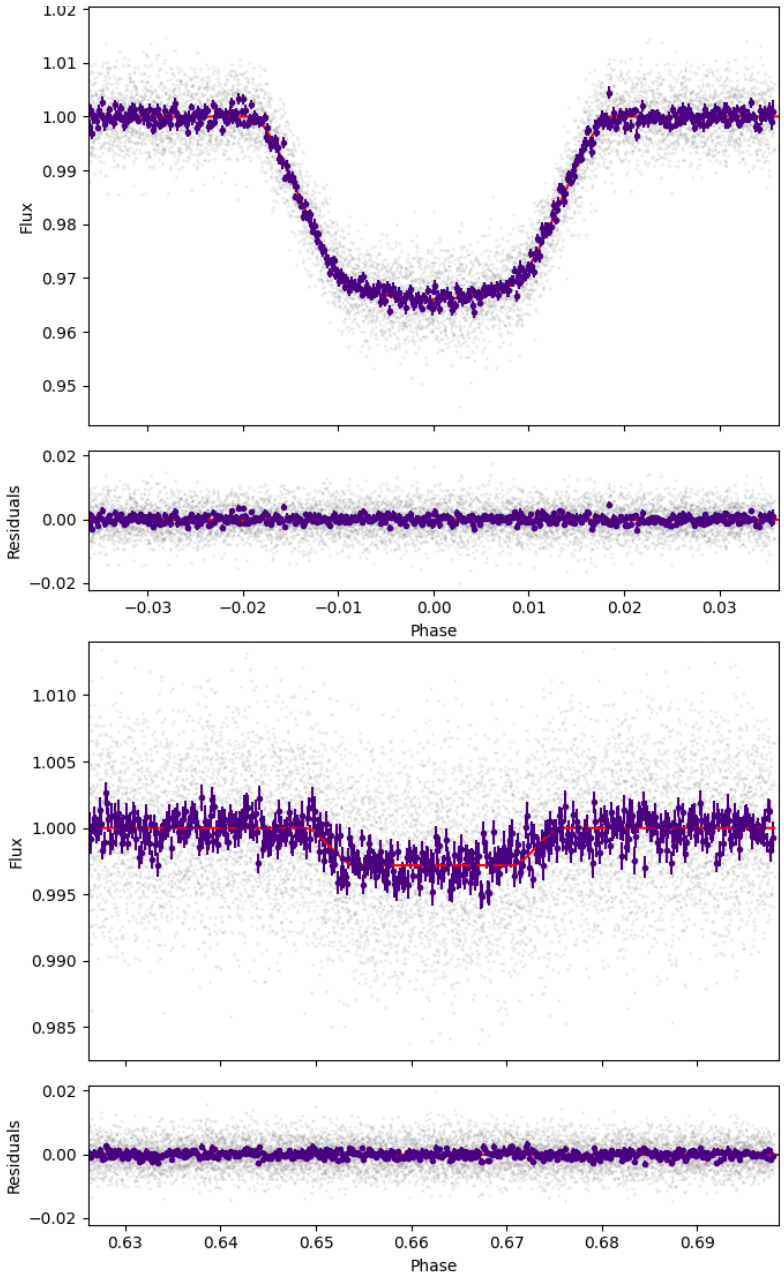

Figure A.21: *TESS* light curves (grey points) for J0709−52 with best fit of `BATMAN` from my analysis in Section 3 (red line) from `EMCEE` analysis. Data binned in 120 s intervals with errors equivalent to the mean absolute deviation are shown for reference in purple. Top panel: primary eclipse. Bottom panel: secondary eclipse.

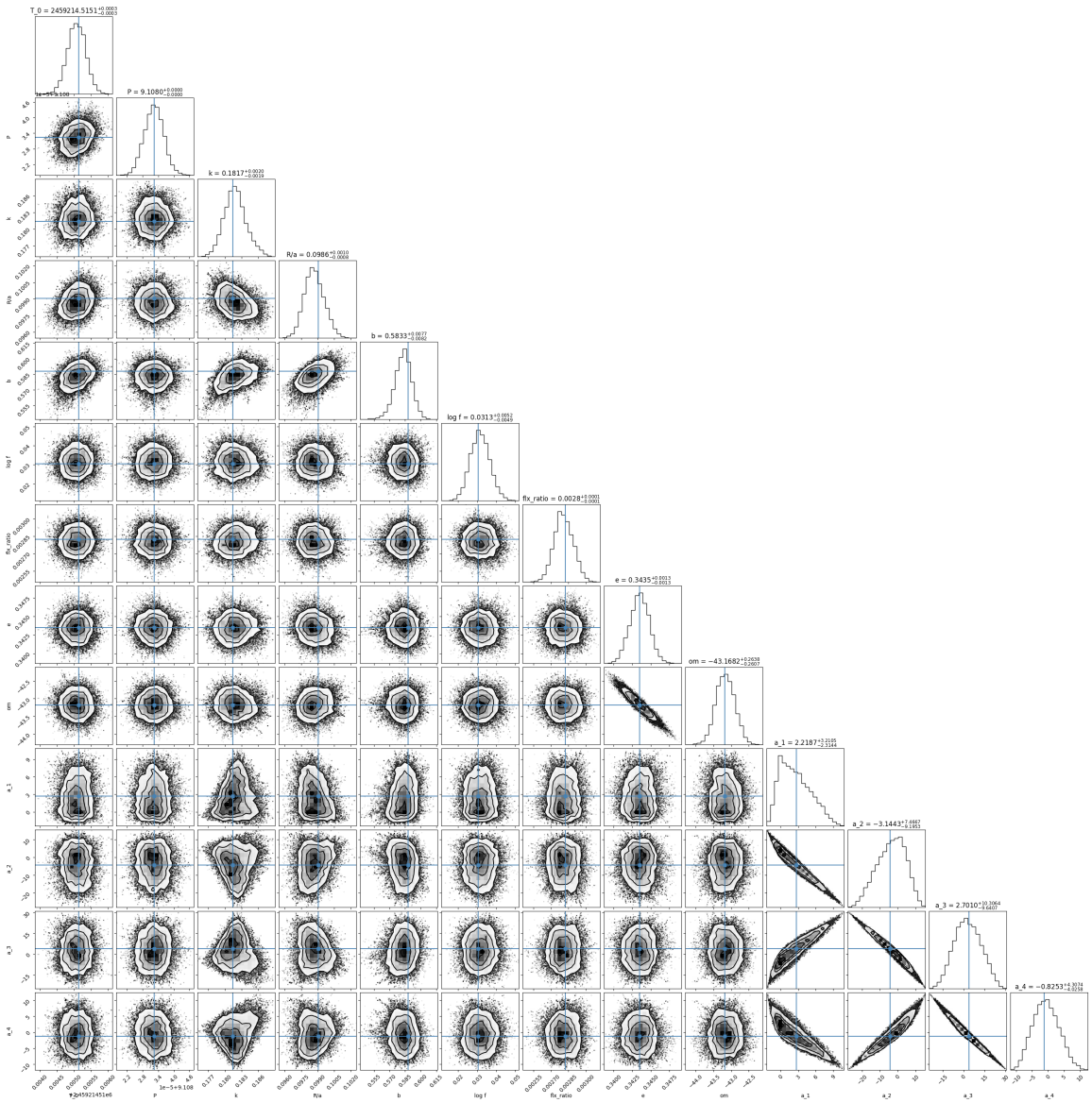

Figure A.22: Corner plots from best fits of `BATMAN` to *TESS* data using `EMCEE` from my analysis in Section 3 for J0709−52.

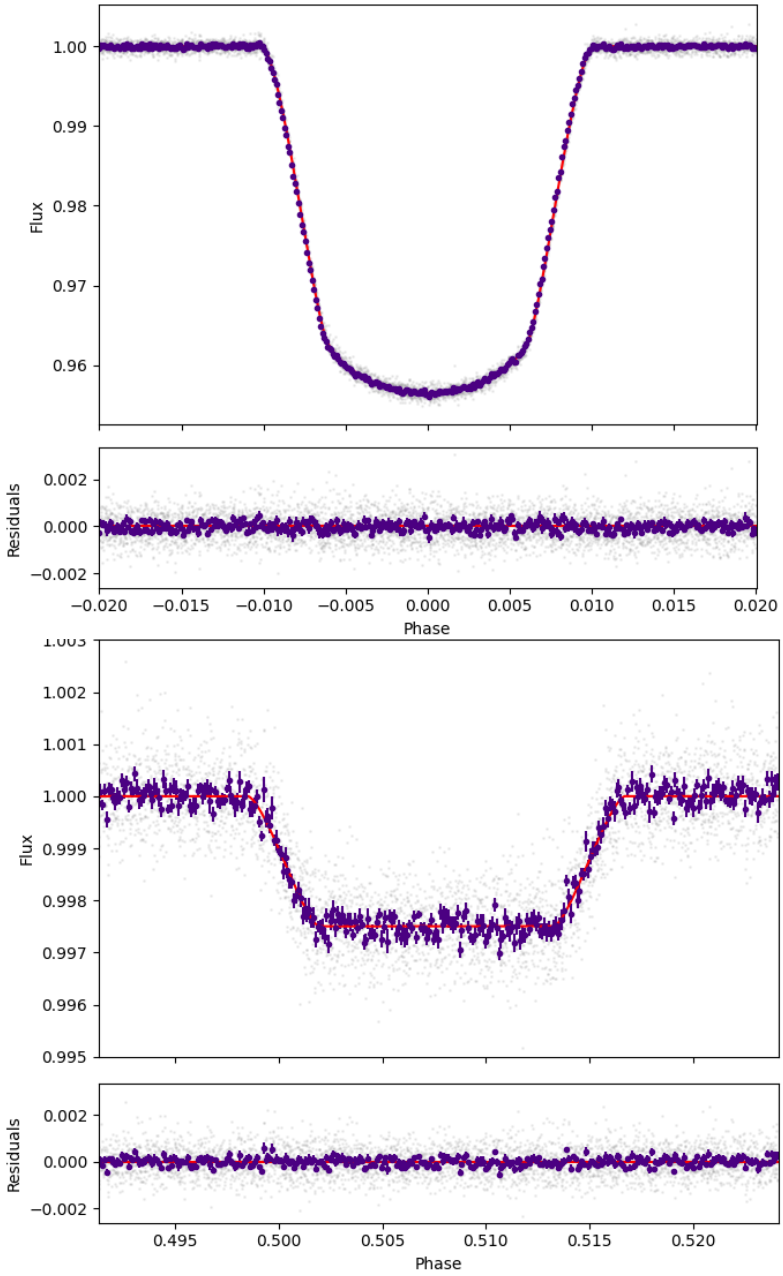

Figure A.23: *TESS* light curves (grey points) for J0723+79 with best fit of `BATMAN` from my analysis in Section 3 (red line) from `EMCEE` analysis. Data binned in 120 s intervals with errors equivalent to the mean absolute deviation are shown for reference in purple. Top panel: primary eclipse. Bottom panel: secondary eclipse.

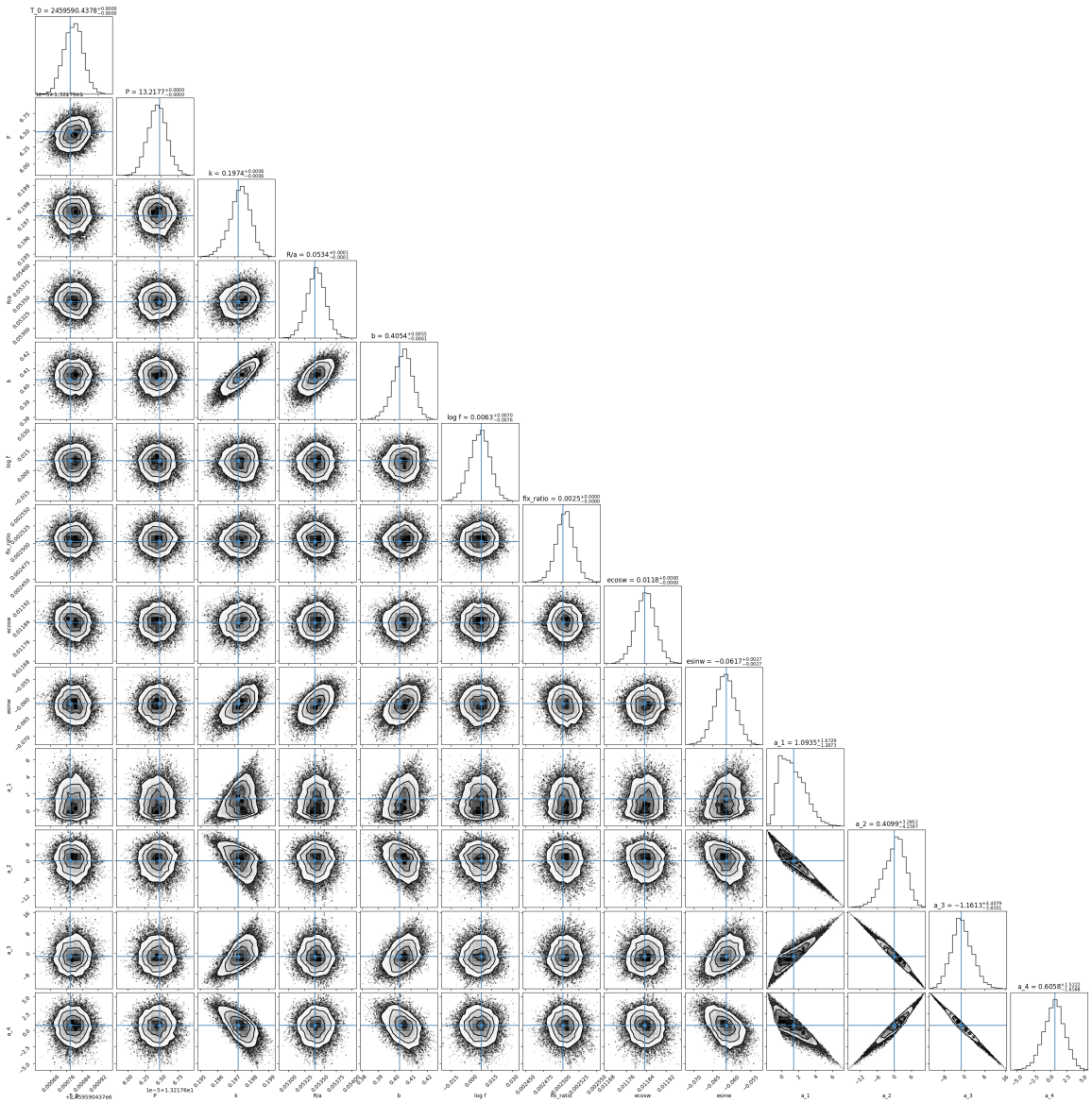

Figure A.24: Corner plots from best fits of `BATMAN` to *TESS* data using `EMCEE` from my analysis in Section 3 for J0723+79.

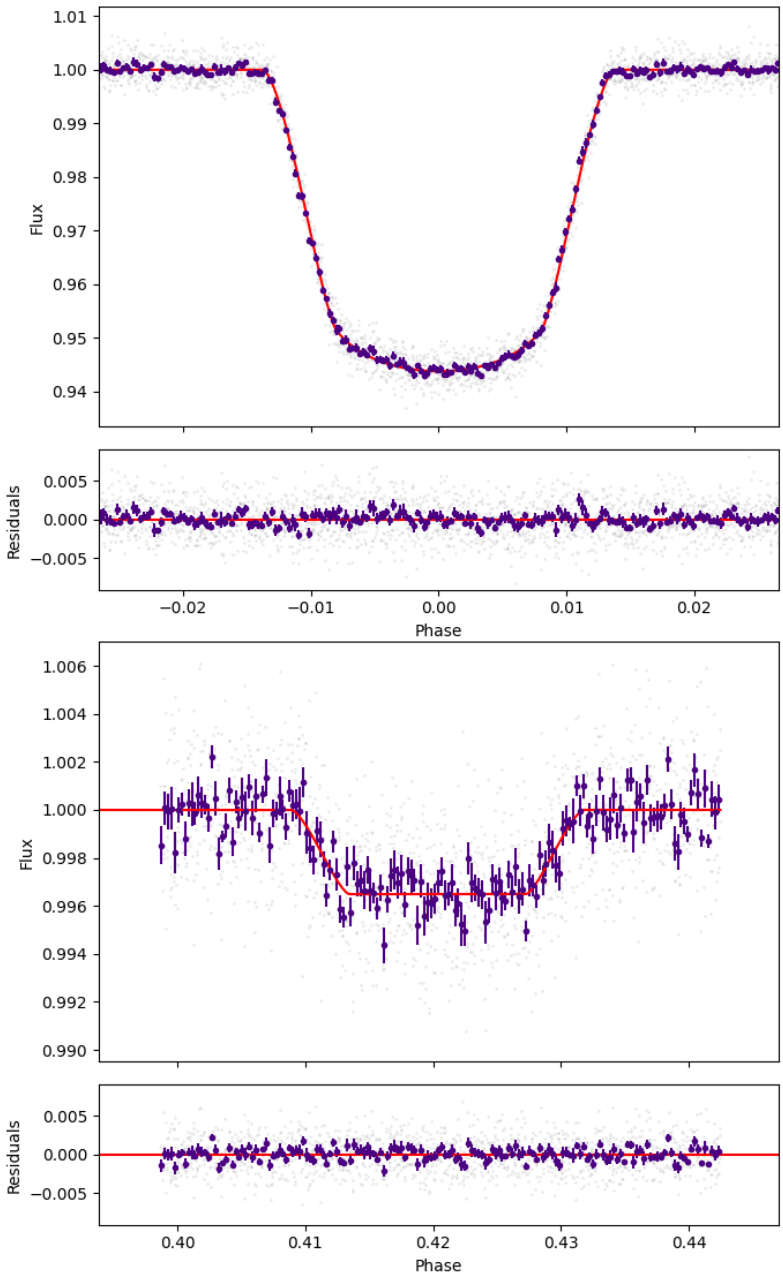

Figure A.25: *TESS* light curves (grey points) for J0829+66 with best fit of `BATMAN` from my analysis in Section 3 (red line) from `EMCEE` analysis. Data binned in 120 s intervals with errors equivalent to the mean absolute deviation are shown for reference in purple. Top panel: primary eclipse. Bottom panel: secondary eclipse.

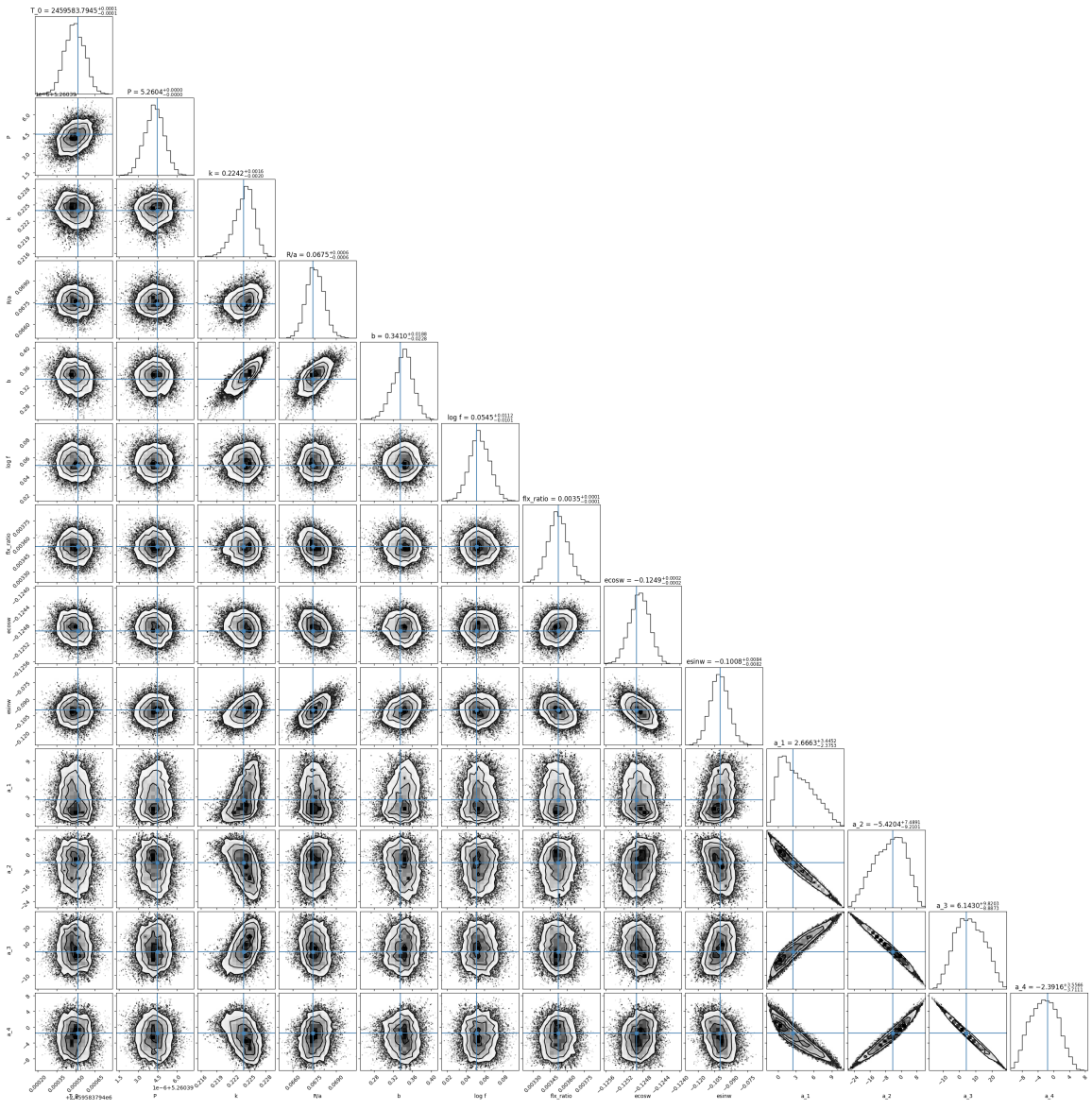

Figure A.26: Corner plots from best fits of `BATMAN` to *TESS* data using `EMCEE` from my analysis in Section 3 for J0829+66.

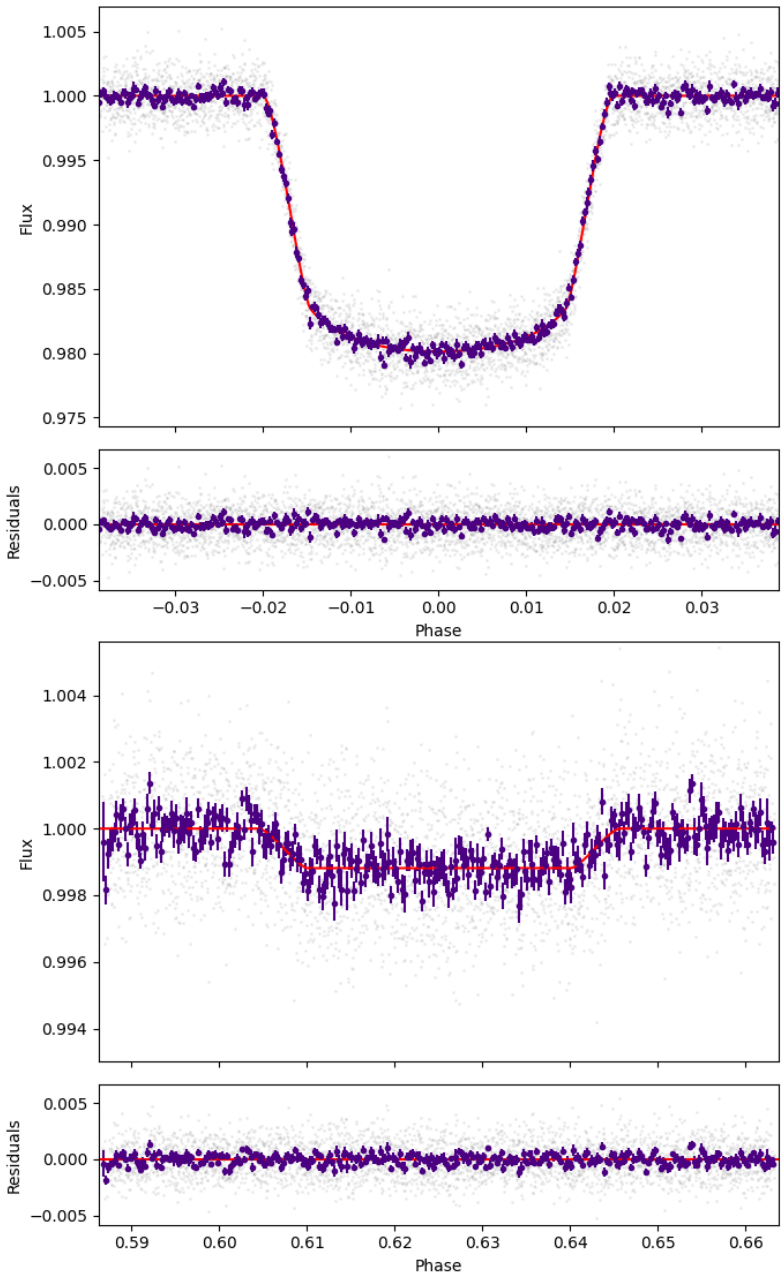

Figure A.27: *TESS* light curves (grey points) for J0941−31 with best fit of `BATMAN` from my analysis in Section 3 (red line) from `EMCEE` analysis. Data binned in 120 s intervals with errors equivalent to the mean absolute deviation are shown for reference in purple. Top panel: primary eclipse. Bottom panel: secondary eclipse.

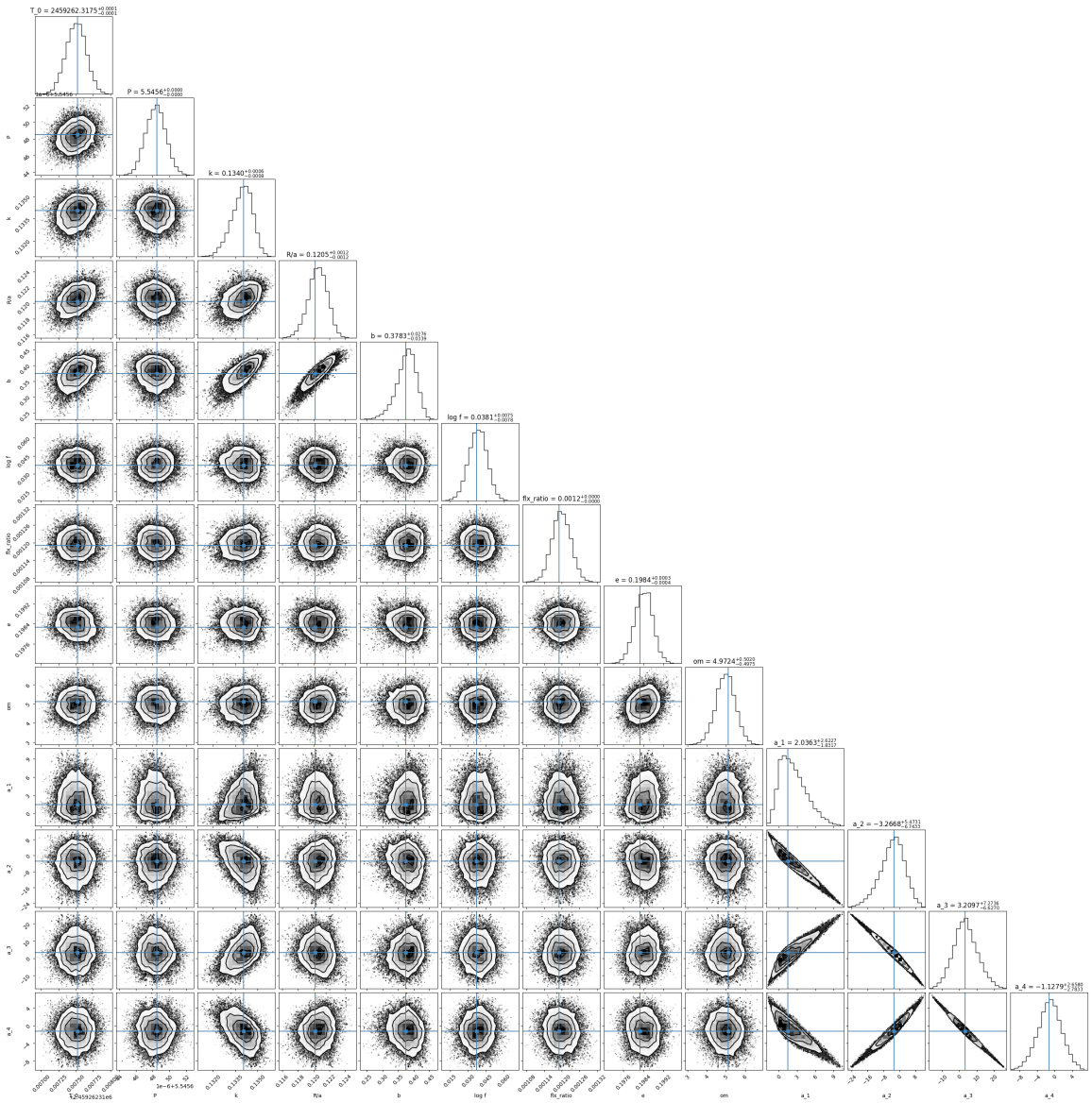

Figure A.28: Corner plots from best fits of `BATMAN` to *TESS* data using `EMCEE` from my analysis in Section 3 for J0941−31.

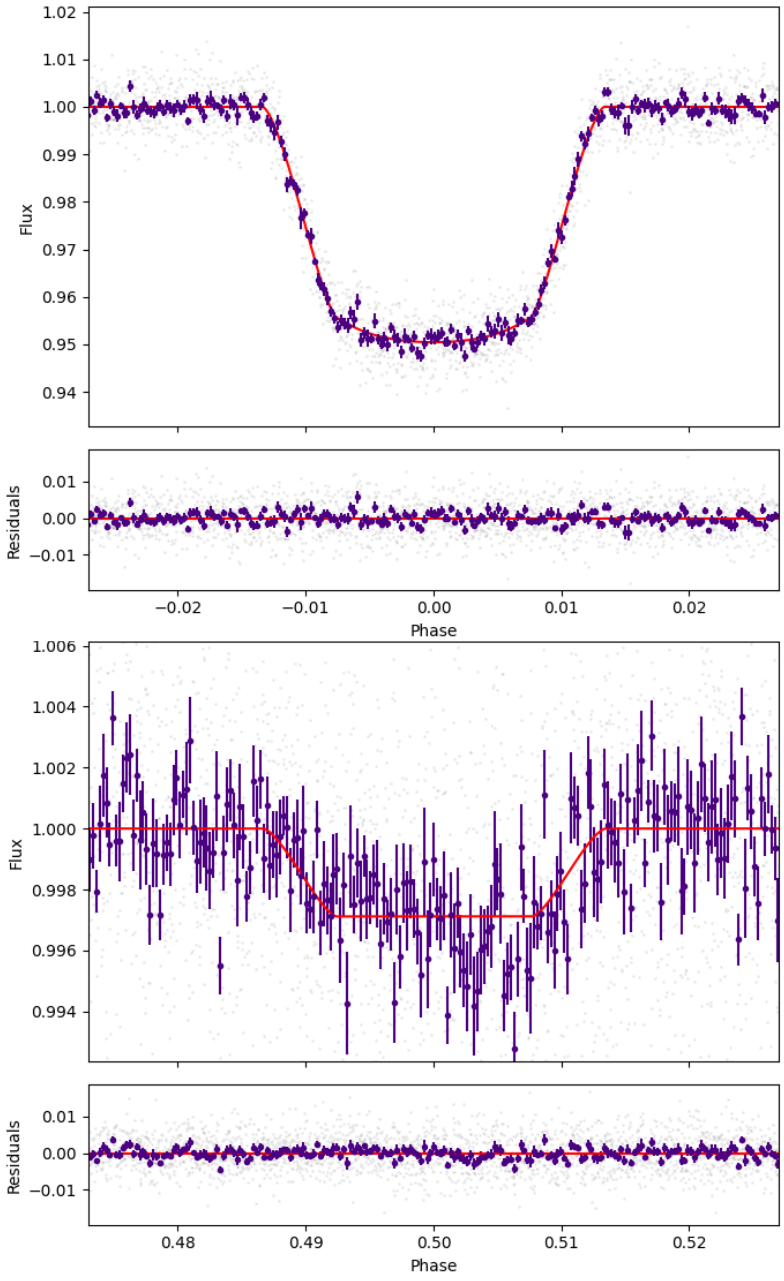

Figure A.29: *TESS* light curves (grey points) for J0955−39 with best fit of `BATMAN` from my analysis in Section 3 (red line) from `EMCEE` analysis. Data binned in 120 s intervals with errors equivalent to the mean absolute deviation are shown for reference in purple. Top panel: primary eclipse. Bottom panel: secondary eclipse.

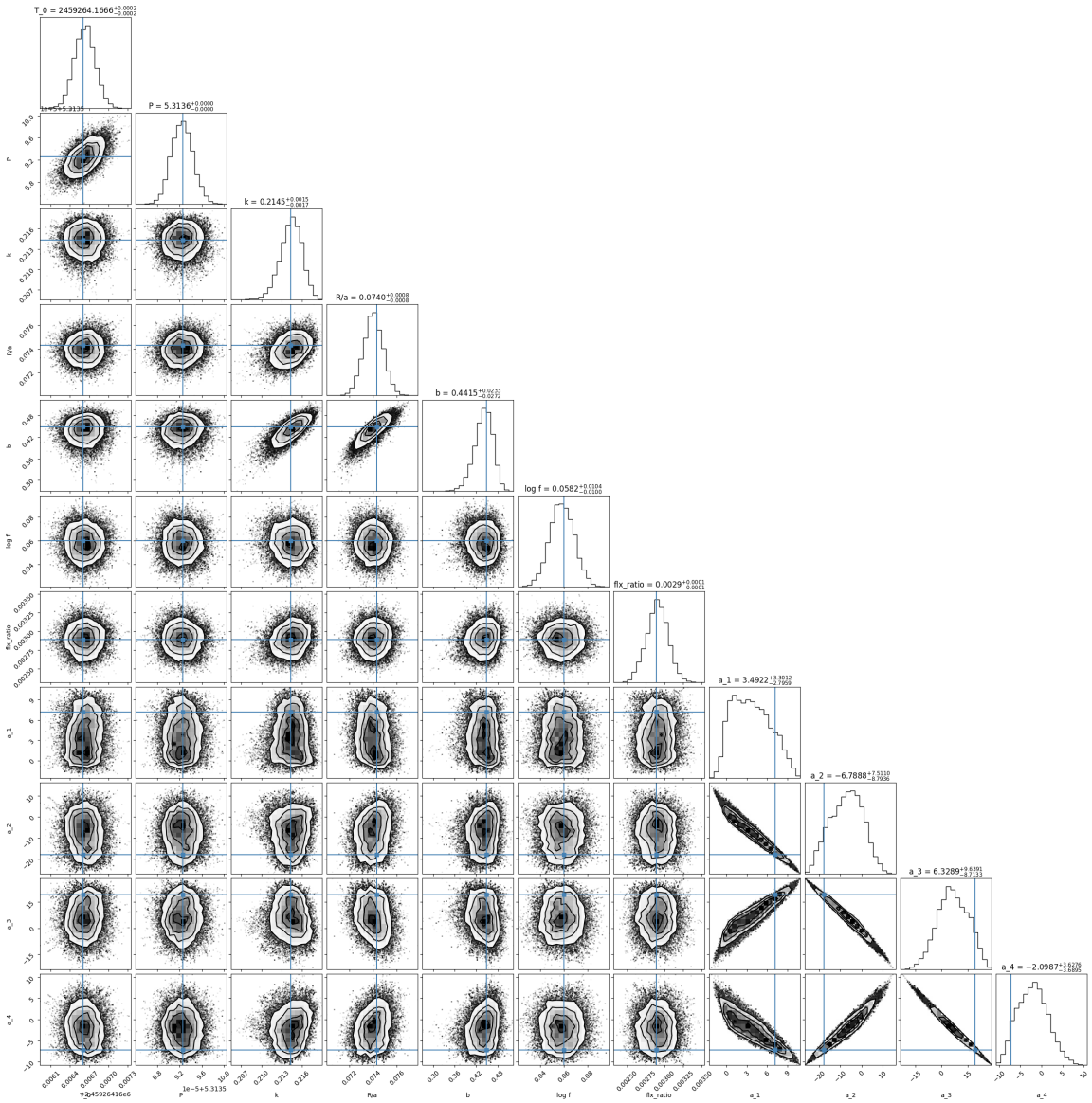

Figure A.30: Corner plots from best fits of `BATMAN` to *TESS* data using `EMCEE` from my analysis in Section 3 for J0955−39.

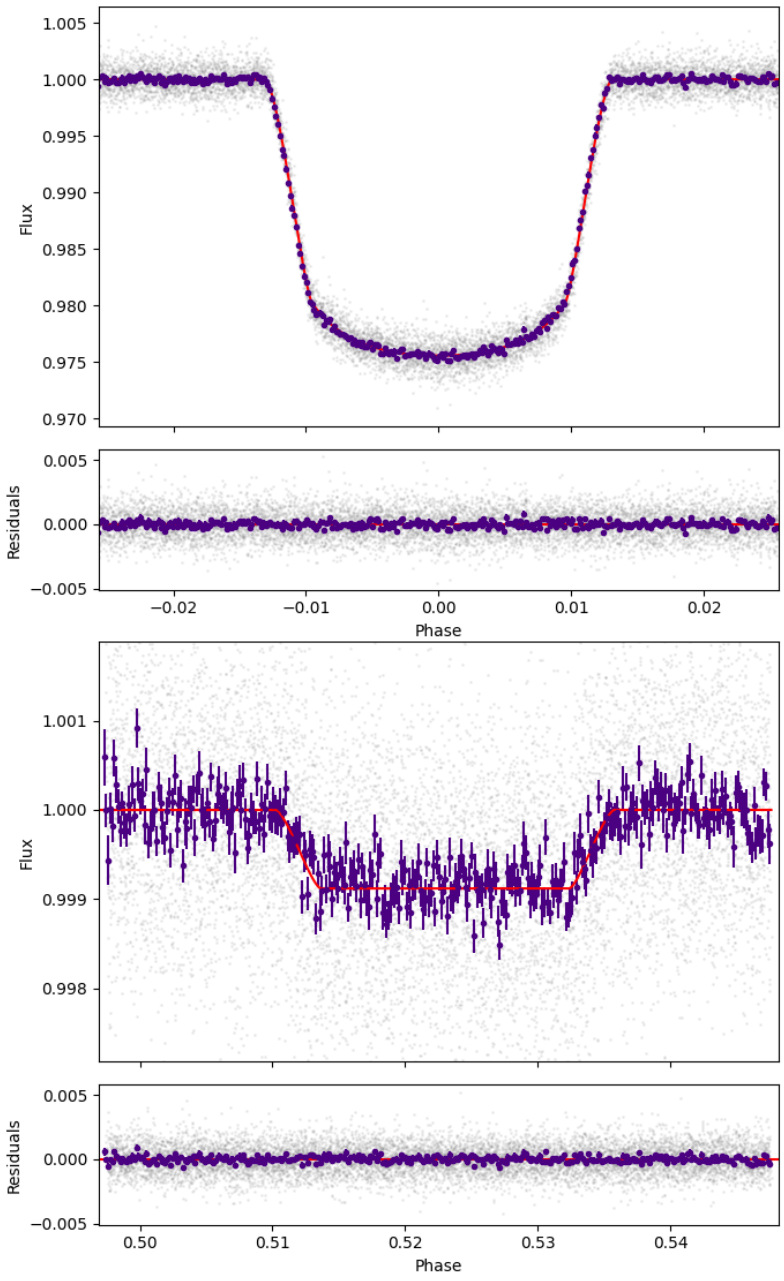

Figure A.31: *TESS* light curves (grey points) for J1626+57 with best fit of `BATMAN` from my analysis in Section 3 (red line) from `EMCEE` analysis. Data binned in 120 s intervals with errors equivalent to the mean absolute deviation are shown for reference in purple. Top panel: primary eclipse. Bottom panel: secondary eclipse.

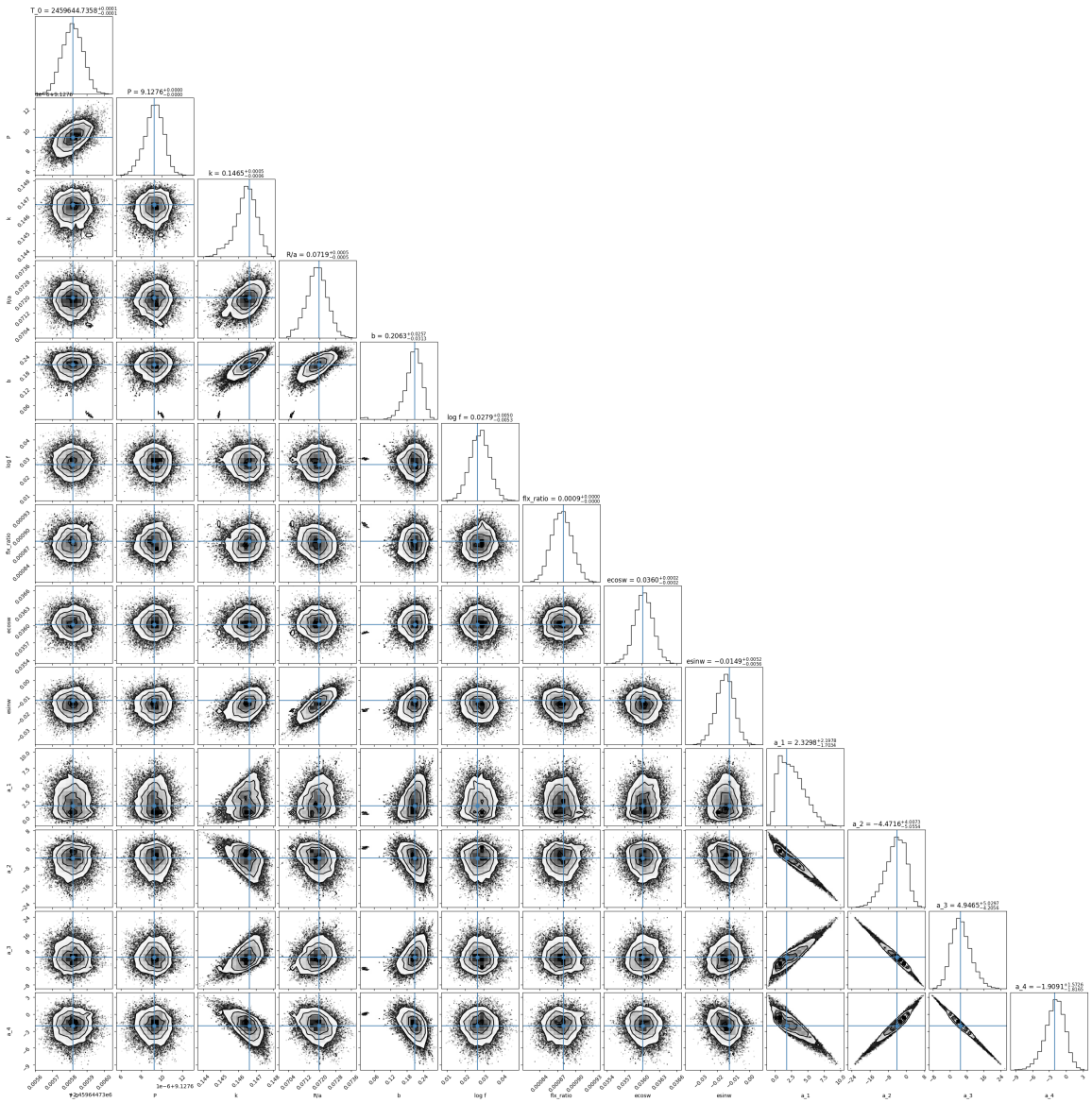

Figure A.32: Corner plots from best fits of `BATMAN` to *TESS* data using `EMCEE` from my analysis in Section 3 for J1626+57.

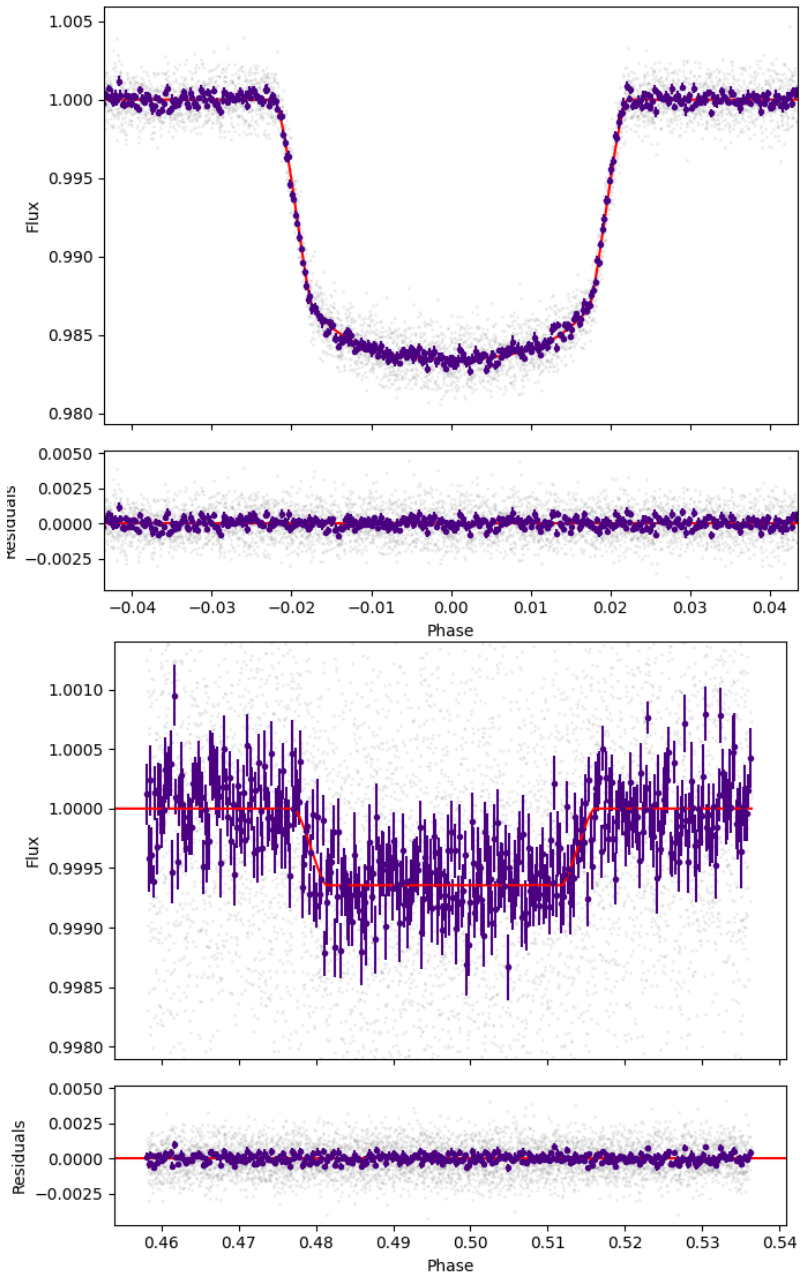

Figure A.33: *TESS* light curves (grey points) for J1640+49 with best fit of `BATMAN` from my analysis in Section 3 (red line) from `EMCEE` analysis. Data binned in 120 s intervals with errors equivalent to the mean absolute deviation are shown for reference in purple. Top panel: primary eclipse. Bottom panel: secondary eclipse.

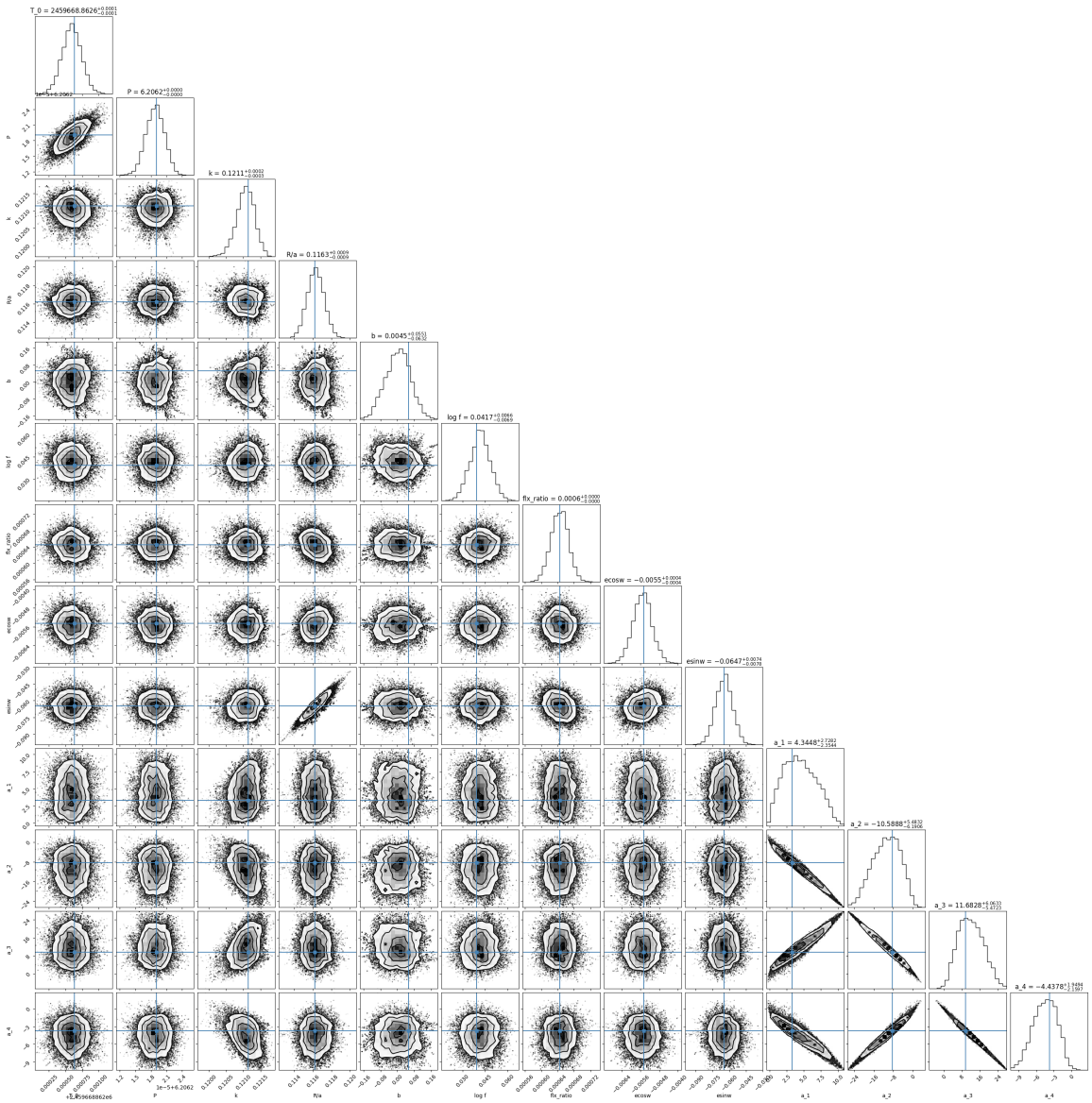

Figure A.34: Corner plots from best fits of `BATMAN` to *TESS* data using `EMCEE` from my analysis in Section 3 for J1640+49.

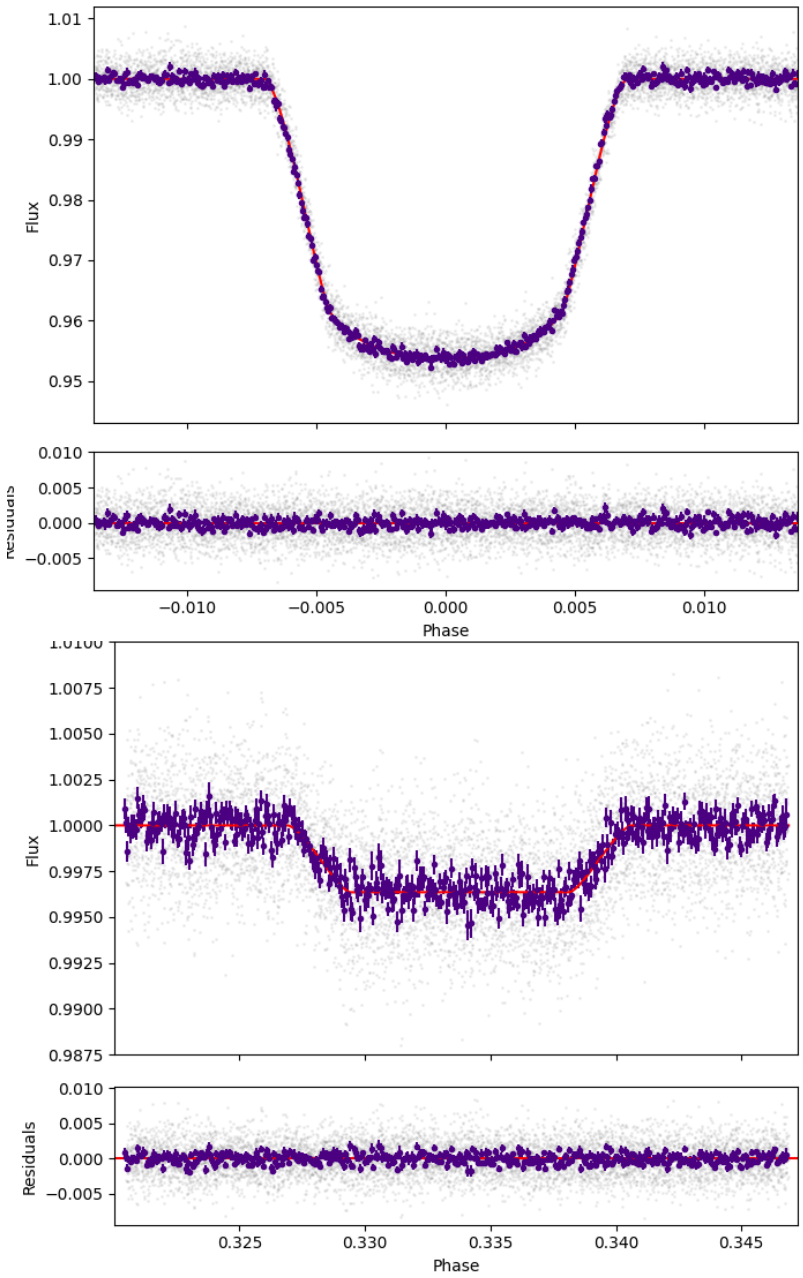

Figure A.35: *TESS* light curves (grey points) for J1705+55 with best fit of `BATMAN` from my analysis in Section 3 (red line) from `EMCEE` analysis. Data binned in 120 s intervals with errors equivalent to the mean absolute deviation are shown for reference in purple. Top panel: primary eclipse. Bottom panel: secondary eclipse.

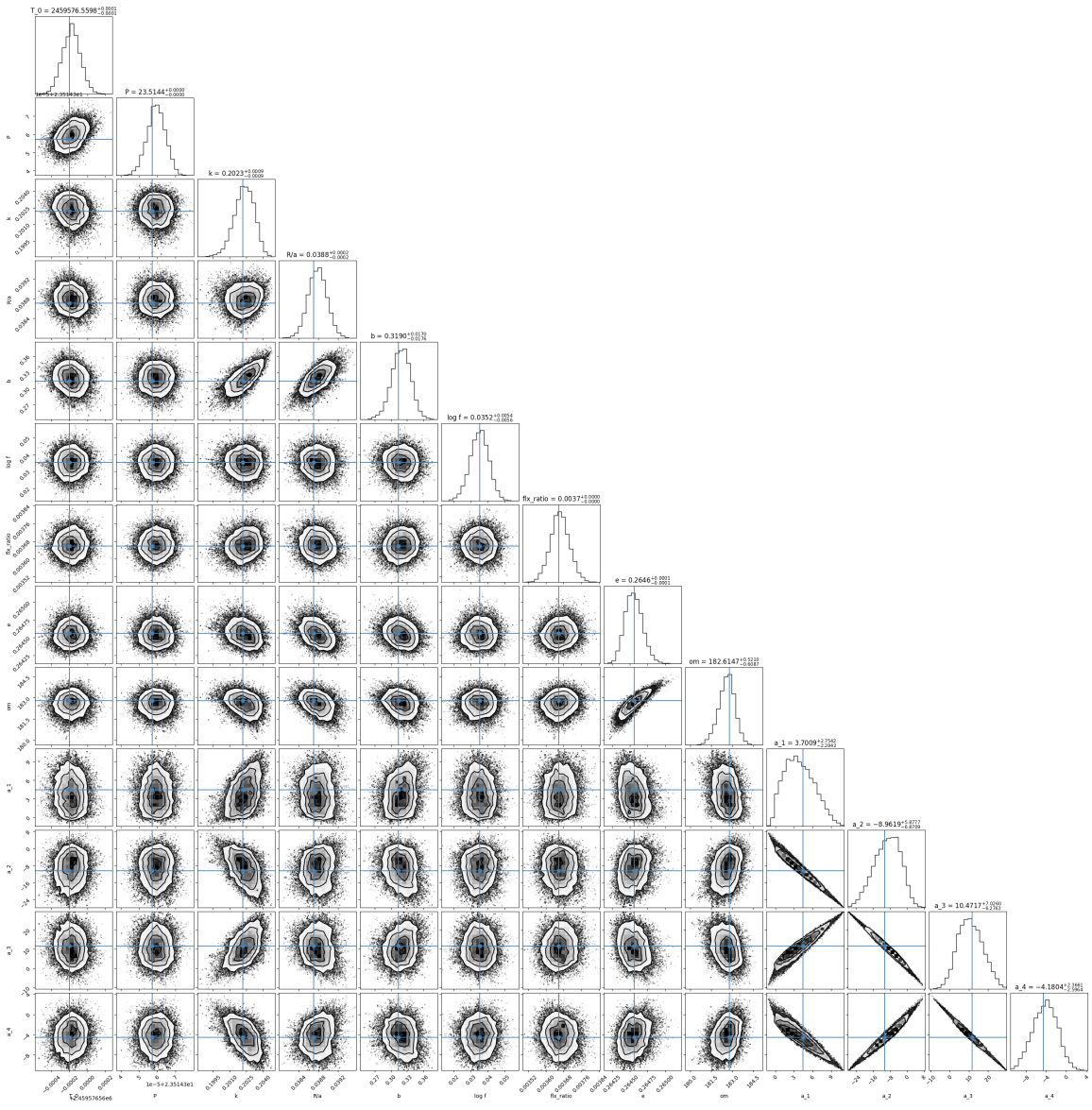

Figure A.36: Corner plots from best fits of `BATMAN` to *TESS* data using `EMCEE` from my analysis in Section 3 for J1705+55.

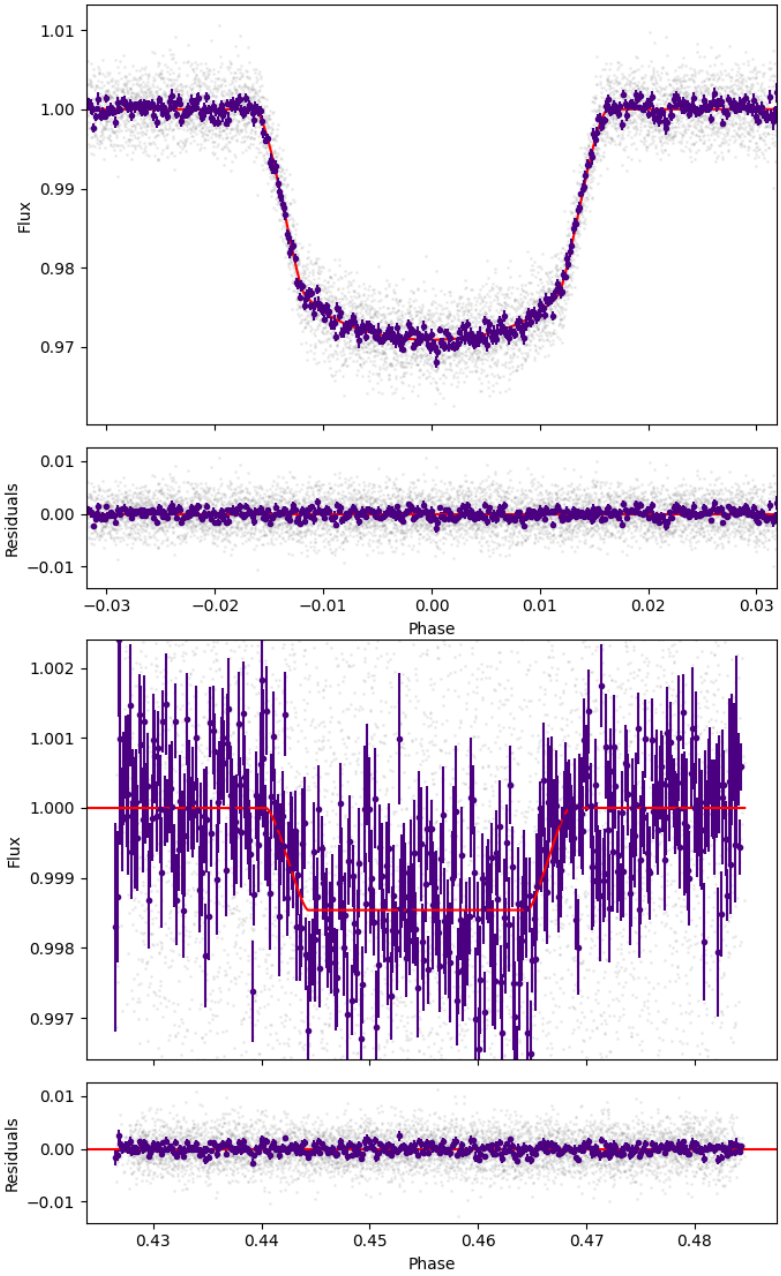

Figure A.37: *TESS* light curves (grey points) for J1850+50 with best fit of `BATMAN` from my analysis in Section 3 (red line) from `EMCEE` analysis. Data binned in 120 s intervals with errors equivalent to the mean absolute deviation are shown for reference in purple. Top panel: primary eclipse. Bottom panel: secondary eclipse.

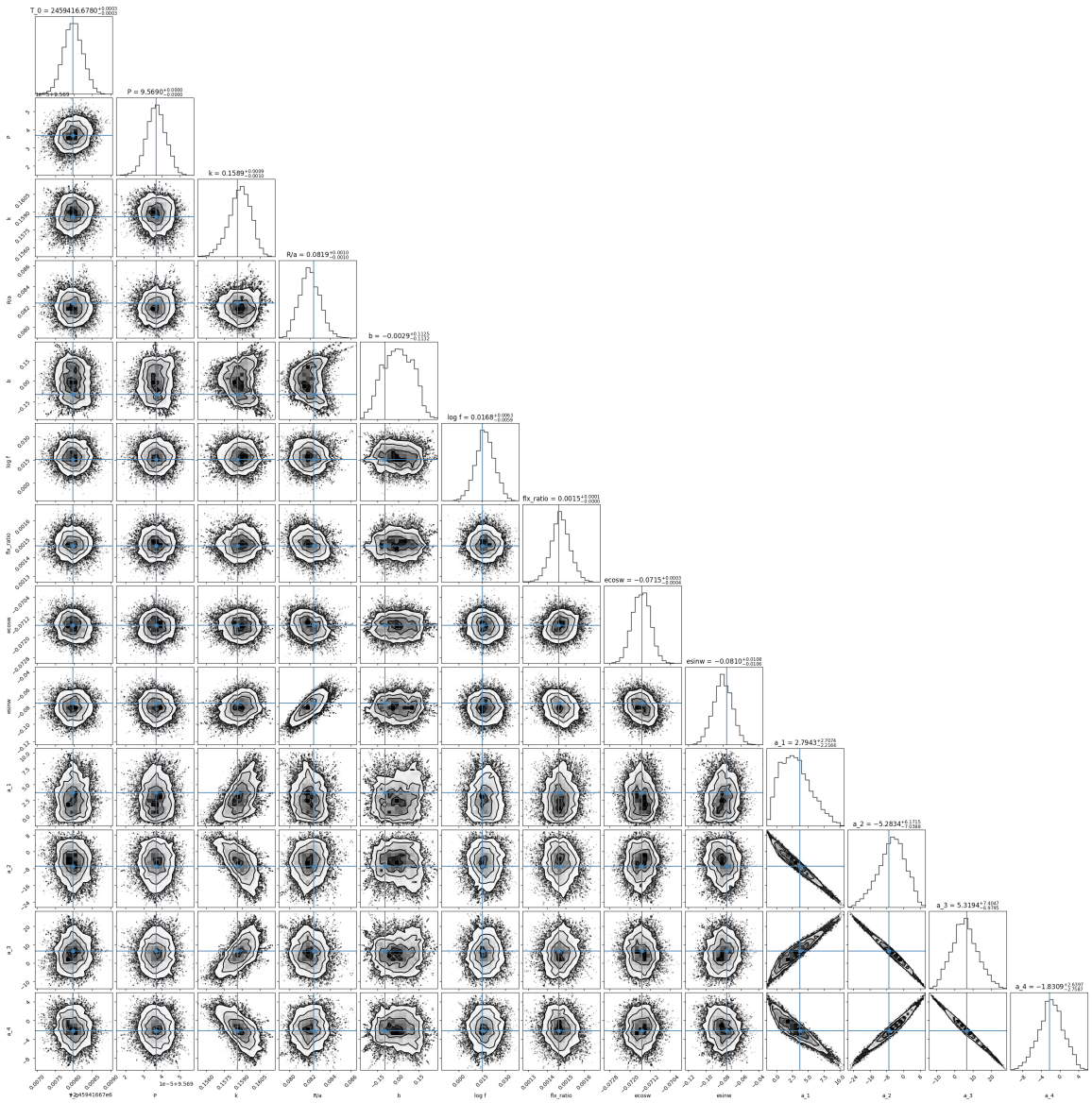

Figure A.38: Corner plots from best fits of `BATMAN` to *TESS* data using `EMCEE` from my analysis in Section 3 for J1850+50.

Bibliography

Adibekyan V., 2019, Geosciences, 9, 105

Allard F., Homeier D., Freytag B., 2011, in Johns-Krull C., Browning M. K., West A. A., eds, Astronomical Society of the Pacific Conference Series Vol. 448, 16th Cambridge Workshop on Cool Stars, Stellar Systems, and the Sun. p. 91 (arXiv:1011.5405), doi:10.48550/arXiv.1011.5405

Allard F., Homeier D., Freytag B., 2012, Philosophical Transactions of the Royal Society of London Series A, 370, 2765

Andrae R., et al., 2022, arXiv e-prints, p. arXiv:2206.06138

Asplund M., Grevesse N., Sauval A. J., Scott P., 2009, ARA&A, 47, 481

Barber R. J., Tennyson J., Harris G. J., Tolchenov R. N., 2006, MNRAS, 368, 1087

Bensby T., Feltzing S., Lundström I., 2003, A&A, 410, 527

Bensby T., Feltzing S., Lundström I., Ilyin I., 2005, A&A, 433, 185

Böhm-Vitense E., 1958, ZA, 46, 108

Böhm-Vitense E., 1960, in Thomas R. N., ed., Vol. 12, Aerodynamic Phenomena in Stellar Atmospheres. pp 338–345

Borkovits T., Rappaport S., Hajdu T., Sztakovics J., 2015, MNRAS, 448, 946

Borucki W., et al., 2008, in Sun Y.-S., Ferraz-Mello S., Zhou J.-L., eds, Vol. 249, Exoplanets: Detection, Formation and Dynamics. pp 17–24, doi:10.1017/S174392130801630X

Buder S., et al., 2021, MNRAS, 506, 150

Carter J. A., Yee J. C., Eastman J., Gaudi B. S., Winn J. N., 2008, ApJ, 689, 499

Castelli F., Kurucz R. L., 2003, in Piskunov N., Weiss W. W., Gray D. F., eds, Vol. 210, Modelling of Stellar Atmospheres. p. A20 (arXiv:astro-ph/0405087), doi:10.48550/arXiv.astro-ph/0405087

Chabrier G., Baraffe I., 1997, A&A, 327, 1039

Choi J., Dotter A., Conroy C., Cantiello M., Paxton B., Johnson B. D., 2016, ApJ, 823, 102

Claret A., 2000, A&A, 363, 1081

Claret A., 2017, A&A, 600, A30

Claret A., 2018, A&A, 618, A20

Collins K. A., et al., 2018, AJ, 156, 234

Cortés-Contreras M., et al., 2020, in XIV.0 Scientific Meeting (virtual) of the Spanish Astronomical Society. p. 131

Díaz R. F., et al., 2013, A&A, 551, L9

Dotter A., 2016, ApJS, 222, 8

Enoch B., Collier Cameron A., Parley N. R., Hebb L., 2010, A&A, 516, A33

Espinoza N., Jordán A., 2016, MNRAS, 457, 3573

Fabrycky D. C., 2010, arXiv e-prints, p. arXiv:1006.3834

Foreman-Mackey D., Hogg D. W., Lang D., Goodman J., 2013, PASP, 125, 306

Fossati L., Koskinen T., France K., Cubillos P. E., Haswell C. A., Lanza A. F., Pillitteri I., 2018, AJ, 155, 113

Freckelton A., et al., 2023, BEBOP V. Homogeneous Stellar Analysis of Potential Circumbinary Planet Hosts, MNRAS (submitted)

Gaia Collaboration 2018, VizieR Online Data Catalog, p. I/345

Gaia Collaboration 2020, VizieR Online Data Catalog, p. I/350

Gaia Collaboration 2022a, VizieR Online Data Catalog, p. I/355

Gaia Collaboration 2022b, VizieR Online Data Catalog, p. I/357

Gaia Collaboration et al., 2021, A&A, 649, A1

Gaudi B. S., et al., 2017, Nature, 546, 514

Gómez Maqueo Chew Y., et al., 2014, A&A, 572, A50

Gonzalez G., 1997, MNRAS, 285, 403

Goodman J., Weare J., 2010, Communications in Applied Mathematics and Computational Science, 5, 65

Hastings W. K., 1970, Biometrika, 57, 97

Hestroffer D., 1997, A&A, 327, 199

Higl J., Weiss A., 2017, A&A, 608, A62

Hoxie D. T., 1970, ApJ, 161, 1083

Husser T. O., Wende-von Berg S., Dreizler S., Homeier D., Reiners A., Barman T., Hauschildt P. H., 2013, A&A, 553, A6

Johnson D. R. H., Soderblom D. R., 1987, AJ, 93, 864

Jönsson H., et al., 2020, AJ, 160, 120

Kostogryz N. M., Witzke V., Shapiro A. I., Solanki S. K., Maxted P. F. L., Kurucz R. L., Gizon L., 2022, A&A, 666, A60

Kostogryz N., et al., 2023, in PLATO Stellar Science Conference 2023. p. 54, doi:10.5281/zenodo.8117867

Kreidberg L., 2015, PASP, 127, 1161

Lanza A. F., 2014, A&A, 572, L6

LeBlanc F., 2010, An Introduction to Stellar Astrophysics

Lightkurve Collaboration et al., 2018, Lightkurve: Kepler and TESS time series analysis in Python, Astrophysics Source Code Library, record ascl:1812.013 (ascl:1812.013)

Limber D. N., 1958, ApJ, 127, 387

Martin D. V., et al., 2019, A&A, 624, A68

Maxted P. F. L., 2018, A&A, 616, A39

Maxted P. F. L., 2023, MNRAS, 519, 3723

Maxted P. F. L., et al., 2022, MNRAS, 514, 77

Maxted P. F. L., Triaud A. H. M. J., Martin D. V., 2023, Universe, 9, 498

Metropolis N., Rosenbluth A. W., Rosenbluth M. N., Teller A. H., Teller E., 1953, JChPh, 21, 1087

Montes D., López-Santiago J., Gálvez M. C., Fernández-Figueroa M. J., De Castro E., Cornide M., 2001, MNRAS, 328, 45

Morello G., Tsiaras A., Howarth I. D., Homeier D., 2017, AJ, 154, 111

Müller H. M., Huber K. F., Czesla S., Wolter U., Schmitt J. H. M. M., 2013, A&A, 560, A112

Niemczura E., Smalley B., Pych W., 2014, Determination of Atmospheric Parameters of B-, A-, F- and G-Type Stars, doi:10.1007/978-3-319-06956-2.

Osborn A., Bayliss D., 2020, MNRAS, 491, 4481

Pecaut M. J., Mamajek E. E., 2013, ApJS, 208, 9

Prša A., et al., 2022, ApJS, 258, 16

Ricker G. R., et al., 2014, in Oschmann Jacobus M. J., Clampin M., Fazio G. G., MacEwen H. A., eds, Society of Photo-Optical Instrumentation Engineers (SPIE) Conference Series Vol. 9143, Space Telescopes and Instrumentation 2014: Optical, Infrared, and Millimeter Wave. p. 914320 (arXiv:1406.0151), doi:10.1117/12.2063489

Santos N. C., Israelian G., Mayor M., 2000, A&A, 363, 228

Santos N. C., Israelian G., Mayor M., 2001, A&A, 373, 1019

Santos N. C., et al., 2013, A&A, 556, A150

Schanche N., et al., 2019, MNRAS, 488, 4905

Schwarzschild K., 1906, Nachrichten von der Königlichen Gesellschaft der Wissenschaften zu Göttingen. Math.-phys. Klasse, 195, 41

Silva Aguirre V., et al., 2017, ApJ, 835, 173

Smalley B., 2014, in , Determination of Atmospheric Parameters of B-, A-, F- and G-Type Stars. pp 131–140, doi:10.1007/978-3-319-06956-2˙12

Soubiran C., et al., 2018, A&A, 616, A7

Sousa S. G., et al., 2021, A&A, 656, A53

Steinmetz M., et al., 2020, AJ, 160, 83

Su T., et al., 2022, ApJS, 261, 26

Sullivan P. W., et al., 2015, ApJ, 809, 77

Swayne M. I., et al., 2023, arXiv e-prints, p. arXiv:2312.11339

Triaud A. H. M. J., et al., 2013, A&A, 549, A18

Triaud A. H. M. J., et al., 2017, A&A, 608, A129

Viani L. S., Basu S., Ong J. M. J., Bonaca A., Chaplin W. J., 2018, ApJ, 858, 28

Wanderley F., et al., 2023, ApJ, 951, 90